DISSERTATION

Modeling of Matrix Damage in Particle Reinforced Ductile Matrix Composites

ausgeführt zum Zwecke der Erlangung des akademischen Grades eines
Doktors der technischen Wissenschaften unter der Leitung von

ao.Univ.Prof. Dipl.-Ing. Dr.techn. Helmut Johann BÖHM, MSc.
E317
Institut für Leichtbau und Struktur-Biomechanik

eingereicht an der Technischen Universität Wien
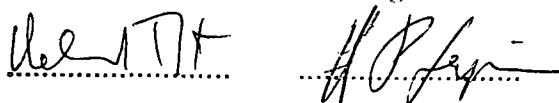Fakultät für Maschinenwesen und Betriebswissenschaften

von

Dipl.-Ing. Thomas DRABEK
Matrikelnummer: 9427633
Helblinggasse 1-3/23
A-1170 Wien

Wien, am 27. Januar 2005

Thomas Drabek

Diese Dissertation haben begutachtet:

Kurzfassung

Die vorliegende Arbeit befaßt sich mit der Simulation duktiler Schädigung in Metall-Matrix-Verbundwerkstoffen (MMCs) mit Hilfe der Finiten Elemente Methode.

Bei den untersuchten Materialien handelt es sich um eine duktile Matrix mit eingebetteten Verstärkungen in Form von Partikeln mit Größen von einigen Mikrometern. Das Ziel dieser Arbeit ist die Untersuchung des Einflusses der Partikelanordnung und -größe auf die Schädigung der Matrix und somit auch auf das Versagen des gesamten Verbundwerkstoffes. Da es sich bei den in MMCs auftretenden Schädigungsmodi (Matrixschädigung, Partikelbruch und Interfaceversagen) um lokale Phänomene handelt, muß eine Strategie gewählt werden, mit der sowohl die Matrix als auch die Verstärkungen im Finiten Elemente Netz modelliert werden können. Aufgrund der vorherrschenden Längenskala sind solche Simulationen auch als mikromechanische Berechnungen bekannt. Mit einem solchen Ansatz ist es möglich, das globale Verhalten des untersuchten Materials in unterschiedlichen Belastungsfällen zu berechnen ("Materialcharakterisierung").

Um die gestellte Aufgabe erfüllen zu können, wurden Materialroutinen in das kommerzielle Finite Elemente Programm ABAQUS/Standard implementiert, welche in der Lage sind, das Verhalten von elasto-plastischen Materialien sowohl im ungeschädigten als auch im geschädigten Zustand zu beschreiben.

Es ist allerdings aus der Literatur bekannt, daß solche Schädigungsmodelle eine Netzabhängigkeit aufweisen, welche dazu führen kann, daß die errechnete Lösung von der gewählten Netzgröße bestimmt wird, was natürlich einen inakzeptablen Zustand darstellt. Ein nichtlokaler Ansatz wurde herangezogen und implementiert, um dieses Problem zu verringern.

Die vorliegende Arbeit beinhaltet eine kurze Einführung in Metall-Matrix-Verbundwerkstoffe und deren Versagensmodi, eine Diskussion der bekanntesten in der Literatur zu findenden duktilen Schädigungsmodelle, eine detaillierte Beschreibung der Implementierung von drei nichtlokalen Schädigungsmodellen in ABAQUS/Standard und eine Diskussion von mit Einheitszellenanalysen erzielten Resultaten.

Abstract

The present work deals with the simulation of ductile damage in metal matrix composites (MMCs) by the finite element method. The materials studied consist of a ductile matrix with embedded particulate reinforcements the size of which is of the order of a few microns. The aim of this work encompasses research on the influence of particle arrangement and size on matrix damage and, hence, the failure of the whole composite.

The observed failure modes of MMCs – matrix damage, particle fracture and interface debonding – act as local phenomena. Accordingly, an obvious modeling strategy consists in resolving the matrix as well as the reinforcements in a finite element mesh. Due to the governing length scale this kind of simulations are also known as micromechanical models. This approach provides the capability of investigating the global behavior of the material under a wide range of thermomechanical loads ("material characterization").

In order to fulfill the above task, a number of material subroutines were implemented into the commercial finite element program ABAQUS/Standard. These subroutines have the capability of describing the behavior of elastoplastic metallic materials in their undamaged as well as in their damaged states.

It is well known from the literature that such damage models in their basic form show an inherent mesh dependence as a consequence of which the results of simulations may be governed by the finite element mesh size. Because such behavior is evidently not acceptable, a nonlocal approach was applied and implemented that allows to mitigate or prevent the above problem.

This work contains a short introduction to metal matrix composites and their failure modes, a description of some important ductile damage models available from the literature, a detailed explanation of the implementation into ABAQUS/Standard for three models, and a discussion of results obtained with finite element analyses.

Acknowledgments

Contents

List of Symbols

Symbols – scalars

A	material parameter in the GTN and Rousselier models
A_f	material parameter in the Oyane model
B	multiplier in the Rousselier model
c	damping factor
c_s^e	elastic wave speed
COMV	common variable in FORTRAN (general)
D	variable to indicate the progress of damage ($D = 0$ indicates a damage free state)
$\bar{D}$	variable to indicate the progress of damage ($\bar{D} = 1$ indicates a damage free state)
$\tilde{D}$	material parameter in the Rousselier model
D_{Ay}	ductile damage indicator proposed by Ayada et al.
D_{Br}	ductile damage indicator proposed by Brozzo et al.
D_{CL}	ductile damage indicator proposed by Cockcroft and Latham
D_{Gu}	ductile damage indicator proposed by Gunawardena et al.
D_{McC}	ductile damage indicator proposed by McClintock
D_{Oy}	ductile damage indicator proposed by Oyane
e	additional degree of freedom
E	Young's modulus
f	void volume fraction
f^*	modified void volume fraction in the GTN model
f_0	initial void volume fraction
f_c	critical void volume fraction
f_f	void volume fraction at final failure (GTN model)
f_F	void volume fraction at final failure (Rousselier model)

g	flow potential
G	shear modulus
h	element size
H	Heaviside function
H_i	state variables
IVOL	integration point volume[1]
k	hardening coefficient
K	bulk modulus
$\hat{K}$	multiplier in the GTN model
L	half of the characteristic length
$\mathcal{L}_i$	is a set of integers that indicates which enrichment functions are activated at node i
LOP	indicates the actual state when UEXTERNALDB is called[1]
m	interaction parameter in cohesive zone models
m_i	material parameters in the ductile damage models (general)
m_C	material parameter in the Cosserat model
M	enrichment function
n	hardening exponent
N	shape function
$\tilde{N}$	load cycles
$\tilde{N}_f$	load cycles at final failure
N_{node}	number of nodes of the finite element model
p_1	the product of the smoothing function, w, and the integration point volume, $\hat{V}$
q	damage variable (general)
q_L	local damage variable
q_{NL}	nonlocal damage variable
q_1	material parameter in the GTN model
q_2	material parameter in the GTN model
q_3	material parameter in the GTN model
q_4	material parameter in the modified Rousselier model
r	radius of the "cap" in the extended Rousselier model
s	path along the process zone
s_p	length of the process zone path
STATEV	state variable (general)[1]

TOLER	termination condition in the Newton algorithm
u	offset of the center of the circle in the extended Rousselier model
$\hat{V}$	integration point volume
w	smoothing function in the nonlocal approach
W	normalizing function in the nonlocal approach
z	distance between two integration points

Γ_0	cohesive energy
δ_{ij}	Kronecker delta
$\Delta\Lambda$	plastic multiplier
ε_p	first scalar in the RMA of pressure-dependent plasticity models
ε_q	second scalar in the RMA of pressure-dependent plasticity models
ε_{eq}^{pl}	accumulated equivalent plastic strain
$\varepsilon_{eq,f}^{pl}$	accumulated equivalent plastic strain at failure
ε_0	material parameter in the Gunawardena model
ε_D	equivalent plastic strain at damage initiation in the Lemaître model
ε_R	equivalent plastic strain at final failure in the Lemaître model
ζ	relaxation time
η	stress triaxiality
ν	Poisson's ratio
ξ	volume fraction
ρ	relative density
σ_1	material parameter in the Rousselier model
$\sigma_I, \sigma_{II}, \sigma_{III}$	principal normal stresses ($\sigma_I \geq \sigma_{II} \geq \sigma_{III}$)
σ_a	stress amplitude
σ_{eq}	von Mises equivalent stress
σ_{eq}^*	von Mises equivalent stress at $\sigma_m = 0$
σ_f	flow stress
σ_f'	derivative of the flow stress, σ_f, with respect to the equivalent plastic strain, ε_{eq}^{pl}
$\sigma_{f,0}$	initial flow stress
σ_m	mean stress
σ_m^*	mean stress at $\sigma_{eq} = 0$
$\Phi, \tilde{\Phi}, \hat{\Phi}$	yield function
Ω_+, Ω_-	volume Ω split by a discontinuity into regions $+$ and $-$

Symbols – vectors, matrices, tensors

$\mathbf{C}$	tangential material tensor (Jacobian)
$\mathbf{C}^e$	elastic material tensor
COORD	vector of coordinates of the integration point[1]
DDSDDE	consistent tangent tensor[1]
$\mathbf{e}$	vector of additional degrees of freedom
$\mathbf{F}$	deformation gradient
$\mathbf{F}^{el}$	elastic contribution of the deformation gradient
$\mathbf{F}^{pl}$	plastic contribution of the deformation gradient
$\mathbf{I}$	second order identity tensor
$\mathbf{J}$	fourth order identity tensor
$\mathbf{M}^*$	artificial mass matrix
$\mathbf{n}$	multiple of the deviatoric part of the stress tensor
$\bar{\mathbf{n}}$	vector of possible wave propagation directions
$\mathbf{Q}$	acoustic tensor
$\mathbf{RF}$	vector of reaction forces at the nodes[1]
$\mathbf{S}$	deviatoric part of the stress tensor
$\mathbf{T}$	averaged traction acting in a process zone
$\mathbf{u}$	interpolated vector of local displacements
$\mathbf{U}$	vector of displacements at nodes
$\mathbf{V}$	vector of nodal velocities
$\mathbf{VF}$	vector of viscous forces at the nodes[1]
$\mathbf{x}$	vector of actual position
$\mathbf{X}$	vector of initial position
$\mathbf{y}$	vector of actual position
$\boldsymbol{\alpha}$	vector of rotational degrees of freedom
$\boldsymbol{\delta}$	vector of the averaged separation in a process zone
$\boldsymbol{\varepsilon}$	strain tensor
$\boldsymbol{\varepsilon}^e$	elastic strain tensor
$\boldsymbol{\varepsilon}^e_D$	deviatoric part of the elastic strain tensor
$\boldsymbol{\varepsilon}^e_V$	volumetric part of the elastic strain tensor
$\boldsymbol{\varepsilon}^{pl}$	plastic strain tensor

ε_D^{pl} deviatoric part of the plastic strain tensor

ε_V^{pl} volumetric part of the plastic strain tensor

σ stress tensor

$\tilde{\sigma}$ effective stress tensor in the Lemaître damage model

σ_m hydrostatic stress tensor

Superscripts and subscripts

x^{cons} consistent derived value

x_{crit} critical value

x_{inc} values in time increment inc

x^{int} intersection point

x_{max} maximum value

x_N in normal direction

x_{ref} reference value

x_t, x^t variable at time t

x^{tr} values in the elastic trial step (RMA)

x_T in tangential direction

$\dot{x}$ time derivative

Abbreviations

DDIT   ductile damage indicator triggered model

EWED   elements with embedded discontinuities

FE   finite element

FEM   finite element method

GTN   Gurson-Tvergaard-Needleman model

HSS   high speed steel

ip(s)   integration point(s)

MMC   metal matrix composite

pbc   periodicity boundary conditions

pvf	particle volume fraction
PM	powder metallurgical
PMMA	polymethyl-methacrylate
RAM	random access memory
RMA	return mapping algorithm
RVE	reference volume element
sbc	symmetry boundary conditions
UEL	user defined element[1]
UEXTERNALDB	user defined external data base subroutine[1]
UMAT	user defined material subroutine in ABAQUS/Standard[1]
USDFLD	user defined field subroutine[1]
VUMAT	user defined material subroutine in ABAQUS/Explicit[1]
X-FEM	extended finite element method

---

[1]The notation has been adopted from ABAQUS.

Chapter 1

Introduction

1.1 General Remarks on Metal Matrix Composites

A composite can be defined as a material that consists of at least two different constituents that are bonded together along their interfaces. In this context, a material will be called metal matrix composite (MMC), if the matrix of the composite that encloses the reinforcements consists of a metal. MMCs can contain continuous fibers, short fibers or particles acting as reinforcements which may consist of metallic or non-metallic materials (in most of the cases ceramics and metal-carbides). Three sketches of the different kinds of reinforcements are shown in fig. 1.1.

The excellent ductility and formability of the metal matrix and the high stiffness and load carrying capacity of the reinforcement give rise to a global material behavior (e.g. stiffness and strength enhancement, increased creep and wear resistance, density reduction) that is of interest in many industrial applications. The combination of the high thermal conductivity of the metal matrix and the very low thermal expansion of the reinforcement have also drawn the attention of researchers towards investigating the mechanisms acting in such composites.

The material behavior of MMCs depends strongly on the behavior of the involved constituents and on the distribution, orientation and volume fraction of the reinforcements. If one is able to manipulate these properties in manufacturing processes, one can "design" high-tech materials that show targeted values of material parameters, such as Young's modulus, yield stress or coefficient of thermal expansion.

Due to the high cost of many MMCs, their applications have been limited to industrial

fields where the benefit of the improved material behavior yields an appropriate cost reduction in the use of the material. The aerospace industry is an important consumer in that case, but further applications have been developed in the automotive, tool, electronic packaging and sports industries as well.

Three processing methods have been primarily used to develop MMCs: high-pressure diffusion bonding, casting, and powder-metallurgy techniques. More specifically, diffusion-bonding have been predominately used for monofilament fiber reinforced MMCs. Particle reinforced MMCs are mainly produced by powder metallurgy, whilst preforms in the squeeze infiltration process are employed in the production of all three kinds of reinforcements.

Two typical metal matrix composites that differ considerably in their mechanical properties will be explained in the following sections.
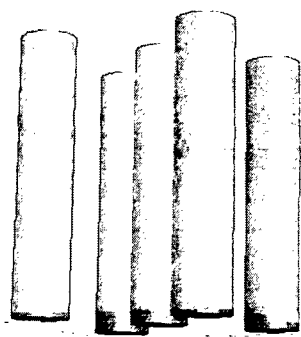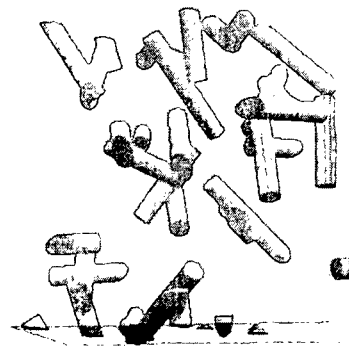
continuous fibers   short fibers
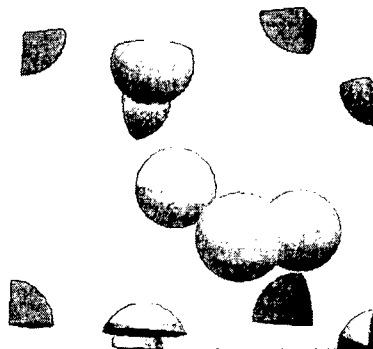
particles

Figure 1.1: Three different kinds of reinforcements

1.1.1 Aluminum Reinforced by SiC Particles

Aluminum and aluminum alloys have become very important engineering materials in the last century especially due to their low density and their good specific material properties. They have experienced considerable use as matrix materials in composites reinforced by silicon carbide (SiC) or aluminum oxide (Al_2O_3) particles that increase the stiffness, wear resistance, strength, and fatigue resistance. Furthermore, the coefficient of thermal expansion of aluminum is reduced while the material retains the high thermal conductivity and low density.

Aluminum Silicon Carbide (Al/SiC_p) metal matrix composite materials offer a variety of outstanding properties for use in high performance electronic packaging, such as high thermal conductivity, low coefficient of thermal expansion and low density. The resulting advantages include higher possible power density, a longer chip life time, higher reliability, and substantial weight savings compared to alternative packaging concepts.

Cast aluminum composite brake drums and rotors, driveshafts and tire studs can be found in automotive applications. In the sports industries, aluminum composites are used for bike and golf components for instance.

A typical microstructure of the above composite material is shown in fig. 1.2.

Figure 1.2: Microstructure of a typical aluminum silicon carbide ($Al/SiC/20_p$) metal matrix composite material

1.1.2 High Speed Steel (HSS) Produced by Powder Metallurgy Methods

Tool steels are special steels used in the manufacture of tools for machining and processing other materials and can be classified into cold-work tool steels, hot-work tool steels and plastic mould steels.

Even though they are not metal matrix composites in the usual sense, tool steels are similar to MMCs in many aspects of their thermomechanical behavior and they can be studied with similar models.

They consist of a steel matrix reinforced by carbidic particles and, like particle reinforced MMCs, they show a matrix–inclusion microtopology.

Tool steels are characterized by a high wear resistance, red hardness, corrosion resistance and compressive strength, all of which are necessary to guarantee a long tool life and good tool precision and, as a consequence, an increased productivity (reduced unit cost).

The most important alloying elements in tool steels are vanadium, chromium, nickel, tungsten, cobalt and molybdenum. The reinforcement of "classical" tool steels consists of hard carbidic particles (M_xC_y), also called the primary carbides, that develop during solidification, the final shapes and sizes of the carbides being obtained by thermomechanical processing. For this reason these materials are often called in-situ composites. In conventionally produced tool steels the distribution of the particles is highly inhomogeneous and their size varies within a wide range. This implies anisotropy effects, and impairs the material properties. As a consequence, the more expensive powder metallurgical (PM) routes have been developed in which the arrangement and geometry of the carbides can be better controlled which allows improved materials to be manufactured, compare fig. 1.3.
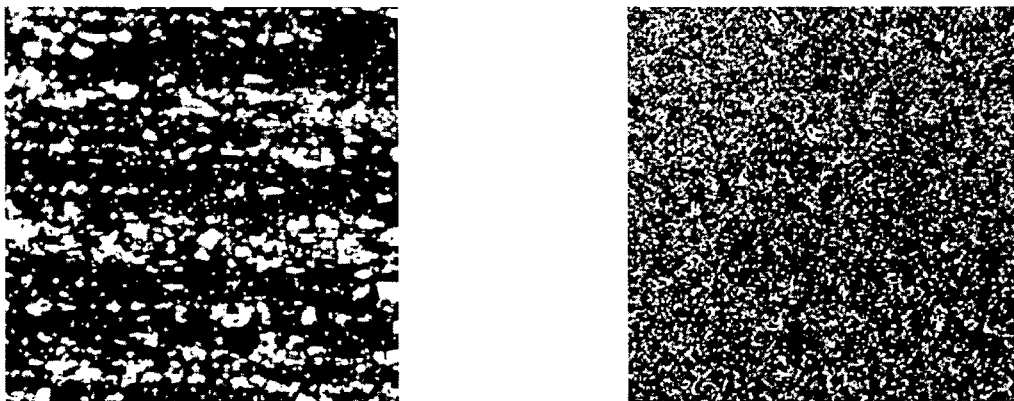
Figure 1.3: Microstructure of conventionally cast and hot deformed tool steel (left) and powder-metallurgy tool steel (right), Böhler [1]

1.2 Failure of Metal Matrix Composites

Damage and failure of ductile matrix composites are due to three local mechanisms, viz. debonding of the matrix–reinforcement interface, brittle fracture of the reinforcing fibers or particles, and ductile failure of the matrix. Local damage due to any of the above mechanisms is triggered by high local values of the stresses and strains in matrix and/or reinforcements, which are a consequence of the marked inhomogeneity of the composite. Examples of the three failure modes are depicted in fig. 1.4.

interfacial debonding   matrix damage
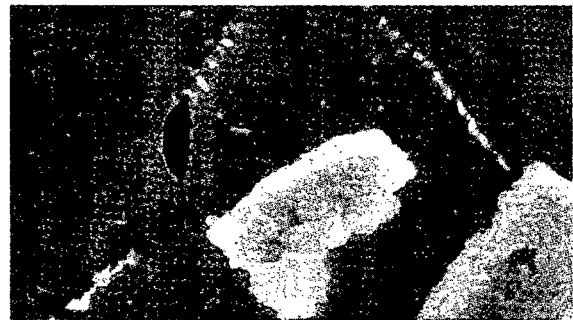
particle cracking

Figure 1.4: The three local failure modes in metal matrix composites, Pandorf [2]

1.3 Simulation of the Thermomechanical Behavior of Composites at Different Length Scales

The simulation of the deformation behavior of mechanical components consisting of composite materials leads to reliable results only if appropriate material models and parameters are used. This requirement leads to the necessity of understanding the architecture of composites and the behavior of their constituents at different length scales.

Figure 1.5 depicts a schematic overview of the different length scales in a structural element beginning at the macroscale and going down to the atomistic scale. The macroscale is the length scale of the structure, whereas the mesocale describes intermediate length scales, e.g. the lamina level in layered composites and reinforcement rich clusters in MMCs. The length scale where the different constituents of the composite (matrix and reinforcements) can be distinguished is called microscale 1 in this context. Microscale 2 deals with the inner structure of a given phase of the composite, where grains, voids, dispersoids or precipitates may be identifiable. The behavior of the different molecules or atoms contained in the material is described in the atomistic scale, which represents the lowest length scale in the figure. The idea of this multiscale approach is to take into account the material properties and the phase arrangement at the lower length scales to obtain the behavior of the higher length scale. This can be done through all the length scales to get the response of the structure due to thermal and/or mechanical loads at the macroscale. If this procedure, known as homogenization, has been performed, the way into the other direction can be tackled. It consists of applying the evaluated stresses at the upper length scale and finding the resultant stresses of the next lower length scale, a procedure known as localization, see e.g. Mura [3], Torquato [4] and Böhm [5].

macroscale

atomistic scale

mesoscale

microscale 2

microscale 1
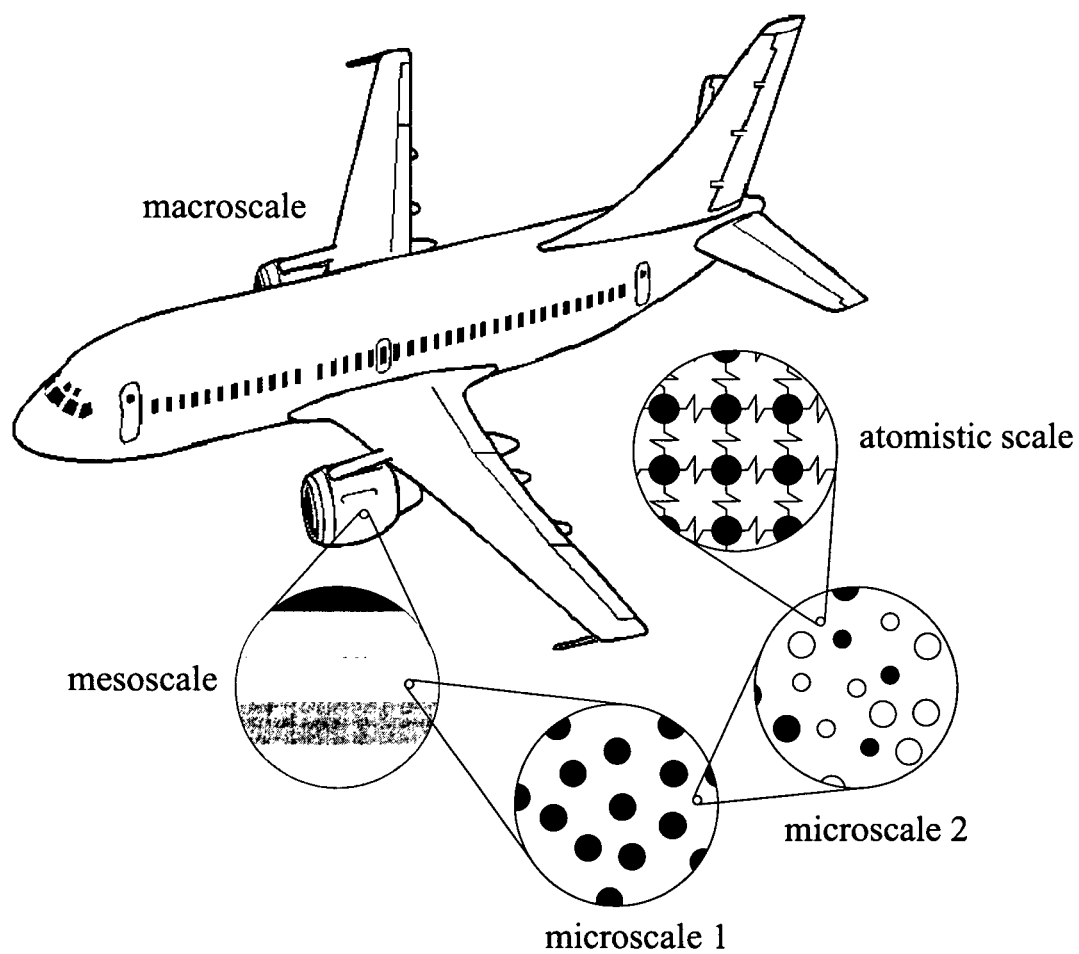
Figure 1.5: Different length scales in a fictitious MMC

Chapter 2

Modeling of Ductile Damage - Literature Research

This chapter gives an overview of the most important ductile damage models used in the literature and presents a discussion about the applicability of the models in order to fulfill the requirements pertinent to this work, that are listed below. The model

- must be able to handle the initiation of ductile cracks,

- must be able to handle complex crack paths (in the matrix of ductile matrix composites),

- must give results that are independent of the employed FE mesh,

- must accommodate a wide range of stress triaxialities, and

- must allow the implementation into the finite element code ABAQUS [6].

The above conditions must be met for micromechanical analyses of ductile matrix composites, where irregular meshes are typically required to discretize multi–particle or multi–fiber arrangements, and high stress and strain gradients as well as high stress triaxialities are the rule rather than the exception. Furthermore, the periodic displacement, stress and strain fields that are characteristic of unit cell analyses must be accommodated.

2.1 Mechanism of Ductile Failure

Ductile damage and failure of metals generally occur by the nucleation, growth and coalescence of voids.

Figure 2.1 shows a schematic sketch of a typical micro-structure in metals containing voids and/or inclusions (dispersoids or precipitates) at a size of the order of nanometers. The size of the inclusions is much smaller than of the reinforcements discussed in the previous section. Due to the current stress state in such a material void growth and the development of new voids by debonding of the metallic "matrix" from the inclusions can be observed. After the voids have grown by a certain extent they coalesce to form microcracks that can grow to become macrocracks that lead to the failure of the specimen or structure.

A number of ductile damage models can be found in the literature which are suitable for describing ductile failure processes via appropriate constitutive equations that consider void growth. The advantage of such models can be explained in the fact, that individual voids do not have to be resolved, i.e. they are homogenized models in the sense of section 1.3. Appropriately formulated smoothed-out descriptions of this type can be used as material models at the integration point level in finite element programs. At present, two major groups of models for describing ductile failure within a finite element framework can be found in the literature. On the one hand, there are volume-oriented descriptions in which damage within planar or three-dimensional continuum elements leads to the loss of their stress carrying capacity and/or to their removal from the finite element model ("element death models"). On the other hand, the progress of ductile cracks can be modeled by decohesion between the continuum elements or along internal discontinuities provided by special elements, i.e. by surface-oriented algorithms.
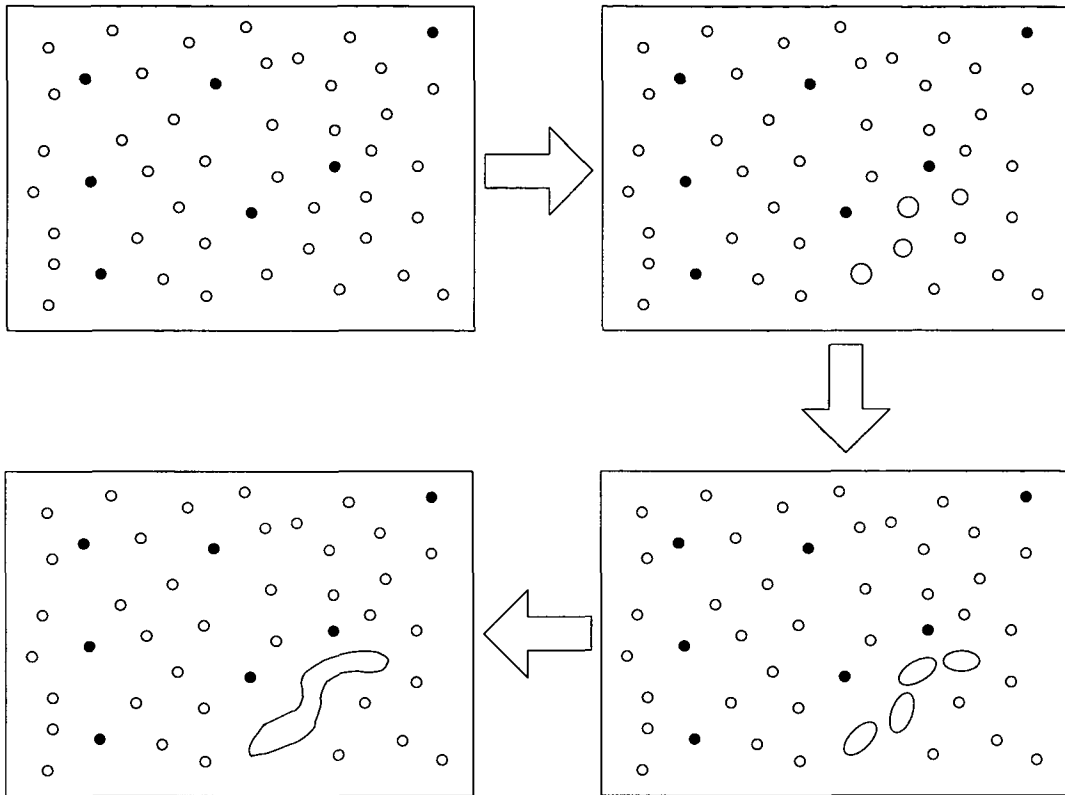
Figure 2.1: Schematic depiction of the microstructure in a ductile material and the failure mechanisms acting within (black: inclusions, empty circles: voids)

2.2 Surface Based Models

The main idea of surface based models is to describe the interaction between two lines in 2D or two surfaces in 3D that represent the so called "process zone" of a crack, shown in fig. 2.2, and the stress distribution at the crack tip. The constitutive description of this behavior takes the form of appropriate traction, T, vs. separation, δ, laws, the principal material parameters (in this case given for the normal direction N) typically being a cohesive strength, $T_{N,max}$, and a cohesive energy, $\Gamma_{N,0}$,

$$\Gamma_{N,0} = \int_0^{\delta_{N,max}} T_N d\delta_N, \tag{2.1}$$

where $\delta_{N,max}$ describes the displacement in normal direction at complete failure, where the tractions vanish. A damage value

$$D = \frac{\delta_N}{\delta_{N,max}} \tag{2.2}$$

can be introduced to indicate the progress of damage in such models, where $D = 1$ stands for complete failure.

Figure 2.3 depicts some typical traction–separation laws used in the literature, which were proposed by Needleman [7], [8] and Scheider [9]. Figure 2.4 shows the laws for concrete, polymethyl-methacrylate (PMMA) and steel proposed by Elices et al. [10]. With the increase of the separation distance the traction between the two cohesive surfaces increases rapidly at first, reaches a maximum value, and then decreases more gradually to zero in fig. 2.3, whereas the curves in fig. 2.4 start at a nonzero traction when the separation δ_N is zero. The traction at zero separation plays an important role when the crack path is not known in advance as will been seen in the following section.

The subsequent decrease of the traction–separation curve (also called the softening regime) corresponds to the stiffness reduction of the material, in the case of metals, due to the growth of voids and a reduction of the load carrying capacity of the process zone.

To consider combinations of normal and shear loading of the process zone appropriate assumptions must be made on the damage value, such as

$$D = \sqrt[m]{\left(\frac{\delta_N}{\delta_{N,max}}\right)^m + \left(\frac{\delta_T}{\delta_{T,max}}\right)^m}, \tag{2.3}$$

where N stands for normal and T for tangential directions, respectively. The parameter m describes the interaction between the normal and shear separation as shown in fig. 2.5. Applications of this kind are presented by Scheider and Brocks [11].

After complete failure between the two cohesive surfaces a friction model must be applied if compressive loads are to be considered.

Surface based models can be subdivided into two groups on the basis of the type of implementation in the finite element code described in the following sections.
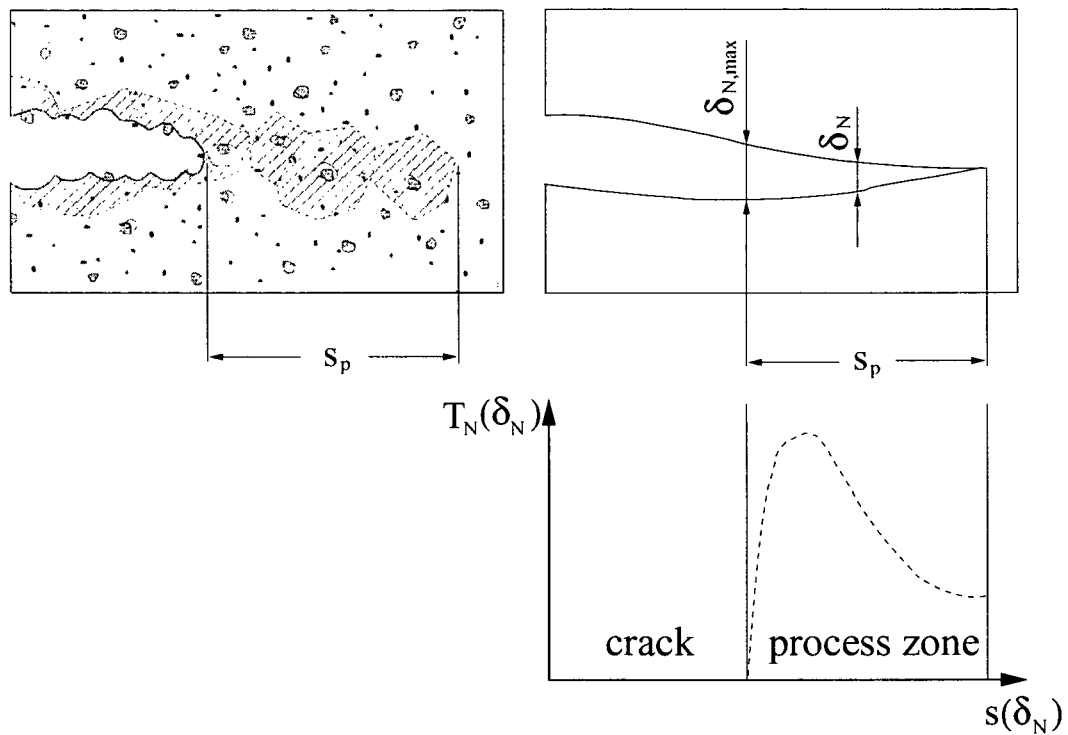
Figure 2.2: Crack and process zone in a real material (left) and modeled with the surface based approach (right); in the diagram on the right, the distribution of the normal component of the traction, T_N, along the process zone path, s, is sketched
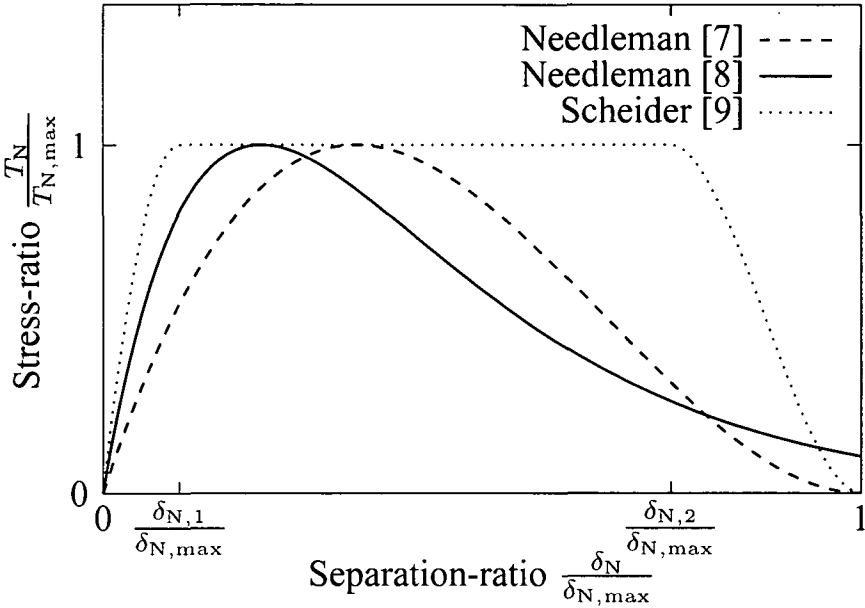
Figure 2.3: Some traction–separation laws for ductile materials proposed in the literature ($\delta_{N,1}$ and $\delta_{N,2}$ are material parameters)
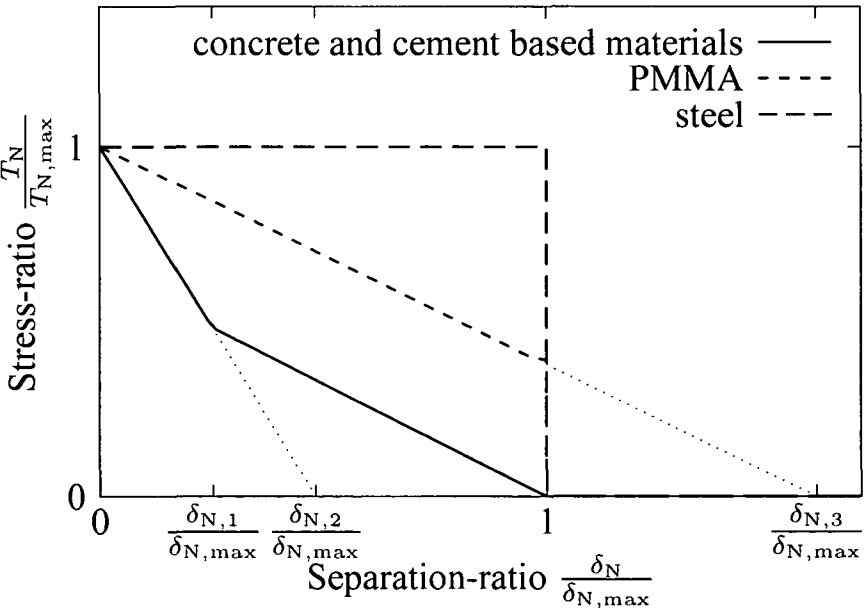
Figure 2.4: Some traction–separation laws proposed for concrete, PMMA and steel by Elices [10] ($\delta_{N,1}$, $\delta_{N,2}$ and $\delta_{N,3}$ are material parameters)
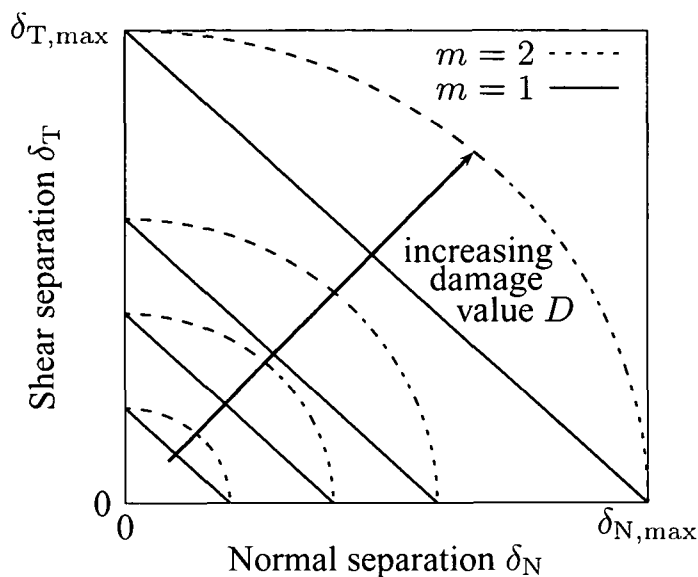
Figure 2.5: Possible combinations between normal and shear separation at different levels of the effective damage value, D, with $m = 1$ and $m = 2$, compare eqn. (2.3)

2.2.1 Cohesive Zone Models

The first group of surface based models is known as cohesive zone or cohesive surface models. They use interface elements that essentially consist of two opposite surfaces that must be separated for a crack to grow, its initial thickness, δ_0, being zero in the load-free and damage-free state.

Cohesive zone models were originally proposed for brittle material behavior by Barenblatt [12] and they were later adapted for handling elastoplastic and elastic-viscoplastic materials, see e.g. Siegmund and Brocks [13] and Siegmund and Needleman [14]. Recent studies by Siegmund and Brocks [13] and Chen et al. [15] have shown that in ductile materials the cohesive strength and energy in general depend on the stress triaxiality.

Cohesive zone models have been widely used in micromechanical studies of composite materials for describing the fracture of reinforcements and the interfacial decohesion between matrix and reinforcements, see e.g. Finot et al. [16] and Tvergaard [17]. In these situations the crack paths are either known a priori or suitable assumptions can be made for them. When there is no prior knowledge of the crack path, however, cohesive zone elements must be provided for all interfaces between the continuum elements that make up a

ductile constituent. On the one hand, this tends to noticeably reduce the overall stiffness as all cohesive surfaces open up slightly under load due to the finite initial slopes of typical traction–separation laws of the type depicted in fig. 2.3, a situation that is sketched in fig. 2.6. This difficulty can in principle be remedied by allowing crack opening only beyond a certain traction threshold as discussed by Elices et al. [10]. On the other hand, with such a model crack paths are by definition constrained to follow element surfaces, which can introduce a considerable mesh dependence of the generated crack surface, compare fig. 2.7, a difficulty that can play a considerable role in continuum micromechanics, where complex mesh geometries are typically required to resolve the constituents. A very interesting approach to overcome this problem was reported by Bouchard et al. [18], where a remeshing algorithm was applied to generate an "appropriate" mesh near the crack that allows the crack to propagate along the finite element boundaries in the previously calculated direction. At present, however, this model is applicable to purely elastic materials only.

The above considerations essentially rule out cohesive zone models for the present purpose.
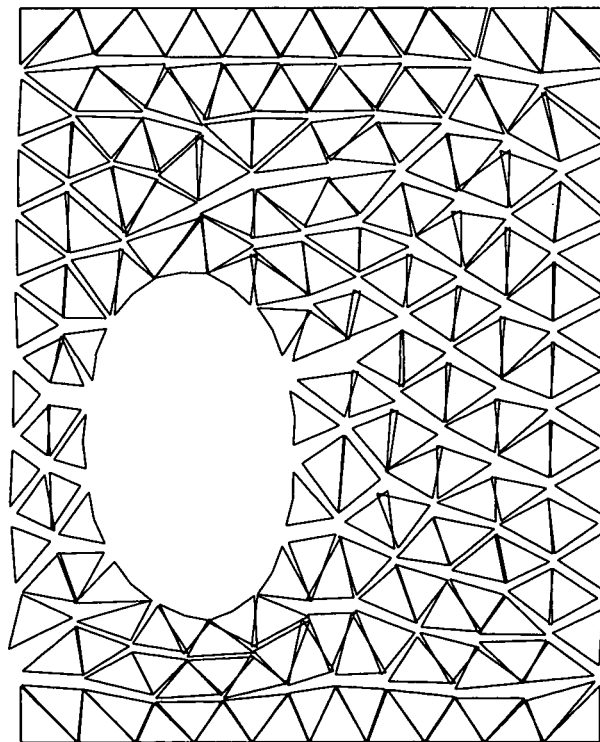
Figure 2.6: Sketch of cohesive zone elements located along all boundaries of elastoplastic continuum elements
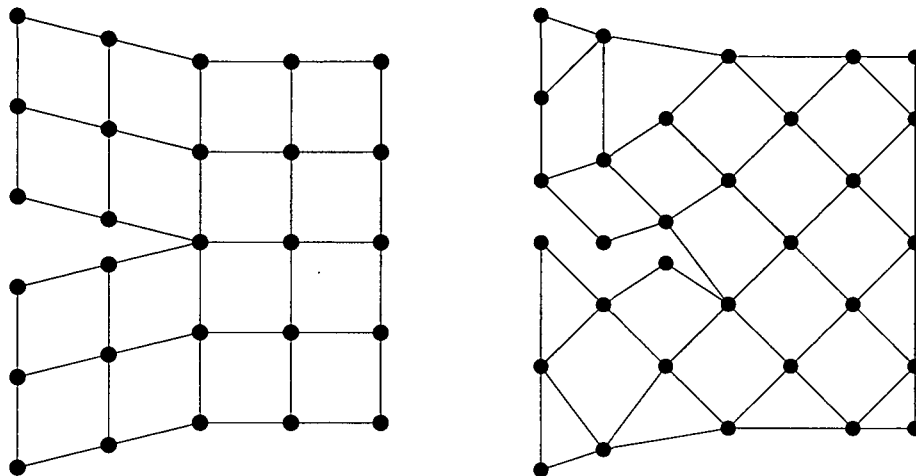
Figure 2.7: Sketches of crack paths that depend on details of two meshes

2.2.2 Embedded Discontinuity Approaches

The limitation caused by the restriction of crack paths to the interfaces between elements can be resolved by embedded discontinuity methods. The main idea of such approaches is to allow the crack to propagate through the finite elements in arbitrary direction and at an arbitrary position in the element. This goal can be reached by element enrichment (elements with embedded discontinuities, EWED, see Armero and Garikipati [19] and Dvorkin et al. [20]) or nodal enrichment (extended finite elements based on the partition of unity, X-FEM, see Belytschko et al. [21], Wells and Sluys [22] and Dolbow et al. [23]), both described in the following.

In the EWED as well as the X-FEM approach, the standard displacement approximation

$$u(x) = \sum_{i=1}^{N_{node}} N_i(x) U_i \tag{2.4}$$

used in the finite element method is enriched by additional degrees of freedom, e_{ij}, and takes the form

$$u(x) = \sum_{i=1}^{N_{node}} N_i(x) \left(U_i + \sum_{j \in \mathcal{L}_i} M_j(x) e_{ij} \right). \tag{2.5}$$

Here N_{node} is the number of nodes of the finite element model, $u(x)$ is the interpolated vector of local displacement, U_i describes the displacement vector at node i and $\mathcal{L}_i \subset$

$\{1, 2, \ldots, m\}$ is a set of integers that indicates which enrichment functions are activated at node i. The global enrichment function in the EWED formulation is defined as

$$M(\mathbf{x}) = H(\mathbf{x}) - \sum_{i \in \Omega_+} N_i(\mathbf{x}), \qquad (2.6)$$

where $H(\mathbf{x})$ stands for the Heaviside function characterizing the discontinuity (unity in Ω_+ and zero in Ω_-). The difference between the EWED and X-FEM approaches is shown in fig. 2.8 for the example of a one-dimensional problem. In this case, there is only one additional degree of freedom, e, in the EWED method, whereas two (e_{21} and e_{31}) will be generated in the X-FEM approach with the global enrichment function

$$M(\mathbf{x}) = H(\mathbf{x}) \qquad (2.7)$$

applied only to the shape functions, N, associated with those nodes that are separated by the discontinuity (nodes 2 and 3 in the example). Beside a local failure criterion (e.g. a traction–separation law) as required in the cohesive zone elements, an additional criterion for determining the direction of the crack must be provided in both methods (e.g. making the propagation of the crack orthogonal to the maximum tensile stress).

An additional problem that must be solved with such algorithms is to make cracks propagate in a compatible way across neighboring elements, see fig. 2.9 and compare the discussions in Jirásek and Zimmermann [24], where it is pointed out that the generated cracks will, in general, not coincide at element boundaries, see fig. 2.9(a) and additional algorithms must be applied to provide a correct crack propagation from one finite element to the other, as depicted in fig. 2.9(b). As mentioned by Wells and Sluys [25] the direction of the crack must be determined at the boundary of the finite element where the stresses are not known accurately and a nonlocal (averaged) stress tensor must be calculated to overcome this problem.

From the author's point of view, the above problems can be tackled with self-written FE-codes only and an implementation into a user element in ABAQUS/Standard will be very difficult, especially the provision of a correct crack transition through finite element boundaries. Accordingly, this class of models was not chosen for the present work, even though they are one of the most promising approaches for modeling crack propagation with the finite element method.
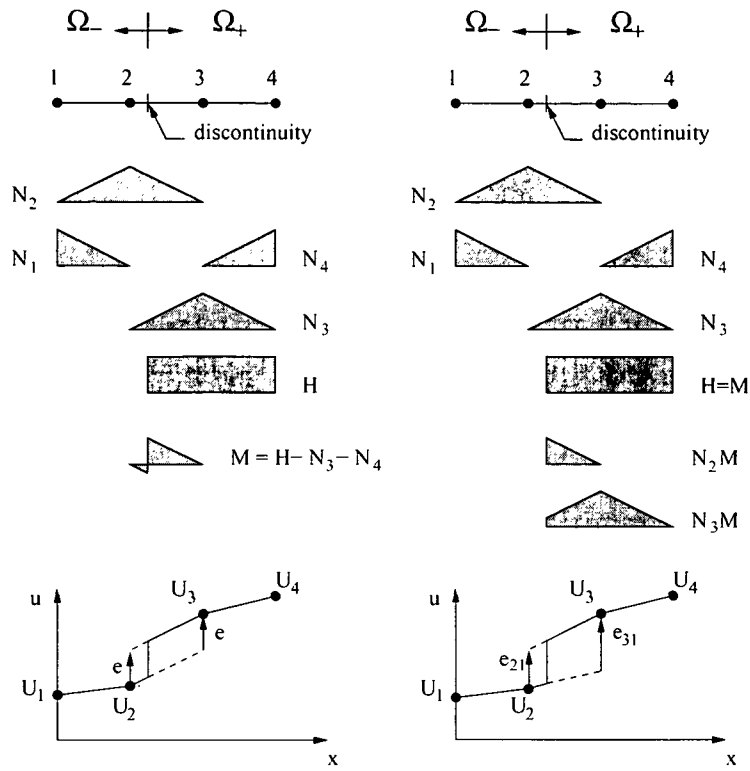
Figure 2.8: Standard shape functions and enrichment functions for the EWED (left) and the X-FEM (right) approaches
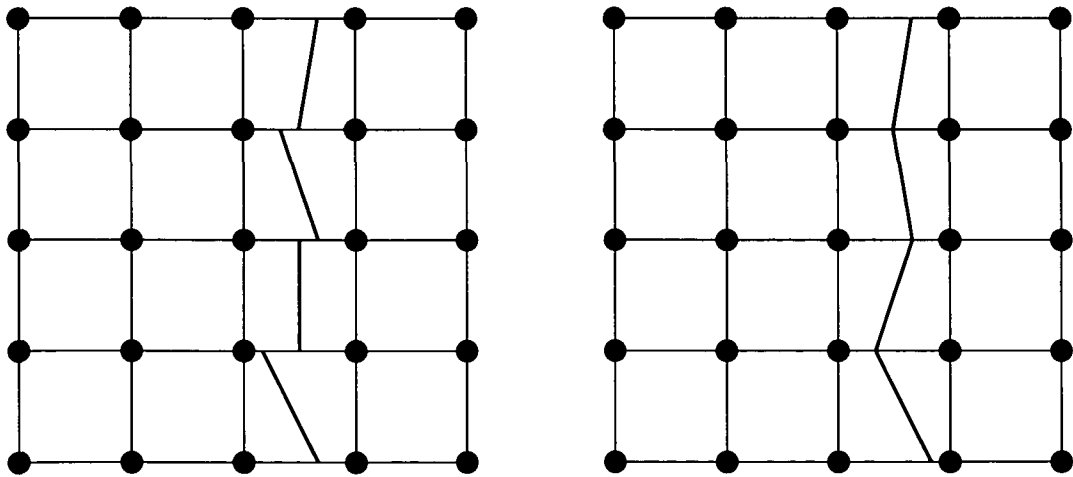
Figure 2.9: Incorrect (left) and correct (right) crack propagation crossing different finite element boundaries

2.3 Continuum Based Models

In this group of models ductile damage and failure are treated on the basis of a process zone, i.e. finite–sized volumes in which the nucleation, growth and coalescence of voids can be described in a smeared-out manner. Following such a continuum damage mechanical concept in micromechanical analyses of composites implies that the characteristic length of the voids is much smaller than that of the reinforcements, so that the effects of damage can be homogenized in the matrix.

In such a framework cracks that are of comparable (or greater) size to the reinforcements take the form of "failed regions" of the ductile phase and can be described by continuum finite elements with low stiffness or by element elimination in the completely damaged stage.

In the following models the yield function, Φ, is treated in extension of J_2-plasticity theory so that expressions of the type

$$\Phi = \sigma_{eq} - \bar{D}\sigma_f = 0 \quad \text{or} \quad \hat{\Phi} = \frac{\sigma_{eq}}{\bar{D}} - \sigma_f = 0 \quad \text{or} \quad \tilde{\Phi} = \frac{\sigma_{eq}}{\sigma_f} - \bar{D} = 0 \quad (2.8)$$

may be used to describe the yield condition. Here σ_{eq} stands for the von Mises equivalent stress, σ_f is the flow stress, and $\bar{D}$ is a parameter that indicates the progress of damage and varies between 1 and 0. $\bar{D}$ depends on different variables, like the void volume fraction, f, the equivalent plastic strain, ε_{eq}^{pl}, the mean stress, σ_m, or the stress triaxiality, $\eta = \sigma_m/\sigma_{eq}$, and a number of material parameters, m_i, specific to the applied model. A completely damage-free material (i.e. one in which no voids are present) is indicated by $\bar{D} = 1$ and is treated by standard J_2-plasticity theory. When $\bar{D}$ reaches zero, ductile failure occurs and the von Mises stress, σ_{eq}, vanishes at the same time, so that the term $\sigma_{eq}/\bar{D}$ in eqn. (2.8) remains finite. The increasing or decreasing of the equivalent stress, σ_{eq}, depends on the development of $\bar{D}$, which gives rise to softening, and the flow stress, σ_f, which represents the hardening term in the yield function. The actual behavior accordingly depends on the "competition" between hardening and softening terms. Figure 2.10 shows a typical evolution of the involved variables during deformation driven by a continuum damage model. Note that the above definitions differ from the ones commonly used for damage parameters in continuum damage mechanics.

Formally, the ductile damage models discussed in the following differ only in the definition of $\bar{D}$, with the mean stress, σ_m, (and, consequently, the stress triaxiality, $\eta = \sigma_m/\sigma_{eq}$) playing an important role in determining $\bar{D}$ in most of the models. For this reason these models can be classified as pressure-dependent plasticity models, in which the first invariant of the

stress tensor must be considered in order to obtain a closed yield surface in stress space.
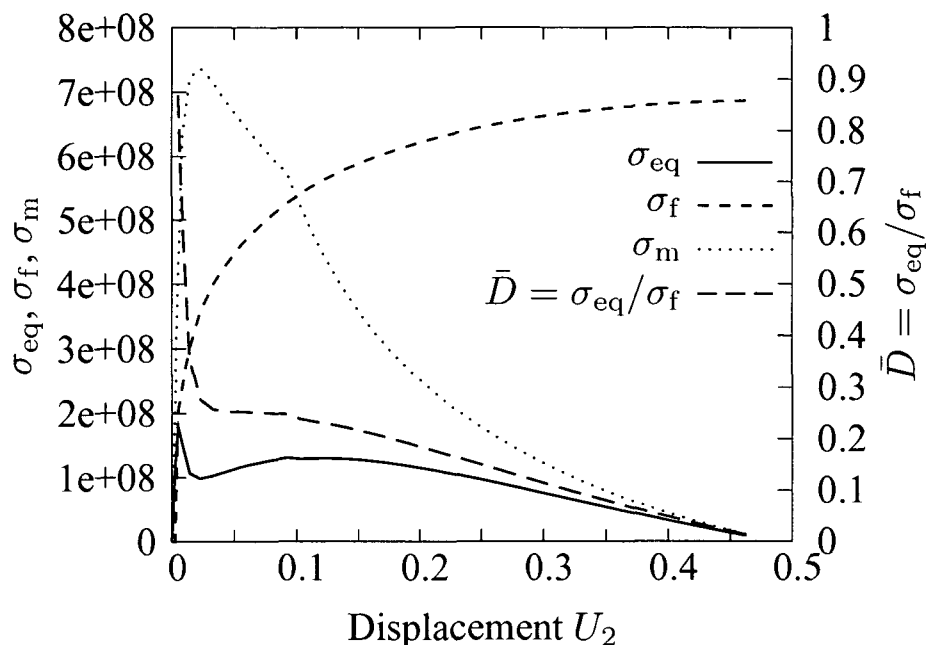
Figure 2.10: Typical evolution of σ_m, σ_{eq}, σ_f and $\bar{D}$ during deformation

2.3.1 Ductile Damage Indicators

Ductile damage indicators, D, have been widely used in the literature, especially due to their simple handling and the low number of material parameters they require. The main idea of such models is to indicate the failure of a material point, if the value of the ductile damage indicator is equal to or exceeds a critical value. Once this point is reached in a "standard" elastoplastic analysis, the simulation must be stopped because the damaged region would influence the behavior of the entire structure due to stress redistribution.

For this reason the idea of element removal techniques for simulating crack propagation based on damage indicators, see e.g. Wulf et al. [26], arose about a decade ago. In such algorithms a material point where the ductile damage indicator, D, exceeds a critical value, D_{crit}, is treated as failed. The stiffness and strength of the corresponding element is then drastically reduced or the element is removed from the mesh if such an option is

provided. Accordingly, $\bar{D}$ as defined in eqn. (2.8) takes the form

$$\bar{D} = \begin{cases} 1 & \text{for} \quad D < D_{\text{crit}} \\ 0 & \text{for} \quad D \geq D_{\text{crit}} \end{cases} . \tag{2.9}$$

A number of different ductile damage indicators have been proposed in the literature and the most important ones will be described in the following.

Cockcroft and Latham [27] assumed that fracture in ductile materials occurs when the integrated value

$$D_{\text{CL}} = \int_0^{\varepsilon_{\text{eq,f}}^{\text{pl}}} \sigma_{\text{I}} d\varepsilon_{\text{eq}}^{\text{pl}} \tag{2.10}$$

equals or exceeds a critical value, D_{crit}. Here σ_{I} stands for the maximum instantaneous principal stress and $\varepsilon_{\text{eq}}^{\text{pl}}$ for the accumulated equivalent plastic strain whereas $\varepsilon_{\text{eq,f}}^{\text{pl}}$ describes the equivalent plastic strain at failure.

Another ductile damage indicator was proposed by McClintock [28] who observed the micro voids in detail. In his work an integral containing two principal stresses σ_{I} and σ_{II} was determined. The ductile damage indicator in this model is defined as follows,

$$D_{\text{McC}} = \int_0^{\varepsilon_{\text{eq,f}}^{\text{pl}}} \left(\frac{\sqrt{3}}{2(1-n)} \sinh \left[\frac{\sqrt{3(1-n)}}{2} \frac{\sigma_{\text{I}} + \sigma_{\text{II}}}{\sigma_{\text{eq}}} \right] + \frac{3}{4} \frac{\sigma_{\text{I}} - \sigma_{\text{II}}}{\sigma_{\text{eq}}} \right) d\varepsilon_{\text{eq}}^{\text{pl}}, \tag{2.11}$$

where n stands for the hardening exponent.

The importance of the stress triaxiality $\sigma_{\text{m}}/\sigma_{\text{eq}}$ in the void nucleation and growths process in ductile materials is evident in the ductile damage indicator criterion of Ayada et al. [29]

$$D_{\text{Ay}} = \int_0^{\varepsilon_{\text{eq,f}}^{\text{pl}}} \frac{\sigma_{\text{m}}}{\sigma_{\text{eq}}} d\varepsilon_{\text{eq}}^{\text{pl}} \tag{2.12}$$

and in the one introduced by Oyane [30]

$$D_{\text{Oy}} = \int_0^{\varepsilon_{\text{eq,f}}^{\text{pl}}} \left(1 + A_{\text{f}} \frac{\sigma_{\text{m}}}{\sigma_{\text{eq}}} \right) d\varepsilon_{\text{eq}}^{\text{pl}} \tag{2.13}$$

which employs an additional material parameter A_{f}. A semi-empirical damage indicator using the maximum stress and the mean stress was formulated by Brozzo et al. [31] and takes the form

$$D_{\text{Br}} = \int_0^{\varepsilon_{\text{eq,f}}^{\text{pl}}} \frac{2\sigma_{\text{I}}}{3(\sigma_{\text{I}} - \sigma_{\text{m}})} d\varepsilon_{\text{eq}}^{\text{pl}}. \tag{2.14}$$

The ductile damage indicator most commonly used in continuum micromechanics was introduced by Gunawardena et al. [32] for assessing the vulnerability of structures to ductile failure on the basis of postprocessing operations after "standard" elastoplastic FE runs. This damage indicator, which is based on work of Rice and Tracey [33] and of Hancock and Mackenzie [34] and was thoroughly studied by Fischer et al. [35] concentrates on void growth and is capable of accounting for the history of the loads acting at any given point in an elastoplastic material. It can be written as

$$
D_{\mathrm{Gu}} = \int_0^{\varepsilon_{\mathrm{eq,f}}^{\mathrm{pl}}} \frac{d\varepsilon_{\mathrm{eq}}^{\mathrm{pl}}}{\varepsilon_{\mathrm{eq,crit}}^{\mathrm{pl}}(\eta)} = \int_0^{\varepsilon_{\mathrm{eq,f}}^{\mathrm{pl}}} \frac{\exp\left(\frac{3}{2}\eta\right)}{1.65\varepsilon_0} d\varepsilon_{\mathrm{eq}}^{\mathrm{pl}}, \tag{2.15}
$$

where $\eta = \sigma_{\mathrm{m}}/\sigma_{\mathrm{eq}}$ is the stress triaxiality also considered in this model. The reference failure strain, ε_0, acting as a material parameter in this ductile damage indicator can be calibrated by appropriate tensile tests. This model is also known in the literature as the Rice–Tracey damage model.

The main idea of this ductile damage indicator is evident in fig. 2.11, where, on the left side, the critical equivalent plastic strain, $\varepsilon_{\mathrm{eq,crit}}^{\mathrm{pl}}$, is shown in dependence of the triaxiality, η, (failure curve) and two points, one of them representing the corresponding stress state with $d\varepsilon_{\mathrm{eq}}^{\mathrm{pl}}$ and η and the second giving the critical value of $\varepsilon_{\mathrm{eq}}^{\mathrm{pl}}$ for the actual triaxiality, η, (lying on the failure curve). On the right side, the figure depicts a Wöhler diagram used for cyclic loading in a mechanical component at the macroscale, that can be seen as an analogy to the above ductile damage indicator and is mentioned in this context for a better understanding of eqn. (2.15) only. In the Wöhler concept, the critical number of load cycles, $\tilde{N}_{\mathrm{crit}}$, depends on the applied stress amplitude, σ_{a}, and final failure of the specimen at cycle number $\tilde{N}_{\mathrm{f}}$ is given by

$$
D_{\mathrm{Wo}} = \int_0^{\tilde{N}_{\mathrm{f}}} \frac{d\tilde{N}}{\tilde{N}_{\mathrm{crit}}(\sigma_{\mathrm{a}})} = 1. \tag{2.16}
$$

The diagram shows the Wöhler line and the considered cycles, $d\tilde{N}$, and the corresponding critical cycle number, $\tilde{N}_{\mathrm{crit}}$, for the present stress amplitude, σ_{a}, both used in eqn. (2.16).

A comparison of the above ductile damage indicators shows that D_{CL}, eqn. (2.10), has the dimensions of a strain energy density, whereas D_{McC}, D_{Ay}, D_{Oy}, D_{Br}, D_{Gu}, eqn. (2.11) to (2.15) are dimensionless numbers.

The material behavior enters into D_{CL}, D_{McC}, D_{Ay}, D_{Oy} and D_{Br} via the critical values of the damage indicators, which are different for each expression and are difficult to evaluate experimentally. D_{Gu}, however, is formulated on the basis of Rice and Tracey's void growth

model such that the critical value is unity[1] and the material behavior enters via the reference strain, ε_0, which can be directly evaluated experimentally, see Fischer et al. [35].

The latter property is the main reason why D_{Gu} has seen much more use in micromechanical studies than other ductile damage indicators and also forms the basis of one of the present implementations.

Models that use a ductile damage indicator, especially eqn. (2.15), to trigger "element death", either by setting the stiffness to very low values or by removing the element from the mesh, are referred to as ductile damage indicator triggered (DDIT) models in the following.

It is worth noting, however, that the above damage indicators cannot be correlated to physical levels of damage, e.g. void volume fractions, in the range $0 < D < D_{\mathrm{crit}}$ and the material is described by standard J_2 plasticity within this range in contrast to the damage progress models described in the next section.
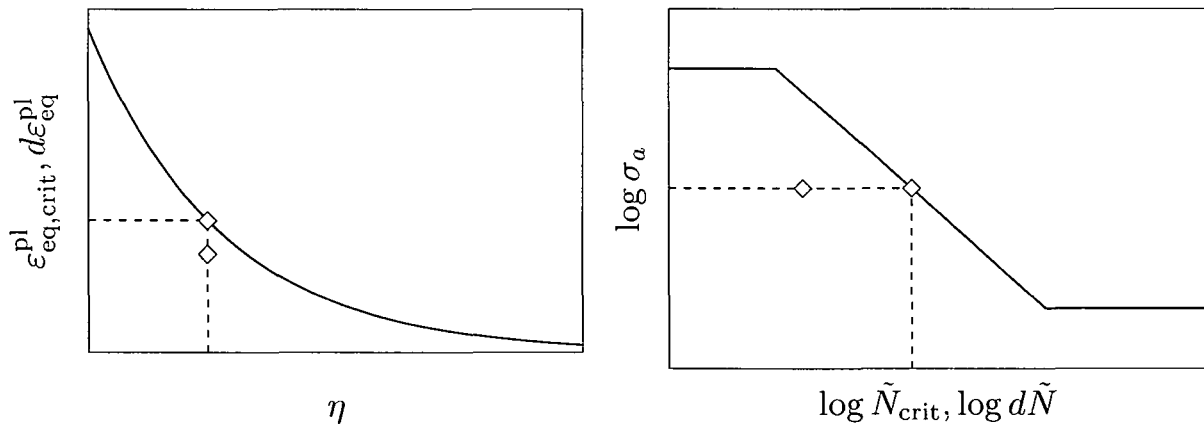
Figure 2.11: Failure curve related to the damage indicator based on Gunawardena [32] (left) in analogy to the Wöhler diagram (right)

2.3.2 Damage Progress Models

A second approach for describing growth and coalescence of voids in ductile materials consists in modifying the von Mises yield function in dependence on the volume fraction of the voids, f. Such "ductile rupture" models can be adapted to account for void nucleation

---

[1]In some works reported in the literature the critical value for D_{Gu} has been used as an additional material parameter to fit experimental data, see e.g. Bernauer and Brocks [36].

as well.

The best known model of this type was developed by Gurson [37] and was extended by Tvergaard [38] as well as Tvergaard and Needleman [39] to include effects of void nucleation and coalescence. For the resulting GTN model the parameter $\bar{D}$ according to eqn. (2.8) can be denoted as

$$\bar{D} = \sqrt{-2q_1 f^* \cosh\left(\frac{3q_2\,\sigma_\mathrm{m}}{2\sigma_\mathrm{f}}\right) + 1 + q_3 f^{*2}}, \qquad (2.17)$$

where σ_f is the flow stress and q_1, q_2 as well as q_3 are adjustable parameters. The internal variable f^* accounts for the rapid loss of stiffness due to void coalescence beyond some critical volume fraction, f_c, and is defined as

$$f^* = \begin{cases} f & \text{for} \quad f \le f_\mathrm{c} \\ f_\mathrm{c} + \hat{K}\,(f - f_\mathrm{c}) & \text{for} \quad f > f_\mathrm{c} \end{cases}, \qquad (2.18)$$

where $\hat{K}$ is a function of f_c and of the void volume fraction at failure, f_f.

The rate of increase of the void volume fraction consists of two contributions, nucleation of new voids and growth of existing voids, which can be approximated as

$$\dot{f} = A\dot{\varepsilon}_\mathrm{eq}^\mathrm{pl} + (1 - f)\,\dot{\varepsilon}_\mathrm{p}, \qquad (2.19)$$

where $A(\varepsilon_\mathrm{eq}^\mathrm{pl})$ is a material parameter. $\dot{\varepsilon}_\mathrm{p}$ stands for the rate of the first invariant of the plastic strain tensor, $\boldsymbol{\varepsilon}^\mathrm{pl}$.

Gurson-like models incorporating the influence of void shape (ellipsoidal voids) were given by Gologanu et al. [40] and by Pardoen and Hutchinson [41], where the critical void volume fraction, f_c, is not treated as a constant and can be calculated in dependence on the triaxiality, the microstructure of the voids and on the deformation state of the material.

An alternative approach for describing ductile damage and failure was proposed by Rousselier [42] in the form of a thermodynamically based continuum damage mechanics method. For this model $\bar{D}$ takes the form (Rousselier [43])

$$\bar{D} = \rho - \rho\frac{\sigma_1}{\sigma_\mathrm{f}}f\tilde{D}\exp\left(\frac{\sigma_\mathrm{m}}{\rho\sigma_1}\right), \qquad (2.20)$$

where the variable ρ is defined as $\rho = (1 - f)/(1 - f_0)$, f_0 is the initial porosity of the ductile material, and σ_1 as well as $\tilde{D}$ are material parameters. The material loses its stress carrying capacity when a void volume fraction of f_F is reached. The rate of increase of the void volume fraction can be calculated in analogy to the GTN model, but to handle void coalescence an additional variable B may be introduced into eqn. (2.19) as proposed

in Rousselier [43] to give

$$\dot{f} = A\dot{\varepsilon}_{eq}^{pl} + (1 - f) B\dot{\varepsilon}_{p}, \tag{2.21}$$

$$B = \begin{cases} 1 & \text{for } f \leq f_c \\ 3 & \text{for } f > f_c \end{cases}.$$

Another isotropic continuum damage model available in the literature was derived by Lemaître [44], [45] in a thermodynamical framework by using the concept of effective stress written as

$$\tilde{\sigma} = \frac{\sigma}{1 - f}, \tag{2.22}$$

where f is the void volume fraction, and serves as the damage variable of the model. It is defined as

$$f = \frac{f_c}{\varepsilon_R - \varepsilon_D} \left(\varepsilon_{eq}^{pl} \left[\frac{2}{3} (1 + \nu) + 3 (1 - 2\nu) \left(\frac{\sigma_m}{\sigma_{eq}} \right)^2 \right] - \varepsilon_D \right), \tag{2.23}$$

where f_c describes the void volume at failure, ν being the Poisson ratio, and ε_D and ε_R stand for the equivalent plastic strain at damage initiation and final failure, respectively. The parameter $\bar{D}$ in eqn. (2.8) can be written as

$$\bar{D} = \left[\frac{2}{3} (1 + \nu) + 3 (1 - 2\nu) \left(\frac{\sigma_m}{\sigma_{eq}} \right)^2 \right]^{-1/2} \tag{2.24}$$

for the Lemaître model.

2.3.3 Step Size Dependence

The step size dependence of material softening models within an incremental–iterative FEM–framework has not been discussed very often in the literature but should be mentioned and considered before implementation work is started. DDIT models are much more sensitive with respect to this kind of dependence than the damage progress models. The main problem is due to the fact that integration points of the model may fail in an analysis with a large load increment which would never fail if the same simulation were done with a smaller load increment. Such behavior can influence the crack path and the global force–displacement response of the structure, and must be avoided in order to obtain a unique solution. A remedy can be found in a strategy to get the largest possible load increment

where only one integration point (or a small number of integration points) will fail in this increment. If the load increment is chosen excessively small the simulation will take more time and if the load increment is set too large a considerable number of integration points may fail giving rise to a step size dependence of the result. Appropriate algorithms can be implemented in ABAQUS/Standard by checking the number of failed integration points after reaching an equilibrium and repeating the increment with a reduced load increment if more than a specified number of integration points are marked for failure. However, this strategy is practical in models with a small number of integration points only, otherwise the simulation time will increase drastically. Figure 2.12 shows a mesh and the failed elements (rendered in gray) after some increments done with small and large load increments, respectively. A detailed description of a possible procedure to overcome the step size dependence in ABAQUS/Standard is given in Zarco-Gonzalez et al. [46], who triggered the element removing technique in such a way, that only the integration point showing the highest maximum damage variable can be eliminated in any given increment.
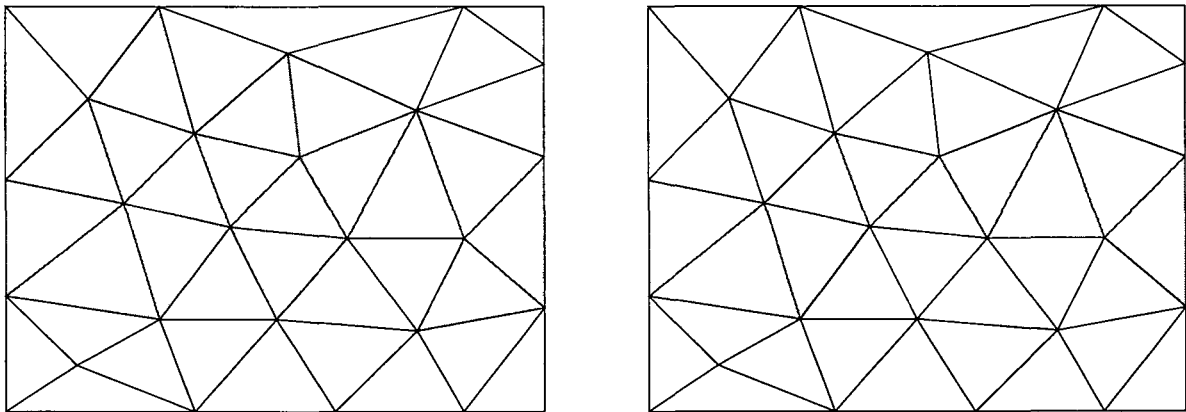

Figure 2.12: Damaged elements (gray) evaluated in large (left) and small (right) load increments showing an example of step size dependence of ductile damage

2.3.4 Mesh Dependence

Among the models discussed in sections 2.3.1 and 2.3.2 a version of the Gurson model is provided in ABAQUS/Standard, and the others can be implemented into this code via

user material subroutines (UMATs). All of these models, however, suffer from the drawback that their results tend to show a marked mesh dependence in terms of both the predicted force–displacement responses and the configurations of the predicted ductile cracks. This behavior is due to the loss of ellipticity of the governing partial differential equations once local softening sets in. The loss of ellipticity is indicated by the acoustic tensor defined by the double contraction

$$Q_{ij} = C_{ijkl}\bar{n}_k\bar{n}_l \tag{2.25}$$

of the tangential material tensor, $\mathbf{C}$, and the normal vector, $\bar{n}$, which indicates possible wave propagation directions, becoming negative definite, see e.g. the discussion by Baaser and Gross [47].

The mesh dependence of the predicted ductile failure behavior can be easily demonstrated by considering a test case that consists of a column of initially rectangular cross section that contains a non-central axial hole of the form of an initially circular cylinder of volume fraction $\xi = 0.8\%$. The arrangement is subjected to tensile loading in the y-direction, constant displacements being prescribed on the y=const boundaries whereas the x=const boundaries are traction free. The column's elastoplastic material behavior is taken to correspond to Al2618-T4, hardening being described by a modified Ludwik law of the type

$$\sigma_f = \sigma_{f,0} + k \cdot (\varepsilon_{eq}^{pl})^n, \tag{2.26}$$

where $\sigma_{f,0}$ is the initial flow stress, k and n stand for the hardening coefficient and the hardening exponent, respectively. For the elastic material parameters and those required for eqn. (2.26) see tab. 2.1, where E stands for the Young's modulus and ν for the Poisson ratio. For testing purposes the following values were employed for the material parameters of the ductile damage models, eqns. (2.15) to (2.20): ε_0=0.2, q_1=1.5, q_2=1.0, q_3=2.25, f_c=0.12, f_f=0.2, f_0=7.0×10^{-3}, f_F=0.9, σ_1=165 MPa and $\tilde{D}$=2.0 (note that these material parameters were not obtained by parameter identification procedures and do not give rise to directly comparable damage responses). Three different meshes, with approximately 2.500, 6.000, and 21.000 quadratic triangular plane strain elements, respectively, were used to check for mesh dependences.

The crack paths predicted for this test case by the DDIT model based on eqn. (2.15) are shown in fig. 2.13. Similar results were obtained with the GTN and Rousselier models, only the former being shown in fig. 2.14. For the GTN model the crack essentially always consists of one row of elements only, i.e. the volume of material affected by ductile failure depends markedly on the FE mesh. The DDIT model, in contrast, displays a tendency for

the mesh dependence to affect the shapes of the cracks in addition to the volume of the failed metal. Figure 2.15 displays the corresponding predicted force–displacement curves, which are normalized with respect to the maximum load carried, $RF_{2,\max}$, and the maximum applied displacement, $U_{2,\max}$. The mesh dependence of the force–displacement paths obtained by both the DDIT and GTN models is evident, with the Rousselier model giving a response very similar to fig. 2.15(b). One can see that the energy required for failure decreases with increasing mesh refinement and the crack propagates earlier and faster in the finer mesh.

Mesh dependence effects of the above type are well known in the literature, see e.g. de Borst et al. [48], and are clearly not acceptable for damage modeling within composite micromechanics.

E [GPa]	ν	$\sigma_{f,0}$ [MPa]	k [MPa]	n
70.0	0.3	184.0	722.7	0.49

Table 2.1: Elastic and elastoplastic material parameters for Al2618-T4

Figure 2.13: Column with a hole under tensile loading in the y–direction: configurations of ductile cracks predicted by the (local) DDIT model for three different meshes
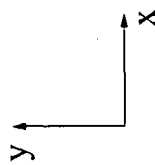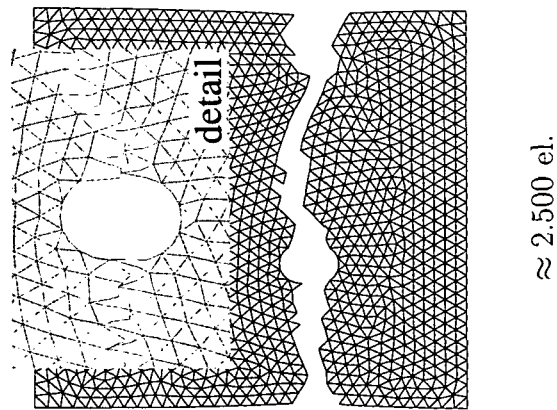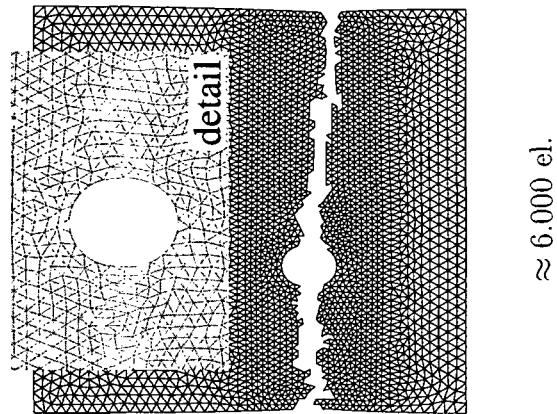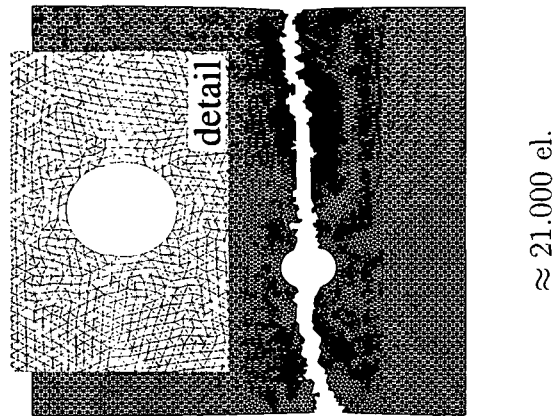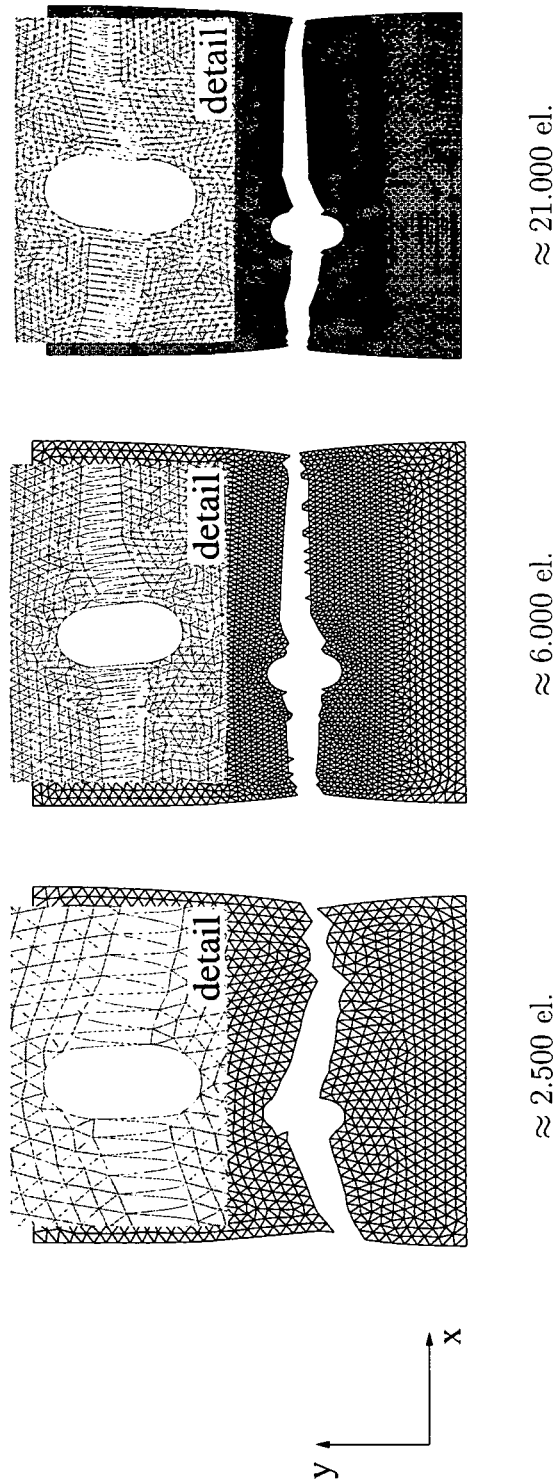
Figure 2.14: Column with a hole under tensile loading in the y–direction: configurations of ductile cracks predicted by the (local) GTN model for three different meshes

(a)

(b)
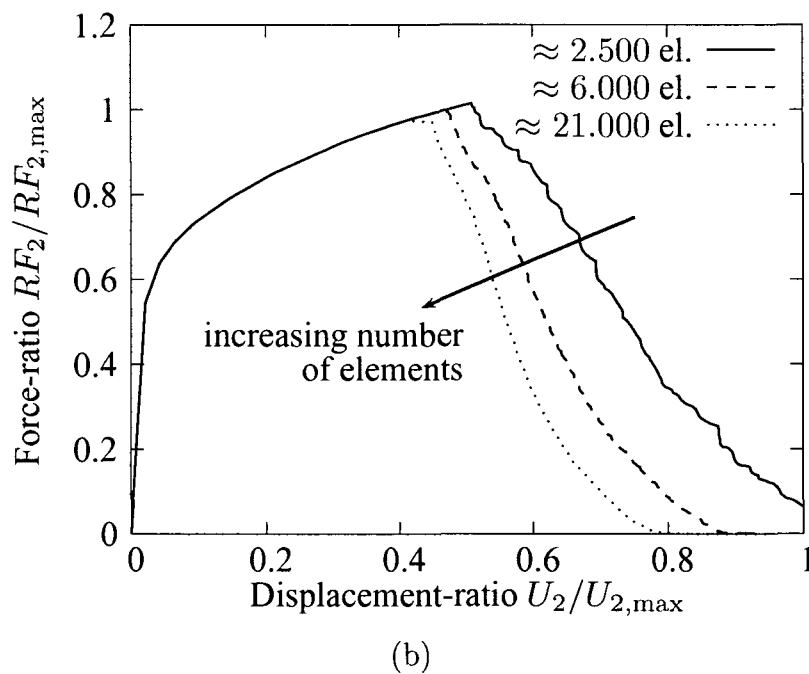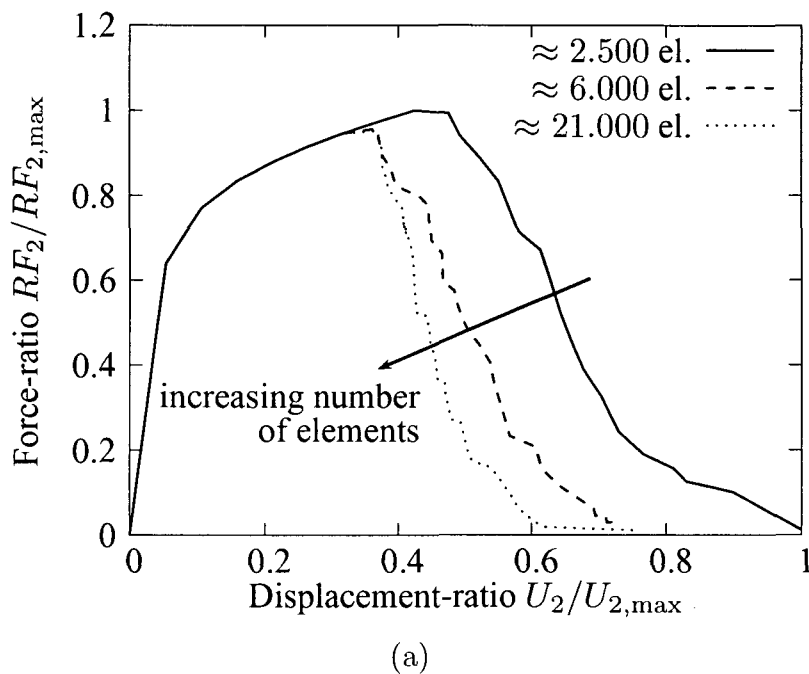
Figure 2.15: Normalized overall force–displacement responses obtained for the column with a hole under loading in vertical direction using local versions of (a) the DDIT model and (b) the GTN model

2.3.5 Regularization Techniques

A number of approaches have been reported in the literature for avoiding the above mesh dependence by regularizing the governing equations. All of them introduce an (absolute) internal length scale (characteristic length) but do so in different ways. Physically this internal length scale of the material may be interpreted as the size of a process zone, as a function of the distance between individual voids, or as the distance between dimples in the fracture surfaces. Publications on the calibration of characteristic lengths are rare and it seems that there are only two approaches to tackle this problem. On the one hand, the calibration can rely on inverse analysis (Bellègo et al. [49]). In this procedure, analyses with different sets of material parameters (the internal length being treated as "ordinary" material parameter as well) must be performed and compared with experimental results. Preferentially an optimization tool is used to provide suggestions for the next set of material parameters to attain a fast convergence between experiment and simulation. On the other hand, models employing resolved voids of defined distance – which defines a length scale – can be compared with smeared-out models employing nonlocal damage descriptions to evaluate a characteristic length, see Tvergaard and Needleman [50] and Tvergaard and Hutchinson [51].

In addition, there are questions about the evolution of the characteristic length during the deformation of the material. In most of the works in the literature this value is held constant, whereas the idea of a growing internal length scale that depends on the void volume fraction, f, on some other damage variable (Ferrara and di Prisco [52]), or on the equivalent plastic strain, ε_{eq}^{pl}, (Pijaudier-Cabot [53]) has arisen in the past years.

The most important localization limiter techniques will be explained in the following.

Integral-type Nonlocal Method

Nonlocal theories are based on the assumption that the local state of the material at any point is insufficient for evaluating damage relevant parameters in that point. This can be explained by the fact that no real material is an ideal continuum and that on a sufficiently small length scale the effects of heterogeneity and discontinuous microstructure become nonnegligible. For further discussions about the necessity of nonlocal models see Pijaudier–Cabot and Bažant [54] as well as Bažant [55].

Integral-type nonlocal methods are based on smoothing the rate of an appropriate damage variable $\dot{q}$ for a material point located at $\mathbf{x}$ by a moving averaging scheme taking into

account the adjacent material points placed at positions $\mathbf{y}$. Leblond et al. [56] proposed a relationship of the form

$$\dot{q}_{\mathrm{NL}}(\mathbf{x}) = \frac{1}{W(\mathbf{x})} \int\limits_V \dot{q}_{\mathrm{L}}(\mathbf{y}) w(\mathbf{x}, \mathbf{y}, L) dV \tag{2.27}$$

for nonlocal averaging with the normalizing factor $W(\mathbf{x})$ being defined as

$$W(\mathbf{x}) = \int\limits_V w(\mathbf{x}, \mathbf{y}, L) dV. \tag{2.28}$$

Here $\dot{q}_{\mathrm{L}}$ and $\dot{q}_{\mathrm{NL}}$ are the rates of the local and nonlocal damage variables, respectively. As mentioned above, such approaches introduce an additional material parameter in the form of a characteristic length $2L$. Two smoothing functions have been frequently used in the literature. The first one

$$w(\mathbf{x}, \mathbf{y}, L) = \left[\frac{1}{1 + \left(\frac{z(\mathbf{x}, \mathbf{y})}{L} \right)^8} \right]^2 \tag{2.29}$$

follows Tvergaard and Needleman [39], and the second is a Gauss distribution (see e.g. Bažant and Pijaudier–Cabot [57])

$$w(\mathbf{x}, \mathbf{y}, L) = \frac{1}{(2\pi)^{3/2} L^3} \exp\left[-\frac{z^2(\mathbf{x}, \mathbf{y})}{2L^2} \right]. \tag{2.30}$$

Here

$$z(\mathbf{x}, \mathbf{y}) = |\mathbf{x} - \mathbf{y}| \tag{2.31}$$

is the distance between the points $\mathbf{x}$ and $\mathbf{y}$. The factor $(2\pi)^{-3/2} L^{-3}$ in eqn. (2.30) normalizes the function $W(\mathbf{x})$ in eqn. (2.28).

Both smoothing functions are depicted in fig. 2.16. Successful implementations and applications for this kind of regularization technique in damage mechanics and plasticity can be found e.g. in Tvergaard and Needleman [39], Tvergaard and Needleman [58], Chambert et al. [59], Baaser and Tvergaard [60], Jackiewicz and Kuna [61], Comi and Perego [62] as well as Rodrìguez-Ferran et el. [63].
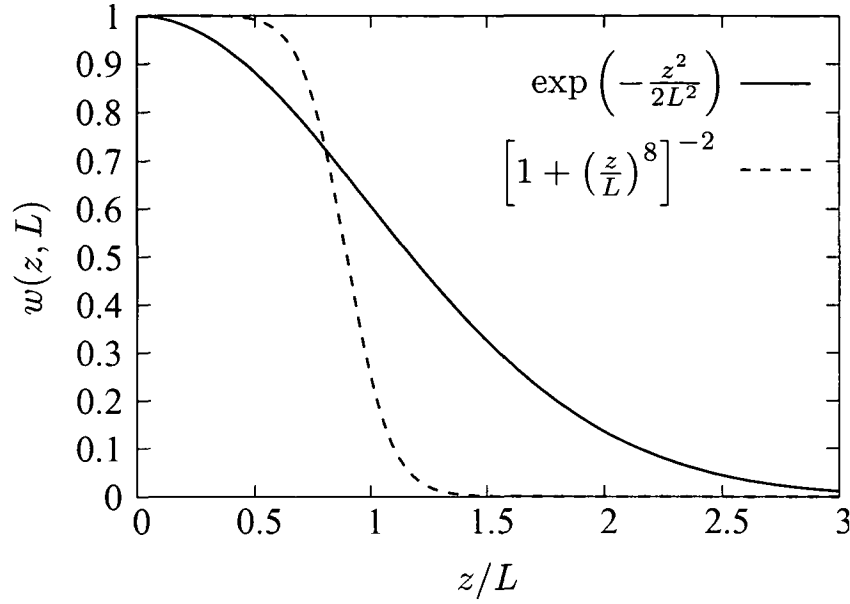
Figure 2.16: Two smoothing functions for the nonlocal approach ([39], [57])

Gradient-type Method

A second regularization technique can be used if the rate of the damage variable $\dot{q}$ is sufficiently smooth. In that case the integral relation in eqn. (2.27) can be rewritten in terms of gradients of $\dot{q}$ by expanding $\dot{q}_L(\mathbf{y})$ into a Taylor series (Bažant et al. [64] and Peerlings et al. [65])

$$\dot{q}_L(\mathbf{y}) = \dot{q}_L(\mathbf{x}) + \frac{\partial \dot{q}_L}{\partial x_i}(y_i - x_i) + \frac{1}{2!}\frac{\partial^2 \dot{q}_L}{\partial x_i \partial x_j}(y_i - x_i)(y_j - x_j) + \qquad (2.32)$$

$$+ \frac{1}{3!}\frac{\partial^3 \dot{q}_L}{\partial x_i \partial x_j \partial x_k}(y_i - x_i)(y_j - x_j)(y_k - x_k) + \ldots$$

Using, for example, the Gauss distribution for the smoothing function w, eqn. (2.30), and substituting the Taylor series, eqn. (2.32), into eqn. (2.27) yields after some calculations

$$\dot{q}_{NL}(\mathbf{x}) = \dot{q}_L(\mathbf{x}) + \frac{1}{2}L^2 \nabla^2 \dot{q}_L(\mathbf{x}) + \frac{1}{8}L^4 \nabla^4 \dot{q}_L(\mathbf{x}) + \ldots \qquad (2.33)$$

where the Laplacian ∇^n is defined by $\nabla^2 = \sum_i \partial^2/\partial x_i^2$ and $\nabla^{2n} = (\nabla^2)^n$. Some of the expressions resulting from the substitution were evaluated by Mathematica [66] and are

given in appendix A. All odd derivative terms in eqn. (2.33) vanish as a result of the isotropy of the weight function. By neglecting terms of order four and higher we obtain

$$\dot{q}_{NL}(\mathbf{x}) = \dot{q}_{L}(\mathbf{x}) + \frac{1}{2}L^2\nabla^2\dot{q}_{L}(\mathbf{x}) \tag{2.34}$$

which is an explicit gradient formulation that may be used as a smoothing procedure to overcome the mesh dependence.

An alternative gradient formulation that can be found in the literature can be derived from eqn. (2.34) by applying the Laplacian operator ∇^2 to it, multiplying by $L^2/2$, and subtracting the result from eqn. (2.34)

$$
\begin{aligned}
\dot{q}_{NL}(\mathbf{x}) - \frac{1}{2}L^2\nabla^2\dot{q}_{NL}(\mathbf{x}) &= \dot{q}_{L}(\mathbf{x}) + \frac{1}{2}L^2\nabla^2\dot{q}_{L} - \\
&\quad \frac{1}{2}L^2\nabla^2\dot{q}_{L} - \frac{1}{4}L^4\nabla^4\dot{q}_{L}(\mathbf{x}) \\
&= \dot{q}_{L}(\mathbf{x}) - \frac{1}{4}L^4\nabla^4\dot{q}_{L}(\mathbf{x}).
\end{aligned}
\tag{2.35}
$$

By neglecting terms of order four and higher again, we obtain the implicit gradient formulation

$$\dot{q}_{NL}(\mathbf{x}) - \frac{1}{2}L^2\nabla^2\dot{q}_{NL}(\mathbf{x}) = \dot{q}_{L}(\mathbf{x}). \tag{2.36}$$

Accordingly, the gradient formulations can be viewed as approximations to the integral-type nonlocal method and should be used in situations with a smooth $\dot{q}$-field only. Applications of the explicit and implicit gradient formulations are presented in de Borst and Mühlhaus [67], Kuhl and Ramm [68], Peerlings et al. [69], Addessi et al. [70], Engelen et al. [71], Yuan and Chen [72] as well as Voyiadjis and Dorgan [73]. An extended Gurson-based ductile damage model with a gradient-type regularization technique implemented into ABAQUS/Standard was published by Reusch et al. [74], where the temperature field variable is used for the nonlocal damage variable and for evaluating the necessary gradient field.

Overviews on nonlocal and gradient formulations of plasticity and damage are given in de Borst [75], Peerlings et al. [76], Bažant and Jirásek [77] and Jirásek and Rolshoven [78].

Viscoplastic Regularization

A further possibility for keeping the field equations well posed consists of the introduction of viscous terms into the governing equations (temporal gradients instead of spatial gradients)

as shown in Needleman [79], Harireche and Loret [80] and Loret et al. [81]. The viscoplastic regularization procedure first proposed by Duvaut and Lions [82] retains the hyperbolicity of the system and allows the development of shear-bands in plasticity or of a process zone in continuum damage mechanics of finite thickness. A characteristic length

$$L = c_s^e \zeta, \tag{2.37}$$

is defined by the elastic wave speed, c_s^e, and by the relaxation time, ζ. As observed in Loret et al. [81] the width of shear-bands is influenced by this viscoplastic regularization technique and is typically of the order of $10L$. The introduction of rate dependence has been claimed to have a regularization effect not only in dynamic analyses but also in the quasi-static analyses where inertia terms can be neglected, see Sluys and Wang [83], who also tested a combination of the viscous and gradient regularization. This claim, however, may be open to discussion in view of the observations in Wang and Sluys [84], where mesh dependence reappeared despite of the use of viscoplastic regularization at very low displacement rates and mesh independent results were obtained only at high strain rates.

Cosserat Continuum

A completely different approach to nonlocal theories was first proposed by the Cosserat brothers [85] in 1909, the first implementation of the theory into a finite element code being reported by de Borst [86]. This theory has two main characteristics. First, rotational degrees of freedom are taken into account in addition to the translational ones and lead to the existence of momentum stresses (momentum per area). Second, an internal length scale that couples stresses to micro-curvature is introduced into the constitutive equations. To give a short introduction the equations of the general theory of elastic two-dimensional Cosserat continuum are given in the following. In this case one rotational degree of freedom, α_3, around the 3 axis is used in addition to the traditional degrees of freedom u_1 and u_2. The normal and shear strains in a Cosserat continuum are defined as

$$\varepsilon_{11} = \frac{\partial u_1}{\partial x_1}, \tag{2.38}$$

$$\varepsilon_{22} = \frac{\partial u_2}{\partial x_2}, \tag{2.39}$$

$$\varepsilon_{12} = \frac{\partial u_2}{\partial x_1} - \alpha_3, \tag{2.40}$$

$$\varepsilon_{21} = \frac{\partial u_1}{\partial x_2} + \alpha_3. \tag{2.41}$$

In contrast to the classical continuum, the micro-curvatures

$$\kappa_{13} = \frac{\partial \alpha_3}{\partial x_1}, \tag{2.42}$$

$$\kappa_{23} = \frac{\partial \alpha_3}{\partial x_2}, \tag{2.43}$$

are introduced that are conjugate to the couple stress components (m_{12} and m_{23}) of the stress tensor. The force and momentum equilibrium then yields:

$$\frac{\partial \sigma_{11}}{\partial x_1} + \frac{\partial \sigma_{21}}{\partial x_2} = 0 \tag{2.44}$$

$$\frac{\partial \sigma_{12}}{\partial x_1} + \frac{\partial \sigma_{22}}{\partial x_2} = 0 \tag{2.45}$$

$$\frac{\partial m_{13}}{\partial x_1} + \frac{\partial m_{23}}{\partial x_2} - \sigma_{21} + \sigma_{12} = 0 \tag{2.46}$$

As can be seen from eqn. (2.46), the stress tensor is generally not symmetric due to the presence of couple stresses. The internal length scale, L, appears in the vectors of the stress and strain components, as

$$\boldsymbol{\varepsilon} = [\varepsilon_{11}, \varepsilon_{22}, \varepsilon_{33}, \varepsilon_{12}, \varepsilon_{21}, \kappa_{13}L, \kappa_{23}L]^T, \tag{2.47}$$

$$\boldsymbol{\sigma} = [\sigma_{11}, \sigma_{22}, \sigma_{33}, \sigma_{12}, \sigma_{21}, m_{13}L, m_{23}L]^T. \tag{2.48}$$

$$\tag{2.49}$$

The linear elastic stiffness matrix is defined as

$$\mathbf{C}^e = \frac{E}{(1+\nu)} \begin{bmatrix} \frac{1-\nu}{1-2\nu} & \frac{\nu}{1-2\nu} & \frac{\nu}{1-2\nu} & 0 & 0 & 0 & 0 \\ \frac{\nu}{1-2\nu} & \frac{1-\nu}{1-2\nu} & \frac{\nu}{1-2\nu} & 0 & 0 & 0 & 0 \\ \frac{\nu}{1-2\nu} & \frac{\nu}{1-2\nu} & \frac{1-\nu}{1-2\nu} & 0 & 0 & 0 & 0 \\ 0 & 0 & 0 & \frac{1}{2}+m_C & \frac{1}{2}-m_C & 0 & 0 \\ 0 & 0 & 0 & \frac{1}{2}-m_C & \frac{1}{2}+m_C & 0 & 0 \\ 0 & 0 & 0 & 0 & 0 & 1 & 0 \\ 0 & 0 & 0 & 0 & 0 & 0 & 1 \end{bmatrix} \tag{2.50}$$

where m_C is an additional material parameter.

Finite elements taking into account the additional rotational degrees of freedom can be implemented into ABAQUS/Standard via the user element subroutine utility (UEL), see e.g. Alsaleh [87] and Grammenoudis [88], who used elastoplastic constitutive laws in their implementations.

The approach of the Cosserat theory is a promising tool for avoiding mesh dependence

in softening materials, after strain localization has set in, when the finite element method is used. A problem, however, is that the rotational degrees of freedom are activated under shear loading only and will be inactive under pure tension. In that case the micro-curvatures remain zero and the couple stresses vanish. Numerical experiments suggest that, when decohesion is the predominant failure mode rather than frictional slip, the Cosserat effect is generally too "weak" to preserve ellipticity of the boundary value problem (de Borst and Mühlhaus [67]).

Ad-hoc Method

The last method for dealing with mesh dependence presented here consists in adjusting the mesh size to an appropriate characteristic length, $2L$. This method cannot be seen as a localization limiter but can be found very often in the literature if no regularization technique is available, see e.g. Reusch et al. [89], Bernauer and Brocks [36], Hambli [90], Imad [91] as well as Nègre et al. [92]. This method can be used with reasonable success only if the generation of a regular mesh with constant element size is possible for the structure to be studied and if the stress and strain gradients are small. If the finite elements contain more than one integration point the process zone will localize in one row of integration points (only a part of the finite elements being involved in the failure process) and the edge length of the elements no longer corresponds to the characteristic length.

This kind of ad-hoc approach is not suitable for analyses in metal matrix composites at the micro-scale due to the irregular meshes typically used and the high gradients of the microfields typically encountered.

General Remarks

As mentioned above nonlocal damage laws explicitly introduce an absolute length scale into finite element models. This is of special interest in continuum micromechanics, where nearly all standard approaches are inherently scale independent (the main exception being certain embedded cell models that study the tips of macrocracks), whereas experimental results typically show a dependence of the overall elastoplastic and damage behavior on the size of the reinforcements. Material models that introduce an absolute length scale into micromechanical schemes are the only physically consistent means for resolving this

situation.

It is also interesting to note that continuum micromechanical studies of ductile matrix composites are a nearly ideal field of application of nonlocal ductile damage models because the microscale of the composite and the size of pertinent process zones are typically comparable. This allows, on the one hand, to use homogenized damage models with good confidence, while, on the other hand, finite element meshes that are sized for capturing the stress and strain fluctuations on the composites' microscale usually are sufficiently fine to have a reasonable number of integration points within the nonlocal scheme's region of influence. Nonlocal averaging schemes are less well suited for macromechanical applications, where the mesh size would be driven by the requirements on nonlocal averaging which would give rise to an excessive number of degrees of freedom.

Chapter 3

Implementation of the Ductile Damage Models into ABAQUS/Standard

The implementation of the DDIT model, the Gurson-Tvergaard-Needleman (GTN) model and the Rousselier model into ABAQUS/Standard with a nonlocal regularization technique will be discussed in the following. The user defined material subroutine (UMAT) provided in ABAQUS/Standard for applying user-written material laws is employed for this purpose. In addition, the DDIT model can be handled via a user defined field subroutine (USDFLD[1]) as well, which in many cases provides convergence within a smaller number of iterations than the UMAT implementation. A further user defined subroutine (UEXTERNALDB) is necessary for handling the nonlocal approach.

The meaning of the "colon" and the "dot" operators used in the following depends on the order of the tensors involved and is given by

$$\mathbf{A} : \mathbf{B} = A_{ij} B_{ij}, \tag{3.1}$$

$$(\mathbf{A} : \mathbf{B})_{ij} = A_{ijkl} B_{kl}, \tag{3.2}$$

$$(\mathbf{A} : \mathbf{B})_{ijkl} = A_{ijmn} B_{mnkl}, \tag{3.3}$$

---

[1]The USDFLD user subroutine in ABAQUS/Standard allows the user to define material properties (e.g. the Young's modulus) depending on the spatial location and the local material state.

and

$$(\mathbf{A} \cdot \mathbf{B})_{ik} = A_{ij} B_{jk}. \tag{3.4}$$

The symbol $\otimes$ indicates the dyadic tensor product, e.g.

$$(\mathbf{A} \otimes \mathbf{B})_{ijkl} = A_{ij} B_{kl}. \tag{3.5}$$

3.1 Return Mapping Algorithm

Return mapping algorithms are necessary tools in nonlinear analyses involving incremental plasticity models with or without damage. They serve to find stress updates if the yield condition is violated.

The implementation of new material models into ABAQUS/Standard can be carried out by a user defined material subroutine, called UMAT, and must be written in FORTRAN code. The most important variables that are passed into the UMAT, and can be accessed by the user, are the stress tensor, $\boldsymbol{\sigma}$, the strain tensor, $\boldsymbol{\varepsilon}$, and the increment of the strain tensor, $\Delta \boldsymbol{\varepsilon}$, at the beginning of an increment. The user must provide an algorithm to compute the stress tensor, $\boldsymbol{\sigma}$, at the end of the increment as well as the (hopefully consistent) tangent matrix (Jacobian)

$$\mathbf{C}^{\mathrm{cons}} = \frac{\partial \Delta \boldsymbol{\sigma}}{\partial \Delta \boldsymbol{\varepsilon}} \tag{3.6}$$

of the constitutive model. The derivation of a consistent tangent matrix, $\mathbf{C}^{\mathrm{cons}}$, will be described in section 3.3. The update of the stress tensor, $\boldsymbol{\sigma}$, for pressure-dependent elastoplastic models proposed by Aravas [93] was applied in this work and will be discussed in more detail in the following, some corrections with respect to the original paper by Aravas being introduced.

When dealing with elastoplastic material models, the deformation gradient, $\mathbf{F}$, can be split into elastic and plastic contributions. In general one can write

$$\mathbf{F} = \mathbf{F}^{\mathrm{el}} \cdot \mathbf{F}^{\mathrm{pl}}, \tag{3.7}$$

where

$$\mathbf{F} = \frac{\partial \mathbf{x}}{\partial \mathbf{X}} \tag{3.8}$$

is a tensor of second order describing the total deformation gradient with $\mathbf{x}$ and $\mathbf{X}$ being the actual and the initial position of the point under consideration, respectively, $\mathbf{F}^{\mathrm{el}}$ is

the fully recoverable contribution and $\mathbf{F}^{\mathrm{pl}}$ stands for the unrecoverable part described by $[\mathbf{F}^{\mathrm{el}}]^{-1} \cdot \mathbf{F}$. A decomposition of the strain increment (and thus of the strain rate) into the elastic contribution, $\boldsymbol{\varepsilon}^{\mathrm{e}}$, and plastic contribution, $\boldsymbol{\varepsilon}^{\mathrm{pl}}$, in the form

$$\Delta\boldsymbol{\varepsilon} = \Delta\boldsymbol{\varepsilon}^{\mathrm{e}} + \Delta\boldsymbol{\varepsilon}^{\mathrm{pl}} \tag{3.9}$$

is assumed, which is a consistent approximation to eqn. (3.7) if the elastic strains are negligible compared to unity and are small compared to the plastic strains.

In order to find the solution for the stress tensor at the end of the increment, an elastic predictor step is applied at the beginning of the increment and provides the trial stress tensor

$$\sigma_{ij}^{\mathrm{tr}} = C_{ijkl}^{\mathrm{e}}(\varepsilon_{kl}^{\mathrm{e}} + \Delta\varepsilon_{kl}), \tag{3.10}$$

where $\varepsilon_{kl}^{\mathrm{e}}$ are the components of the elastic strain tensor, $\boldsymbol{\varepsilon}^{\mathrm{e}}$, and the elastic stiffness matrix is defined as

$$C_{ijkl}^{\mathrm{e}} = \left(K - \frac{2}{3}G\right)\delta_{ij}\delta_{kl} + 2G\delta_{ik}\delta_{jl}, \tag{3.11}$$

where G stands for the shear modulus and K for the bulk modulus, isotropic elastic material behavior being assumed. δ_{ij} is the Kronecker delta. It is worth noting, that in the following discussion the shear components of $\boldsymbol{\varepsilon}^{\mathrm{e}}$ are the shear strains, ε_{ij}, whereas ABAQUS uses the shear angles

$$\gamma_{ij} = \varepsilon_{ij} + \varepsilon_{ji} \qquad \text{for } i \neq j, \tag{3.12}$$

which must be accounted for in the actual implementation.

In case the yield condition is violated in the predictor step ($\Phi > 0$), a return mapping algorithm must be started in a corrector step to update the stress tensor in such a way that the yield condition is fulfilled ($\Phi = 0$). For elastic states ($\Phi < 0$) the trial stress tensor is valid and can be used to update the stress tensor at the end of the increment and $\mathbf{C}^{\mathrm{cons}} = \mathbf{C}^{\mathrm{e}}$. In other words, the following return mapping algorithm will lead to a solution where the strain tensor increment, $\Delta\boldsymbol{\varepsilon}$, is split into an elastic and a plastic tensor to fulfill the yield condition $\Phi = 0$.

Pressure dependent elastoplastic models are characterized by a yield function

$$\Phi = \Phi(\sigma_{\mathrm{m}}, \sigma_{\mathrm{eq}}, H_i) \qquad i = 1, \ldots, n \tag{3.13}$$

that depends on the first stress invariant, that is the mean stress

$$\sigma_{\mathrm{m}} = \frac{1}{3}\boldsymbol{\sigma} : \mathbf{I}, \tag{3.14}$$

on the second stress deviator invariant, the equivalent von Mises stress

$$\sigma_{\text{eq}} = \sqrt{\left(\frac{3}{2}\mathbf{S} : \mathbf{S}\right)}, \tag{3.15}$$

and on a set of scalar state variables H_i, $i = 1, \dots, n$. Here $\mathbf{I}$ stands for the second order identity tensor defined by $I_{ij} = \delta_{ij}$ and

$$\mathbf{S} = \boldsymbol{\sigma} - \sigma_{\text{m}}\mathbf{I} = 2G\boldsymbol{\varepsilon}_{\text{D}}^{\text{e}} \tag{3.16}$$

is the stress deviator, where the deviatoric part of the elastic strain tensor can be expressed as

$$\boldsymbol{\varepsilon}_{\text{D}}^{\text{e}} = \boldsymbol{\varepsilon}^{\text{e}} - \frac{1}{3}\boldsymbol{\varepsilon}_{\text{V}}^{\text{e}} = \boldsymbol{\varepsilon}^{\text{e}} - \frac{1}{3}\varepsilon_{ii}^{\text{e}}\mathbf{I}, \tag{3.17}$$

$\varepsilon_{\text{V}}^{\text{e}}$ being known as the volumetric part of the elastic strain tensor $\boldsymbol{\varepsilon}^{\text{e}}$.

A proof of eqn. (3.16) is given in appendix B.

The increment of the plastic strain tensor $\boldsymbol{\varepsilon}^{\text{pl}}$ can be calculated from the flow rule as

$$\Delta\boldsymbol{\varepsilon}^{\text{pl}} = \Delta\Lambda\frac{\partial g}{\partial\boldsymbol{\sigma}} = \Delta\Lambda\left(\frac{\partial g}{\partial\sigma_{\text{m}}}\frac{\partial\sigma_{\text{m}}}{\partial\boldsymbol{\sigma}} + \frac{\partial g}{\partial\sigma_{\text{eq}}}\frac{\partial\sigma_{\text{eq}}}{\partial\boldsymbol{\sigma}}\right), \tag{3.18}$$

where $g = g(\sigma_{\text{m}}, \sigma_{\text{eq}}, H_i)$ is the flow potential and $\Delta\Lambda$ is a positive scalar. $\Delta\boldsymbol{\varepsilon}^{\text{pl}}$ can be split into two parts, the increment of the volumetric plastic strain tensor, $\Delta\boldsymbol{\varepsilon}_{\text{V}}^{\text{pl}} = \Delta\varepsilon_{ii}^{\text{pl}}\mathbf{I}$, and the increment of the deviatoric plastic strain tensor, $\Delta\boldsymbol{\varepsilon}_{\text{D}}^{\text{pl}}$, to give

$$\Delta\boldsymbol{\varepsilon}^{\text{pl}} = \frac{1}{3}\Delta\boldsymbol{\varepsilon}_{\text{V}}^{\text{pl}} + \Delta\boldsymbol{\varepsilon}_{\text{D}}^{\text{pl}}. \tag{3.19}$$

The evaluation of the terms in eqn. (3.18)

$$\frac{\partial\sigma_{\text{m}}}{\partial\boldsymbol{\sigma}} = \frac{\partial}{\partial\boldsymbol{\sigma}}\left(\frac{1}{3}\boldsymbol{\sigma} : \mathbf{I}\right) = \frac{1}{3}\mathbf{I} \tag{3.20}$$

and

$$\begin{aligned}
\frac{\partial\sigma_{\text{eq}}}{\partial\boldsymbol{\sigma}} &= \frac{\partial}{\partial\boldsymbol{\sigma}}\left(\frac{3}{2}\mathbf{S} : \mathbf{S}\right)^{\frac{1}{2}} = \frac{\partial}{\partial\boldsymbol{\sigma}}\left(\frac{3}{2}(\boldsymbol{\sigma} - \sigma_{\text{m}}\mathbf{I}) : (\boldsymbol{\sigma} - \sigma_{\text{m}}\mathbf{I})\right)^{\frac{1}{2}} \\
&= \frac{1}{2}\left(\frac{3}{2}(\boldsymbol{\sigma} - \sigma_{\text{m}}\mathbf{I}) : (\boldsymbol{\sigma} - \sigma_{\text{m}}\mathbf{I})\right)^{-\frac{1}{2}}2\frac{3}{2}(\boldsymbol{\sigma} - \sigma_{\text{m}}\mathbf{I}) = \frac{3}{2\sigma_{\text{eq}}}\mathbf{S}
\end{aligned} \tag{3.21}$$

and the introduction of the tensor

$$\mathbf{n} = \frac{3}{2\sigma_{\text{eq}}}\mathbf{S}, \tag{3.22}$$

leads to a new description of the increment of the plastic strain tensor

$$
\Delta\varepsilon^{\mathrm{pl}} = \Delta\Lambda \left(\frac{1}{3}\frac{\partial g}{\partial\sigma_{\mathrm{m}}}\mathbf{I} + \frac{\partial g}{\partial\sigma_{\mathrm{eq}}}\mathbf{n} \right) \tag{3.23}
$$

$$
= \frac{1}{3}\Delta\varepsilon_{\mathrm{p}}\mathbf{I} + \Delta\varepsilon_{\mathrm{q}}\mathbf{n},
$$

in terms of the increment of the first invariant of the plastic strain tensor

$$
\Delta\varepsilon_{\mathrm{p}} = \Delta\Lambda\frac{\partial g}{\partial\sigma_{\mathrm{m}}} = \Delta\varepsilon_{ii}^{\mathrm{pl}} = \Delta\varepsilon_{V}^{\mathrm{pl}} \tag{3.24}
$$

and the increment of a scalar

$$
\Delta\varepsilon_{\mathrm{q}} = \Delta\Lambda\frac{\partial g}{\partial\sigma_{\mathrm{eq}}}, \tag{3.25}
$$

that is related to the deviatoric part of the plastic strain tensor by

$$
\Delta\varepsilon_{\mathrm{D}}^{\mathrm{pl}} = \Delta\varepsilon_{\mathrm{q}}\mathbf{n}. \tag{3.26}
$$

The elimination of the unknown $\Delta\Lambda$ can be carried out by using the relationship

$$
\frac{\partial^2 f(x,y)}{\partial x \partial y} - \frac{\partial^2 f(x,y)}{\partial y \partial x} = 0, \tag{3.27}
$$

which, when applied to $\Delta\Lambda g$, leads to the relationship

$$
\Delta\Lambda\frac{\partial^2 g}{\partial\sigma_{\mathrm{eq}}\partial\sigma_{\mathrm{m}}} - \Delta\Lambda\frac{\partial^2 g}{\partial\sigma_{\mathrm{m}}\partial\sigma_{\mathrm{eq}}} = \Delta\varepsilon_{\mathrm{q}}\frac{\partial g}{\partial\sigma_{\mathrm{m}}} - \Delta\varepsilon_{\mathrm{p}}\frac{\partial g}{\partial\sigma_{\mathrm{eq}}} = 0, \tag{3.28}
$$

that links $\Delta\varepsilon_{\mathrm{p}}$ and $\Delta\varepsilon_{\mathrm{q}}$.

Splitting the stress tensor into volumetric, σ_{m}, and deviatoric, $\mathbf{S}$, contributions in analogy to eqn. (3.19) gives

$$
\sigma = \sigma_{\mathrm{m}} + \mathbf{S} = \sigma_{\mathrm{m}}\mathbf{I} + \frac{2}{3}\sigma_{\mathrm{eq}}\mathbf{n}. \tag{3.29}
$$

The stress tensor can be expressed in terms of the trial stress, σ^{tr}, as

$$
\sigma = \mathbf{C}^{\mathrm{e}} : \varepsilon^{\mathrm{e}} = \mathbf{C}^{\mathrm{e}} : \left(\varepsilon^{\mathrm{tr}} - \Delta\varepsilon^{\mathrm{pl}} \right) = \sigma^{\mathrm{tr}} - \mathbf{C}^{\mathrm{e}} : \Delta\varepsilon^{\mathrm{pl}}, \tag{3.30}
$$

compare the schematic sketch in fig. 3.1, and the new term on the right hand side of eqn. (3.30) can be evaluated by means of eqn. (3.23) as

$$
\mathbf{C}^{\mathrm{e}} : \Delta\varepsilon^{\mathrm{pl}} = \mathbf{C}^{\mathrm{e}} : \left(\frac{1}{3}\Delta\varepsilon_{\mathrm{p}}\mathbf{I} + \Delta\varepsilon_{\mathrm{q}}\mathbf{n} \right) \tag{3.31}
$$

with

$$\mathbf{C}^{\mathrm{e}} : \mathbf{I} = C^{\mathrm{e}}_{ijkl} I_{kl} = \left(K - \frac{2}{3}G \right) \delta_{ij}\delta_{kl}I_{kl} + 2G\delta_{ik}\delta_{jl}I_{kl} = 3K\mathbf{I} \tag{3.32}$$

and

$$\mathbf{C}^{\mathrm{e}} : \mathbf{n} = \frac{3}{2\sigma_{\mathrm{eq}}}\mathbf{C}^{\mathrm{e}} : \mathbf{S} = 2G\frac{3}{2\sigma_{\mathrm{eq}}}\mathbf{C}^{\mathrm{e}} : \varepsilon^{\mathrm{e}}_{\mathrm{D}} = 2G\frac{3}{2\sigma_{\mathrm{eq}}}\mathbf{S} = 2G\mathbf{n}. \tag{3.33}$$

Accordingly, the stress tensor is given by the expression

$$\boldsymbol{\sigma} = \boldsymbol{\sigma}^{\mathrm{tr}} - K\Delta\varepsilon_{\mathrm{p}}\mathbf{I} - 2G\Delta\varepsilon_{\mathrm{q}}\mathbf{n}, \tag{3.34}$$

which shows that in the deviatoric stress space the return to the yield surface is along $\mathbf{n}$. This implies that $\mathbf{S}^{\mathrm{tr}}$ and $\mathbf{S}$ are co-axial and, therefore, $\mathbf{n}$ can be simply calculated from the elastic predictor $\boldsymbol{\sigma}^{\mathrm{tr}}$ as

$$\mathbf{n} = \frac{3}{2\sigma_{\mathrm{eq}}}\mathbf{S} = \frac{3}{2\sigma^{\mathrm{tr}}_{\mathrm{eq}}}\mathbf{S}^{\mathrm{tr}}. \tag{3.35}$$

A comparison between expressions for the stress tensor in eqn. (3.29) and eqn. (3.34) gives

$$\begin{aligned}
\boldsymbol{\sigma} &= \sigma_{\mathrm{m}}\mathbf{I} + \frac{2}{3}\sigma_{\mathrm{eq}}\mathbf{n} \tag{3.36} \\
&= \boldsymbol{\sigma}^{\mathrm{tr}} - K\Delta\varepsilon_{\mathrm{p}}\mathbf{I} - 2G\Delta\varepsilon_{\mathrm{q}}\mathbf{n} \tag{3.37} \\
&= \sigma^{\mathrm{tr}}_{\mathrm{m}}\mathbf{I} + \frac{2}{3}\sigma^{\mathrm{tr}}_{\mathrm{eq}}\mathbf{n} - K\Delta\varepsilon_{\mathrm{p}}\mathbf{I} - 2G\Delta\varepsilon_{\mathrm{q}}\mathbf{n}
\end{aligned}$$

which provides the equations for calculating the new mean stress

$$\sigma_{\mathrm{m}} = \sigma^{\mathrm{tr}}_{\mathrm{m}} - K\Delta\varepsilon_{\mathrm{p}} \tag{3.38}$$

and the new equivalent stress

$$\sigma_{\mathrm{eq}} = \sigma^{\mathrm{tr}}_{\mathrm{eq}} - 3G\Delta\varepsilon_{\mathrm{q}} \tag{3.39}$$

in the corrector step of the return mapping algorithm. The full system of equations required in the corrector step is given in tab. 3.1 and can be solved by standard Newton iteration. An application of the above algorithm to the Gurson-based damage model was presented by Zhang [94] and pressure-dependent plasticity models including kinematic hardening are discussed by Mühlich and Brocks [95].

The return mapping algorithm for pressure-independent elastoplastic models, e.g. in the case of "standard" J_2-plasticity, that are characterized by $\frac{\partial \Phi}{\partial \sigma_{\mathrm{m}}} = \frac{\partial g}{\partial \sigma_{\mathrm{m}}} = 0$ and a vanishing

first invariant of the plastic strain tensor, $\varepsilon_{ii}^{pl} = 0$, can be treated with the above algorithm as well, by introducing the corresponding conditions. Return mapping procedures for pure pressure-independent elastoplastic constitutive relations are given e.g. by Ortiz et al. [96].

input: σ_m^{tr}, σ_{eq}^{tr}, $\mathbf{n} = \frac{3}{2\sigma_{eq}^{tr}}\mathbf{S}^{tr}$
$\Phi(\sigma_{eq}, \sigma_m, H_i) = 0 \qquad i = 1, \ldots, n$
$\Delta\varepsilon_q\frac{\partial g}{\partial\sigma_m} - \Delta\varepsilon_p\frac{\partial g}{\partial\sigma_{eq}} = 0$
$\sigma_m = \sigma_m^{tr} - K\Delta\varepsilon_p$
$\sigma_{eq} = \sigma_{eq}^{tr} - 3G\Delta\varepsilon_q$
$\Delta H_i = \Delta H_i(\Delta\varepsilon_p, \Delta\varepsilon_q, \sigma_m, \sigma_{eq}, H_j) \qquad i, j = 1,\ldots,n$
unknowns: σ_m, σ_{eq}, $\Delta\varepsilon_p$, $\Delta\varepsilon_q$, H_i (state variables)
output: $\boldsymbol{\sigma} = \sigma_m\mathbf{I} + \frac{2}{3}\sigma_{eq}\mathbf{n}$

Table 3.1: The full set of equations required for the corrector step in a pressure-dependent plasticity model

$$-\boldsymbol{C}^e : \Delta\boldsymbol{\varepsilon}^{pl} = -\Delta\Lambda\boldsymbol{C}^e : \left(\frac{\partial g}{\partial\boldsymbol{\sigma}}\right)$$
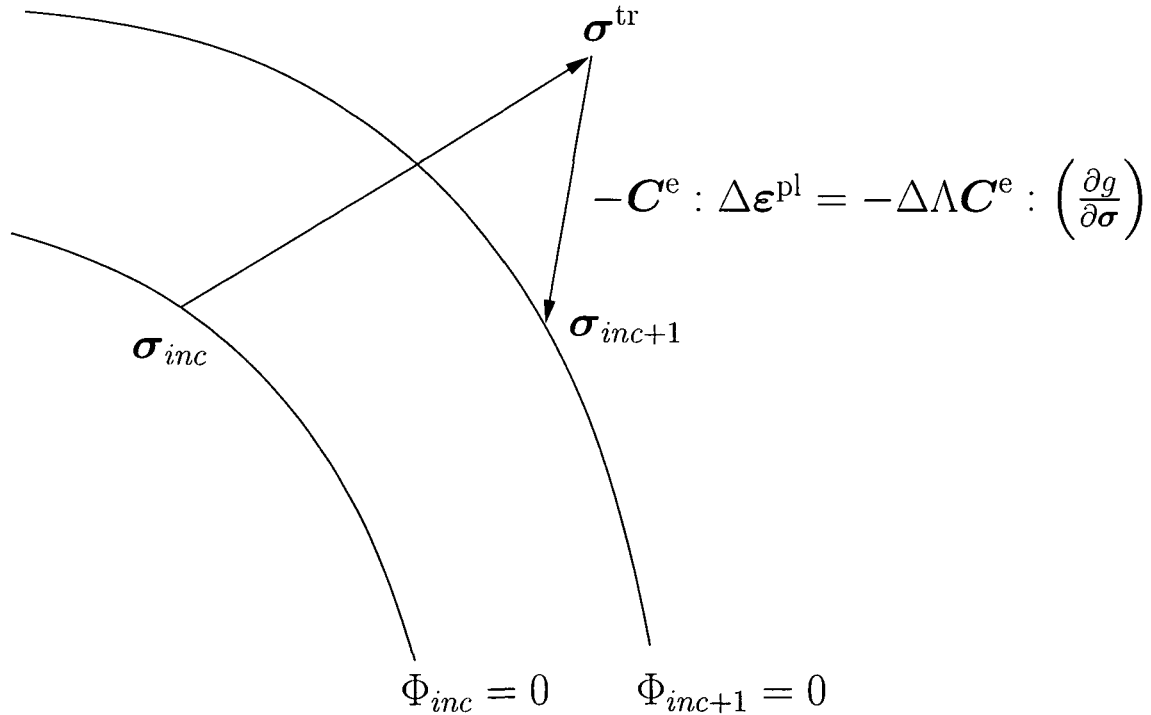
Figure 3.1: Geometric interpretation of the return mapping algorithm in stress space with stress states in two increments

3.2 Constitutive Equations of the Implemented Damage Models

In the following the constitutive equations for the implemented ductile damage models are given in a notation that can be used directly for the implementation into ABAQUS/Standard. Associated plasticity, where the yield function Φ and the flow potential g are identical, is assumed unless explicitly stated otherwise.

The DDIT model based on the damage indicator of Gunawardena et al., see subsection 2.3.1, follows standard J_2-plasticity throughout the "sub-critical" state, i.e. the ductile damage indicator

$$D = \sum_{inc=1}^{n} \frac{1}{1.65\varepsilon_0} \frac{\exp\left(\frac{3}{2}\frac{\sigma_m}{\sigma_{eq}}\right)_{inc} + \exp\left(\frac{3}{2}\frac{\sigma_m}{\sigma_{eq}}\right)_{inc-1}}{2} \Delta\varepsilon^{pl}_{eq,inc}, \qquad (3.40)$$

is evaluated after each increment, inc, using a trapeze rule, but does not influence the material behavior until the critical value is reached. Once D reaches the critical value, D_{crit}, the material point is treated as having failed, the stress is set to a very small number, and a linear elastic material behavior with an extremely small Young's modulus (10^{-8} times that of the damage-free material) is activated. This material model was implemented both into a user defined material routine (UMAT) and into a user defined field routine (USDFLD). All equations necessary for implementing this model into a UMAT are collected in tab. 3.2, and only eqn. (3.40) is required to trigger the reduction of stiffness in a given integration point in the USDFLD.

A discussion of the responses obtained with the UMAT and the USDFLD subroutines is given in section 3.6.

It is worth noting that the DDIT model will not indicate failure in loading scenarios in which the local stress state is hydrostatic and does not give rise to yielding with the J_2 theory used. Accordingly, the overall response remains linear elastic and no growth of the damage indicator is obtained from eqn. (3.40) since the increment of the plastic strain, $\Delta\varepsilon^{pl}_{eq,inc}$, remains zero.

The full set of equations making up the GTN model discussed in subsection 2.3.2 is listed in tab. 3.3. It consists of 8 explicit and 2 implicit equations for 10 unknowns. This nonlinear system must be solved for each integration point in each iteration. The modified void

volume fraction

$$
f^* = \begin{cases} f & \text{for} \quad 0 \le f < f_c \\ f_c + \frac{0.8 q_1^{-1} - f_c}{f_f - f_c}(f - f_c) & \text{for} \quad f_c \le f < f_f \\ \frac{0.8}{q_1} + \frac{0.2 q_1^{-1}}{1.0 - f_f}(f - f_f) & \text{for} \quad f_f \le f \le 1 \end{cases} \tag{3.41}
$$

is defined in three stages depending on f, where f_f is the void volume fraction at failure. The third of these stages was introduced by the author to avoid numerical difficulties. Beyond $f = 1$, where complete loss of stiffness takes place, the integration point can be treated in analogy to the failed state in the DDIT model. The relation between f and f^* is depicted in fig. 3.2. Note that the relations in tab. 3.3 also include an evolution equation for the void volume fraction, f, which follows the original paper of Gurson [37].

An alternative strategy for handling damaged integration points was suggested by Zhang [97]. In this "fixed Gurson-based model" the load-carrying capacity for $f > f_f$ is controlled by a GTN-based non-hardening material behavior that no longer evolves. Accordingly, the yield surface is kept constant and the corrector step in the return mapping algorithm has to return the stress to the same yield surface after each elastic predictor step. The author found that this approach can give rise to an unfavorable convergence behavior due to ill-posed Jacobians.

The second damage progress model that was implemented into ABAQUS/Standard is the Rousselier model presented in subsection 2.3.2. The evolution of the void volume fraction in this model can be calculated in the same way as for the modified Gurson model, compare tab. 3.3, and an additional variable B may be introduced for handling void coalescence in loose analogy to the GTN model with

$$
\Delta f = (1 - f) B \Delta \varepsilon_p, \tag{3.42}
$$

$$
B = \begin{cases} 1 & \text{for } 0 \le f < f_c \\ 1 + \frac{4}{f_F - f_c}(f - f_c) & \text{for } f_c \le f < f_F \\ 0.5 & \text{for } f_F \le f \le 1 \end{cases} \tag{3.43}
$$

see also fig. 3.3. With this extension the void volume fraction in the Rousselier model increases rapidly for $f \ge f_c$ but reverts to a very slow rate of growth once f_F is reached. This behavior is similar to the one enforced by eqn. (3.41) for f^* in the GTN model.

The initial void volume fraction, f_0, required by the Rousselier and GTN models can be obtained by summing over the volume fractions of the preexisting voids and of any inclusions that can be assumed to be weakly bonded to the matrix.

A total of 2 implicit and 6 explicit equations are available for the 8 unknowns of the standard Rousselier model, see tab. 3.4. One can see, that the variable $\Delta \varepsilon_q$ explained

in eqn. (3.25) is treated as the increment of the equivalent plastic strain, $\Delta\varepsilon_{eq}^{pl}$, in the Rousselier model, whilst in the Gurson model $\Delta\varepsilon_q$ is an additional unknown that can be evaluated from the equivalence of the overall rate of plastic work

$$\boldsymbol{\sigma} : \Delta\boldsymbol{\varepsilon}^{pl} = \sigma_m \Delta\varepsilon_p + \sigma_{eq}\Delta\varepsilon_q = (1 - f)\sigma_f \Delta\varepsilon_{eq}^{pl}. \tag{3.44}$$

The difference between the GTN and Rousselier models in the behavior at final failure is worth noting. The GTN model is designed such that the yield surface shrinks to the origin of the stress space ($\sigma_m = 0$, $\sigma_{eq} = 0$) when f^* reaches $1/q_1$, provided that the material parameter q_3 is equal to q_1^2. Otherwise, due to the quadratic form of the yield function,

$$\Phi = \frac{0^2}{\sigma_f^2} + 2q_1 f^* \cosh\left(\frac{0}{2\sigma_f}\right) - 1 - q_3 f^{*2} = 2q_1 f^* - 1 - q_3 f^{*2} = 0, \tag{3.45}$$

two solutions are obtained for the void volume at failure

$$f_f^* = \pm\sqrt{\left(\frac{q_1}{q_3}\right)^2 - \frac{1}{q_3}} + \frac{q_1}{q_3}. \tag{3.46}$$

This explains why the assumption of $q_3 = q_1^2$ can be found very often in the literature. The Rousselier model, in contrast, shows no comparable restrictions, the state of complete failure being determined by both void volume fraction and yield stress (or equivalent plastic strain) so that it cannot be calibrated in advance. To account for this aspect of the Rousselier model a modification proposed by Aboutayeb [98] was used in the present work, where a replacement of the material parameter σ_1 by the expression $q_4\sigma_f$ was suggested, q_4 being a new material parameter. The equations corresponding to this modified Rousselier model are listed in tab. 3.5. These modifications lead to a unique void volume fraction at failure, f_F, depending on the material parameter q_4 and on $\tilde{D}$.

In the DDIT model, of course, ductile failure is unequivocally described by $D = 1$. Table 3.6 gives the conditions for total failure for all three models and for the modified Rousselier model.

A direct comparison between the above ductile damage models can be obtained by rearranging the yield condition $\Phi = 0$ such that the equivalent stress, σ_{eq}, is expressed as a function of the mean stress, σ_m. Figure 3.4 shows the σ_{eq}-σ_m-diagram for the DDIT, GTN and Rousselier models. First, it can be seen that the DDIT model does not depend on the mean stress because it follows J_2-plasticity theory if $D < D_{crit}$. Second, whilst the GTN model shows an infinite slope at $\sigma_{eq} = 0$, a vertex can be observed for the Rousselier model in that point. Furthermore, a completely different behavior is evident for yielding under compressive hydrostatic loads.

The vertex of the Rousselier model plays an important role when tensile hydrostatic stress states occur. The use of the relation

$$\sigma_{eq} = \sigma_{eq}^{tr} - 3G\Delta\varepsilon_q \tag{3.47}$$

in the return mapping algorithm in eqn. (3.39) as listed in tab. 3.2, 3.3, 3.4 can then lead to negative values of the equivalent stress, which, of course, is not acceptable. Interestingly, if negative results from eqn. (3.47) are nevertheless plugged into eqn. (3.15), the obtained stress tensor has a (positive) equivalent stress of the same magnitude, but does not satisfy the governing set of equations. From the above discussion it is evident that appropriate measures must be taken to make the Rousselier model a robust and practical proposition for analyses where hydrostatic or nearly hydrostatic stress states can occur, as is often the case in micromechanical models. To the authors knowledge a solution for this problem has not been given in the literature. Figure 3.5 shows a number of modifications to the Rousselier flow surface that were tested by the author for removing the vertex of the yield surface on the hydrostatic axis. All these modifications aim at removing the vertex while modifying the Rousselier flow surface as little as possible. The extension #1 of the Rousselier model depicted in fig. 3.5 introduces a segment of a circle in the σ_{eq}-σ_m plane

$$\sigma_{eq} = \sqrt{r^2 - (\sigma_m - u)^2}, \tag{3.48}$$

where r and u stand for the radius and the offset of the center of the circle along the σ_m-axis, respectively. A smooth transition between the Rousselier flow function and the circle was provided at a stress triaxiality of $\eta = 4$. Two equations for r and u can be obtained by enforcing the intersection at $\eta = 4$

$$\sigma_{eq}^{int} = \sigma_f - \tilde{D}f\sigma_1 \exp\left(\frac{\sigma_m^{int}}{\sigma_1}\right) = \sqrt{r^2 - (\sigma_m^{int} - u)^2} \tag{3.49}$$

and by requiring it to be smooth

$$\frac{\partial\sigma_{eq}^{int}}{\partial\sigma_m^{int}} = \frac{\partial\sigma_f - \tilde{D}f\sigma_1 \exp\left(\frac{\sigma_m^{int}}{\sigma_1}\right)}{\partial\sigma_m^{int}} = \frac{\partial\sqrt{r^2 - (\sigma_m^{int} - u)^2}}{\partial\sigma_m^{int}}. \tag{3.50}$$

The point of transition

$$\sigma_{eq}^{int} = \frac{\sigma_m^{int}}{4} = \sigma_f - Df\sigma_1 \exp\left(\frac{\sigma_m^{int}}{\sigma_1}\right) \tag{3.51}$$

can only be found iteratively. The above approach seems to be the best method from the point of view of "removing" the vertex, of guaranteeing an infinite slope at $\sigma_{eq} = 0$

and of causing no problems in the return mapping algorithm. In practice, however, the introduction of the four additional, nonlinear equations for the four new unknowns r, u, σ_m^{int} and σ_{eq}^{int} increases the complexity of the whole set of equations dramatically and convergence for nearly hydrostatic loads was obtained only in cases where the predictor step in the return mapping procedure was very small. If the predictor step provides a stress state in the vicinity of $\eta = 4$, switching between the Rousselier flow surface and the circle may occur during iteration, which can cause additional numerical difficulties.

The next two ways of removing the vertex are based on the idea of using a continuous function in the whole domain so that the introduction of an intersection point is not necessary. Extensions #2 and #3 use smooth penalty functions that are activated in the vicinity of $\sigma_{eq} = 0$ only. The yield functions obtained this way are

$$\Phi = \sigma_{eq} - \sigma_f + \left(\tilde{D} + \tilde{D}m_1 \left(\frac{\arctan \left(\exp \left(m_2 \frac{\sigma_m}{\sigma_m^*} - 1 \right) \right)}{1.57} \right) \right) \sigma_1 f \exp \left(\frac{\sigma_m}{\sigma_1} \right) \quad (3.52)$$

for algorithm #2 and

$$\Phi = \sigma_{eq} - \sigma_f + \left(\tilde{D} + \tilde{D}m_3 \left(\frac{1}{1 + \left(\frac{\sigma_m^* - \sigma_m}{\sigma_m/m_4} \right)^{m_5}} \right)^{m_5} \right) \sigma_1 f \exp \left(\frac{\sigma_m}{\sigma_1} \right) \quad (3.53)$$

for algorithm #3, respectively. Both reduce σ_{eq} considerably in the neighborhood of the hydrostatic case, where

$$\sigma_m^*(\sigma_{eq} = 0) = \sigma_1 \ln \left(\frac{\sigma_f}{\tilde{D} f \sigma_1} \right). \quad (3.54)$$

The chosen parameters m_i are given in tab. 3.7. These two approaches definitely provide smooth yield functions but give rise to similar numerical difficulties as observed with extension #1.

Modification #4 replaces the Rousselier yield function with an elliptic function as used in the GTN approach. The Rousselier model is used to obtain the mean stress, σ_m^*, and the equivalent stress,

$$\sigma_{eq}^*(\sigma_m = 0) = \sigma_f - \tilde{D} f \sigma_1, \quad (3.55)$$

which are used to define an elliptic yield function

$$\Phi = \frac{\sigma_{eq}^2}{\sigma_{eq}^{*2}} + \frac{\sigma_m^2}{\sigma_m^{*2}} - 1. \quad (3.56)$$

This algorithm works very well and stably, but cannot be considered to be a Rousselier model in the strict sense.

A workable compromise was found in extension #5, where the Rousselier flow function, Φ, listed in tab. 3.4 is combined with an elliptic flow potential, g, that follows eqn. (3.56), i.e. a non-associated flow rule is used. This preserves the main features of the original Rousselier model (the yield function, Φ, will be unaffected) and avoids the unrealistic calculation of σ_{eq}.

The full set of equations for the extended (extension #5) and modified (following Abou-tayeb [98]) Rousselier model that was applied for part of the simulations in this work is given in tab. 3.5.

The sets of nonlinear equations given in tab. 3.2, 3.3, 3.4, 3.5 can be solved by Newton-methods. The considerable number of equations and their nonlinearity, however, give rise to numerical difficulties. The marked differences in the absolute values of the coefficients in the above sets of equations (compare e.g. the orders of magnitude of the increment of the equivalent plastic strain, $\Delta\varepsilon_{eq}^{pl}$, and of the flow stress, σ_f) lead to ill posed problems in inverting the corresponding system matrices. For that reason, the introduction of normalizing factors into the involved equations is necessary for obtaining a suitably conditioned systems of equations. A further problem was detected in the criterion for finding the "correct" solution and hence stopping the Newton algorithm. The criterion

$$\left| \frac{\Delta x_i}{x_i} \right| < \texttt{TOLER}, \tag{3.57}$$

where x_i stands for the unknown i and $\texttt{TOLER}$ for a tolerance of the order of 10^{-5}, was not sufficient for ensuring convergence. Accordingly, an additional criterion was introduced in such cases. If the equation is of the form

$$f = \sum_{i=1}^{N} a_i(x_k) = 0, \tag{3.58}$$

where $a_i(x_k)$ are the terms of the sum containing the unknowns, the decision when the function f is sufficiently close to zero is difficult, because it depends on the order of magnitude of each summand. A criterion, where the absolute value of the residuum is required to be below an appropriate bound,

$$f = \left| \sum_{i=1}^{N} a_i(x_k) \right| \leq 10^{-3} \left(\frac{\sum_{i=1}^{N} |a_i(x_k)|}{N} \right), \tag{3.59}$$

was found – in combination with eqn. (3.57) – to provide a robust indication of convergence. It was accordingly applied in this work to solve the above equations for each integration point.

$\Phi = g = \sigma_{eq} - \sigma_f = 0$
$\varepsilon_{eq}^{pl} = \varepsilon_{eq}^{pl,tr} + \Delta\varepsilon_{eq}^{pl}$
$\sigma_{eq} = \sigma_{eq}^{tr} - 3G\Delta\varepsilon_{eq}^{pl}$
$\sigma_f = \sigma_f(\varepsilon_{eq}^{pl})$
$D = D(\sigma_m/\sigma_{eq}, \Delta\varepsilon_{eq}^{pl})$ is defined in eqn. (3.40)
unknowns: $\sigma_{eq}, \sigma_f, \varepsilon_{eq}^{pl}, \Delta\varepsilon_{eq}^{pl}, D$

Table 3.2: The full set of equations for the DDIT model based on Gunawardena's damage indicator

$\Phi = g = \frac{\sigma_{eq}^2}{\sigma_f^2} + 2q_1 f^* \cosh\left(\frac{3q_2\sigma_m}{2\sigma_f}\right) - 1 - q_3 f^{*2} = 0$
$\Delta\varepsilon_p \frac{\partial g}{\partial\sigma_{eq}} - \Delta\varepsilon_q \frac{\partial g}{\partial\sigma_m} = 0$
$\Delta\varepsilon_{eq}^{pl} = \frac{\sigma_m\Delta\varepsilon_p + \sigma_{eq}\Delta\varepsilon_q}{(1-f)\sigma_f}$
$\Delta f = (1 - f)\Delta\varepsilon_p$
$f = f^{tr} + \Delta f$
$\varepsilon_{eq}^{pl} = \varepsilon_{eq}^{pl,tr} + \Delta\varepsilon_{eq}^{pl}$
$\sigma_m = \sigma_m^{tr} - K\Delta\varepsilon_p$
$\sigma_{eq} = \sigma_{eq}^{tr} - 3G\Delta\varepsilon_q$
f^* is defined in eqn. (3.41)
$\sigma_f = \sigma_f(\varepsilon_{eq}^{pl})$
unknowns: $\sigma_m, \sigma_{eq}, \sigma_f, f, \Delta f, f^*, \varepsilon_{eq}^{pl}, \Delta\varepsilon_{eq}^{pl}, \Delta\varepsilon_q, \Delta\varepsilon_p$

Table 3.3: The full set of equations for the GTN model

$$\Phi = g = \sigma_{eq} - \sigma_f + \sigma_1 f \tilde{D} \exp\left(\frac{\sigma_m}{\sigma_1}\right) = 0$$

$$\Delta\varepsilon_p \frac{\partial g}{\partial \sigma_{eq}} - \Delta\varepsilon_q \frac{\partial g}{\partial \sigma_m} = 0$$

Δf is defined in eqn. (3.42)

$$f = f^{tr} + \Delta f$$

$$\varepsilon_{eq}^{pl} = \varepsilon_{eq}^{pl,tr} + \Delta\varepsilon_q$$

$$\sigma_m = \sigma_m^{tr} - K\Delta\varepsilon_p$$

$$\sigma_{eq} = \sigma_{eq}^{tr} - 3G\Delta\varepsilon_q$$

$$\sigma_f = \sigma_f(\varepsilon_{eq}^{pl})$$

unknowns: $\sigma_m, \sigma_{eq}, \sigma_f, f, \Delta f, \varepsilon_{eq}^{pl}, \Delta\varepsilon_q, \Delta\varepsilon_p$

Table 3.4: The full set of equations for the Rousselier model

$$\Phi = \sigma_{eq} - \sigma_f + q_4\sigma_f f \tilde{D} \exp\left(\frac{\sigma_m}{q_4\sigma_f}\right) = 0$$

$$g = \frac{\sigma_{eq}^2}{\sigma_{eq}^{*2}} + \frac{\sigma_m^2}{\sigma_m^{*2}} - 1$$

$$\Delta\varepsilon_p \frac{\partial g}{\partial \sigma_{eq}} - \Delta\varepsilon_q \frac{\partial g}{\partial \sigma_m} = 0$$

$$\sigma_m^* = q_4\sigma_f \ln\left(\frac{1}{q_4\tilde{D}f}\right)$$

$$\sigma_{eq}^* = \sigma_f(1 - \tilde{D}fq_4)$$

Δf is defined in eqn. (3.42)

$$f = f^{tr} + \Delta f$$

$$\varepsilon_{eq}^{pl} = \varepsilon_{eq}^{pl,tr} + \Delta\varepsilon_q$$

$$\sigma_m = \sigma_m^{tr} - K\Delta\varepsilon_p$$

$$\sigma_{eq} = \sigma_{eq}^{tr} - 3G\Delta\varepsilon_q$$

$$\sigma_f = \sigma_f(\varepsilon_{eq}^{pl})$$

unknowns: $\sigma_m, \sigma_{eq}, \sigma_f, f, \Delta f, \varepsilon_{eq}^{pl}, \Delta\varepsilon_q, \Delta\varepsilon_p, g, \sigma_m^*, \sigma_{eq}^*$

Table 3.5: The full set of equations for the extended, modified [98] Rousselier model

Model	damage variable at failure for $\Phi(\sigma_m = 0, \sigma_{eq} = 0) = 0$
Rousselier	$f = \frac{\sigma_f}{\sigma_1 D}$
mod. Rousselier	$f = \frac{1}{q_4 D}$
GTN	$f^* = \frac{1}{q_1}$ with $q_3 = q_1^2$
DDIT	$D = D_{crit}$

Table 3.6: Conditions at final failure for the considered ductile damage models

m_1	100
m_2	100
m_3	100
m_4	20
m_5	8
m_6	2

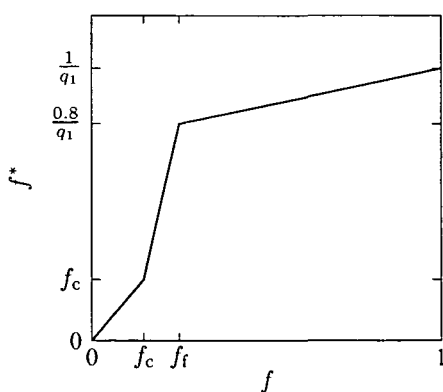Table 3.7: Parameters m_i for the extended Rousselier models #2 and #3

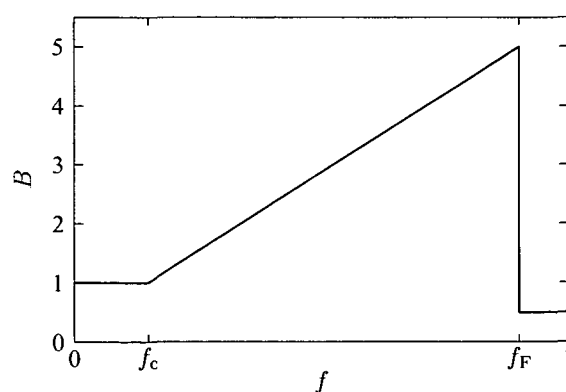Figure 3.2: Relation between f^* and f in the GTN model, eqn. (3.41)

Figure 3.3: Relation between B and f in the modified Rousselier model, eqn. (3.43)
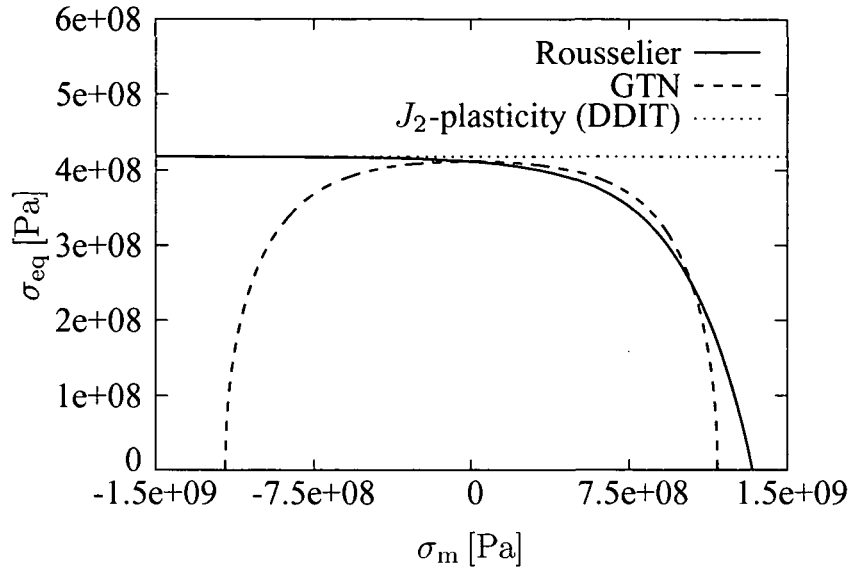
Figure 3.4: σ_{eq}-σ_m-diagram of the GTN, Rousselier and DDIT models at an arbitrary state described by $\varepsilon_{eq}^{pl} = 10^{-2}$ and $f = 10^{-2}$
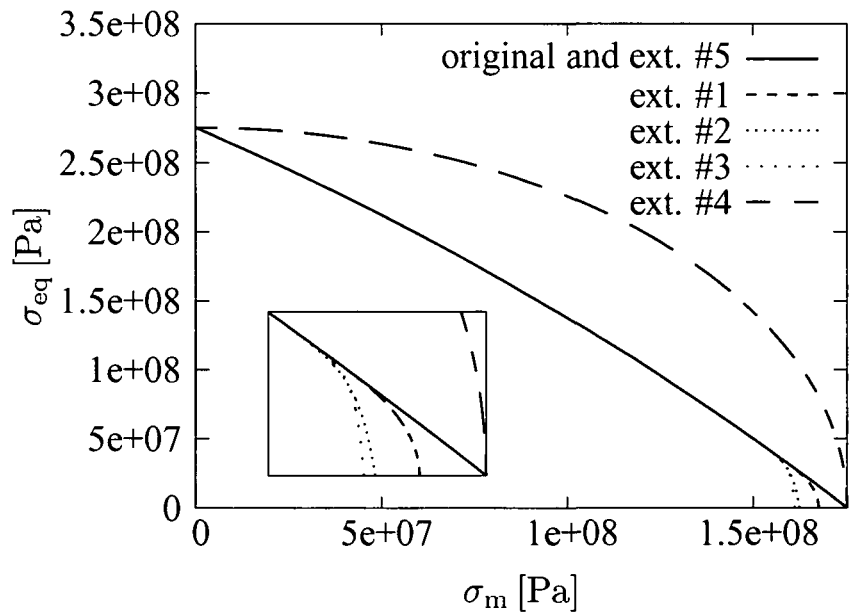

Figure 3.5: "Extended" Rousselier models that avoid the vertex in the flow surface at $\sigma_{eq} = 0$ ($\varepsilon_{eq}^{pl} = 0.36$ and $f = 0.58$ are set in this case and extension #5 differs from the original model in the definition of the flow potential, g, only)

3.3   Consistent Tangent (Jacobian)

In the ABAQUS/Standard UMAT a consistent tangent (DDSDDE array in the parameter list
of the UMAT routine)

$$\mathbf{C}^{\text{cons}} = \frac{\partial \Delta \boldsymbol{\sigma}}{\partial \Delta \boldsymbol{\varepsilon}} = \frac{\partial \boldsymbol{\sigma}}{\partial \boldsymbol{\varepsilon}} \tag{3.60}$$

must be determined by the user. The component C_{ijkl} of the Jacobian defines the change in
the ij stress component at the end of the increment caused by an infinitesimal perturbation
of the kl strain component. The ABAQUS manual states that an incorrect value of the
material Jacobian only affects the rate of convergence, but not the obtained results. For
calculations in the softening regime, however, the author found that the predictions for the
displacement, stress and strain fields can depend markedly on the choice of the Jacobian.
This can be shown by a single element test performed with the GTN model and a 20 node
element (27 ips=integration points), where a consistent and an incorrect (in this case, the
elastic) material Jacobian were used, see figs. 3.6 and 3.7, respectively. A unique solution
for all integration points in the simulation using the consistent tangent was found for all
integration points as can be seen from the figures, whilst different results were obtained for
different integration points when an incorrect tangent was applied. This example shows
the importance of a consistent derivation of the Jacobian from the governing constitutive
equations.

The procedure for determining a consistent tangent for pressure-dependent elastoplasticity
models proposed by Aravas [93] and improved by Zhang [97] is presented in the following.
Due to some errors in both publications the derivations were redone to obtain the correct
set of equations.

Note that the definitions of the tensor operators ":" and "$\otimes$" used in the following are
given at the beginning of chapter 3.

In order to calculate the consistent tangent, the total derivative of the stress tensor

$$
\begin{aligned}
\boldsymbol{\sigma} &= \mathbf{C}^{\text{e}} : \left(\boldsymbol{\varepsilon} - \boldsymbol{\varepsilon}^{\text{pl}} \right) \\
&= \mathbf{C}^{\text{e}} : \left(\boldsymbol{\varepsilon} - \boldsymbol{\varepsilon}_t^{\text{pl}} - \Delta \boldsymbol{\varepsilon}^{\text{pl}} \right) \\
&= \mathbf{C}^{\text{e}} : \left(\boldsymbol{\varepsilon} - \boldsymbol{\varepsilon}_t^{\text{pl}} - \frac{1}{3} \Delta \varepsilon_{\text{p}} \mathbf{I} - \Delta \varepsilon_{\text{q}} \mathbf{n} \right)
\end{aligned} \tag{3.61}
$$

must be calculated, where the index "t" indicates the beginning of the increment. This
total derivative takes the form

$$\partial \boldsymbol{\sigma} = \mathbf{C}^{\text{e}} : \left(\partial \boldsymbol{\varepsilon} - \frac{1}{3} \partial \Delta \varepsilon_{\text{p}} \mathbf{I} - \partial \Delta \varepsilon_{\text{q}} \mathbf{n} - \Delta \varepsilon_{\text{q}} \frac{\partial \mathbf{n}}{\partial \boldsymbol{\sigma}} : \partial \boldsymbol{\sigma} \right). \tag{3.62}$$

Note that ε_t^{pl} is a constant and, accordingly, does not contribute to the differential.
To calculate the two unknowns $\partial\Delta\varepsilon_p$ and $\partial\Delta\varepsilon_q$, the differentiation of eqn. (3.13) and
eqn. (3.28) must be performed to obtain

$$\partial\Phi = \left(\frac{\partial\Phi}{\partial\sigma_m}\frac{\partial\sigma_m}{\partial\boldsymbol{\sigma}} + \frac{\partial\Phi}{\partial\sigma_{eq}}\frac{\partial\sigma_{eq}}{\partial\boldsymbol{\sigma}}\right) : \partial\boldsymbol{\sigma} + \sum_{i=1}^{n}\frac{\partial\Phi}{\partial H_i}\partial H_i = 0 \tag{3.63}$$

and

$$\partial\left(\Delta\varepsilon_p\frac{\partial g}{\partial\sigma_{eq}} - \Delta\varepsilon_q\frac{\partial g}{\partial\sigma_m}\right) = \tag{3.64}$$

$$\partial\Delta\varepsilon_p\frac{\partial g}{\partial\sigma_{eq}} + \Delta\varepsilon_p\left(\left(\frac{\partial^2 g}{\partial\sigma_{eq}^2}\frac{\partial\sigma_{eq}}{\partial\boldsymbol{\sigma}} + \frac{\partial^2 g}{\partial\sigma_m\partial\sigma_{eq}}\frac{\partial\sigma_m}{\partial\boldsymbol{\sigma}}\right) : \partial\boldsymbol{\sigma} + \sum_{i=1}^{n}\frac{\partial^2 g}{\partial\sigma_{eq}\partial H_i}\partial H_i\right) -$$

$$\partial\Delta\varepsilon_q\frac{\partial g}{\partial\sigma_m} - \Delta\varepsilon_q\left(\left(\frac{\partial^2 g}{\partial\sigma_m^2}\frac{\partial\sigma_m}{\partial\boldsymbol{\sigma}} + \frac{\partial^2 g}{\partial\sigma_m\partial\sigma_{eq}}\frac{\partial\sigma_{eq}}{\partial\boldsymbol{\sigma}}\right) : \partial\boldsymbol{\sigma} + \sum_{i=1}^{n}\frac{\partial^2 g}{\partial\sigma_m\partial H_i}\partial H_i\right) = 0,$$

respectively, with

$$\partial H_i = \sum_{j=1}^{n}c_{ij}\left(\frac{\partial\Delta H_j}{\partial\Delta\varepsilon_p}\partial\Delta\varepsilon_p + \frac{\partial\Delta H_j}{\partial\Delta\varepsilon_q}\partial\Delta\varepsilon_q + \left(\frac{\partial\Delta H_j}{\partial\sigma_m}\frac{\partial\sigma_m}{\partial\boldsymbol{\sigma}} + \frac{\partial\Delta H_j}{\partial\sigma_{eq}}\frac{\partial\sigma_{eq}}{\partial\boldsymbol{\sigma}}\right) : \partial\boldsymbol{\sigma}\right). \tag{3.65}$$

Here c_{ij} is the inverse of the tensor

$$\hat{c}_{ij} = \left(\delta_{ij} - \frac{\partial\Delta H_i}{\partial H_j}\right) \tag{3.66}$$

and is derived in appendix C for the case of $n = 2$ and $\Delta H_i = \Delta H_i(\sigma_m, \sigma_{eq}, \Delta\varepsilon_p, \Delta\varepsilon_q, H_j)$.
By reformulating eqn. (3.63) and eqn. (3.64) the expressions

$$A_{11}\partial\Delta\varepsilon_p + A_{12}\partial\Delta\varepsilon_q = (B_{11}\mathbf{I} + B_{12}\mathbf{n}) : \partial\boldsymbol{\sigma}, \tag{3.67}$$

$$A_{21}\partial\Delta\varepsilon_p + A_{22}\partial\Delta\varepsilon_q = (B_{21}\mathbf{I} + B_{22}\mathbf{n}) : \partial\boldsymbol{\sigma}, \tag{3.68}$$

are obtained, from which $\partial\Delta\varepsilon_p$ and $\partial\Delta\varepsilon_q$ can be solved by inverting $\mathbf{A}$ to $\bar{\mathbf{A}} = \mathbf{A}^{-1}$, which
leads to

$$\partial\Delta\varepsilon_p = \left((\bar{A}_{11}B_{11} + \bar{A}_{12}B_{21})\mathbf{I} + (\bar{A}_{11}B_{12} + \bar{A}_{12}B_{22})\mathbf{n}\right) : \partial\boldsymbol{\sigma}, \tag{3.69}$$

$$\partial\Delta\varepsilon_q = \left((\bar{A}_{21}B_{11} + \bar{A}_{22}B_{21})\mathbf{I} + (\bar{A}_{21}B_{12} + \bar{A}_{22}B_{22})\mathbf{n}\right) : \partial\boldsymbol{\sigma}. \tag{3.70}$$

In the notation of Aravas these relations can be expressed as

$$\partial\Delta\varepsilon_p = (m_{pI}\mathbf{I} + m_{pn}\mathbf{n}) : \partial\boldsymbol{\sigma}, \tag{3.71}$$

$$\partial\Delta\varepsilon_q = (m_{qI}\mathbf{I} + m_{qn}\mathbf{n}) : \partial\boldsymbol{\sigma}. \tag{3.72}$$

Inserting eqn. (3.71) and eqn. (3.72) into eqn. (3.62) and rearranging yields the relationship

$$(\mathbf{J} + \mathbf{C}^e : \mathbf{M}) : \partial\boldsymbol{\sigma} = \mathbf{C}^e : \partial\boldsymbol{\varepsilon} \tag{3.73}$$

where

$$\mathbf{M} = \frac{1}{3}m_{\text{pI}}\mathbf{I} \otimes \mathbf{I} + \frac{1}{3}m_{\text{pn}}\mathbf{I} \otimes \mathbf{n} + m_{\text{qI}}\mathbf{n} \otimes \mathbf{I} + m_{\text{qn}}\mathbf{n} \otimes \mathbf{n} + \Delta\varepsilon_q\frac{\partial\mathbf{n}}{\partial\boldsymbol{\sigma}} \tag{3.74}$$

and $\mathbf{J}$ is the fourth order identity tensor defined by $J_{jklm} = \delta_{jl}\delta_{km}$.
The inversion of $(\mathbf{J} + \mathbf{C}^e : \mathbf{M})$ leads to the consistent tangent

$$\mathbf{C}^{\text{cons}} = \frac{\partial\Delta\boldsymbol{\sigma}}{\partial\Delta\boldsymbol{\varepsilon}} = \frac{\partial\boldsymbol{\sigma}}{\partial\boldsymbol{\varepsilon}} = (\mathbf{J} + \mathbf{C}^e : \mathbf{M})^{-1}\,\mathbf{C}^e = \left(\mathbf{M} + \mathbf{C}^{e^{-1}}\right)^{-1}. \tag{3.75}$$

Zhang [97] proposed a method to avoid the above inversion by using the expression

$$\partial\boldsymbol{\sigma} = \mathbf{Z} : \partial\boldsymbol{\varepsilon} - K\mathbf{I}\partial\Delta\varepsilon_p - 2G\mathbf{n}\partial\Delta\varepsilon_q \tag{3.76}$$

with

$$\mathbf{Z} = 2G\frac{\sigma_{\text{eq}}}{\sigma_{\text{eq}}^{\text{tr}}}\mathbf{J} + \left(K - \frac{2G}{3}\frac{\sigma_{\text{eq}}}{\sigma_{\text{eq}}^{\text{tr}}}\right)\mathbf{I} \otimes \mathbf{I} + \frac{4G^2}{\sigma_{\text{eq}}^{\text{tr}}}\Delta\varepsilon_q\mathbf{n} \otimes \mathbf{n}. \tag{3.77}$$

where $\boldsymbol{\sigma}^{\text{tr}}$ is the trial stress tensor defined in eqn. (3.10).
By substituting eqn. (3.76) into eqn. (3.67) and eqn. (3.68), one obtains

$$\partial\Delta\varepsilon_p = (C_{11}\mathbf{I} + C_{12}\mathbf{n}) : \mathbf{Z} : \partial\boldsymbol{\varepsilon}, \tag{3.78}$$

$$\partial\Delta\varepsilon_q = (C_{21}\mathbf{I} + C_{22}\mathbf{n}) : \mathbf{Z} : \partial\boldsymbol{\varepsilon}, \tag{3.79}$$

so that only an inversion of a 2x2 matrix

$$\mathbf{C} = \begin{pmatrix} A_{11} + 3KB_{11} & A_{12} + 3GB_{12} \\ A_{21} + 3KB_{21} & A_{22} + 3GB_{22} \end{pmatrix}^{-1}\mathbf{B} \tag{3.80}$$

must be performed in the entire calculation procedure of the consistent tangent to obtain the two unknowns $\partial\Delta\varepsilon_p$ and $\partial\Delta\varepsilon_q$. Note that Zhang, who claimed that no inversion is required in this approach, gave the above inverse in analytical form

$$\mathbf{C} = \frac{1}{\det(\bar{\mathbf{C}})}\begin{pmatrix} \bar{C}_{22} & -\bar{C}_{12} \\ -\bar{C}_{21} & \bar{C}_{11} \end{pmatrix}, \tag{3.81}$$

where $\mathbf{C} = \bar{\mathbf{C}}^{-1}$. The stress tensor can then be written as

$$\partial\boldsymbol{\sigma} = \mathbf{C}^{\text{cons}} : \partial\boldsymbol{\varepsilon} \tag{3.82}$$

$$= (\mathbf{J} - K\mathbf{I} \otimes (C_{11}\mathbf{I} + C_{21}\mathbf{n}) - 2G\mathbf{n} \otimes (C_{21}\mathbf{I} + C_{22}\mathbf{n})) : \mathbf{Z} : \partial\boldsymbol{\varepsilon},$$

and the consistent tangent can be extracted in the form

$$\mathbf{C}^{\text{cons}} = (\mathbf{J} - K\mathbf{I} \otimes (C_{11}\mathbf{I} + C_{21}\mathbf{n}) - 2G\mathbf{n} \otimes (C_{21}\mathbf{I} + C_{22}\mathbf{n})) : \mathbf{Z}. \tag{3.83}$$

Equation (3.83) can be formulated in index notation as

$$
\begin{aligned}
C_{ijmn} &= Z_{ijmn} & \text{(3.84)} \\
&- KI_{ij}C_{11}I_{kl}Z_{klmn} \\
&- KI_{ij}C_{12}n_{kl}Z_{klmn} \\
&- 2Gn_{ij}C_{21}I_{kl}Z_{klmn} \\
&- 2Gn_{ij}C_{22}n_{kl}Z_{klmn}.
\end{aligned}
$$

Using an abbreviation of eqn. (3.77) in the form

$$Z_{ijmn} = aJ_{ijmn} + bI_{ij}I_{mn} + cn_{ij}n_{mn} \tag{3.85}$$

and applying the relations

$$I_{kl}I_{kl} = 3, \tag{3.86}$$

$$n_{kl}n_{kl} = \frac{3}{2}, \tag{3.87}$$

$$I_{kl}n_{kl} = 0, \tag{3.88}$$

$$I_{kl}J_{klmn} = I_{mn}, \tag{3.89}$$

$$n_{kl}J_{klmn} = n_{mn}, \tag{3.90}$$

the consistent tangent can be rewritten as

$$
\begin{aligned}
C_{ijmn} &= aJ_{ijmn} + bI_{ij}I_{mn} + cn_{ij}n_{mn} & \text{(3.91)} \\
&- KC_{11}\left(a + 3b\right)I_{ij}I_{mn} \\
&- KC_{12}\left(a + \frac{3}{2}c\right)I_{ij}n_{mn} \\
&- 2GC_{21}\left(a + 3b\right)n_{ij}I_{mn} \\
&- 2GC_{22}\left(a + \frac{3}{2}c\right)n_{ij}n_{mn}.
\end{aligned}
$$

The relations

$$a + 3b = 2G\frac{\sigma_{\text{eq}}}{\sigma_{\text{eq}}^{\text{tr}}} + 3\left(K - \frac{2G}{3}\frac{\sigma_{\text{eq}}}{\sigma_{\text{eq}}^{\text{tr}}}\right) = 3K, \tag{3.92}$$

$$\Delta\varepsilon_{\text{q}} = \frac{\sigma_{\text{eq}}^{\text{tr}} - \sigma_{\text{eq}}}{3G}, \tag{3.93}$$

$$a + \frac{3}{2}c = 2G\frac{\sigma_{\text{eq}}}{\sigma_{\text{eq}}^{\text{tr}}} + \frac{3}{2}\frac{4G^2}{\sigma_{\text{eq}}^{\text{tr}}}\Delta\varepsilon_{\text{q}} = 2G \tag{3.94}$$

lead to the expression of the consistent tangent given by Zhang as

$$
\begin{aligned}
C_{ijmn} &= a J_{ijmn} + b I_{ij} I_{mn} + c n_{ij} n_{mn} \\
&\quad - 3K^2 C_{11} I_{ij} I_{mn} \\
&\quad - 2KG C_{12} I_{ij} n_{mn} \\
&\quad - 6KG C_{21} n_{ij} I_{mn} \\
&\quad - 4G^2 C_{22} n_{ij} n_{mn}.
\end{aligned}
\tag{3.95}
$$

The consistent tangent for the "standard" J_2 plasticity (pressure-independent) model with an isotropic hardening rule as used for the DDIT model in the undamaged state, see tab. 3.2, described by the yield function

$$
\Phi = \sigma_{eq} - \sigma_f(\varepsilon_{eq}^{pl}) = 0
\tag{3.96}
$$

and the state variable $H_1 = \varepsilon_{eq}^{pl}$, can be derived by the above algorithm as well. Plugging the above yield function into eqn. (3.63) will lead to

$$
\partial \Phi = \left(\frac{\partial \Phi}{\partial \sigma_{eq}} \frac{\partial \sigma_{eq}}{\partial \boldsymbol{\sigma}} \right) : \partial \boldsymbol{\sigma} + \frac{\partial \Phi}{\partial H_1} \partial H_1 = \mathbf{n} : \partial \boldsymbol{\sigma} - \sigma_f' \partial \varepsilon_{eq}^{pl} = 0
\tag{3.97}
$$

with

$$
\sigma_f' = \frac{\partial \sigma_f}{\partial \varepsilon_{eq}^{pl}}.
\tag{3.98}
$$

This equation can be transformed into the above framework by setting the following constants of eqn. (3.67) and eqn. (3.68):

$$
\begin{array}{llll}
A_{11} = 1 & A_{12} = 0 & A_{21} = 0 & A_{22} = -\sigma_f' \\
B_{11} = 0 & B_{12} = 0 & B_{21} = 0 & B_{22} = -1
\end{array}
$$

The algorithm proposed by Zhang then leads to a consistent tangent of the form

$$
\mathbf{C}^{cons} = 2G \frac{\sigma_{eq}}{\sigma_{eq}^{tr}} \mathbf{J} + \left(K - \frac{2G}{3} \frac{\sigma_{eq}}{\sigma_{eq}^{tr}} \right) \mathbf{I} \otimes \mathbf{I} - \frac{4G}{3} \left(\frac{3G}{3G + \sigma_f'} - 1 + \frac{\sigma_{eq}}{\sigma_{eq}^{tr}} \right) \mathbf{n} \otimes \mathbf{n}.
\tag{3.99}
$$

Note that all necessary derivations for the evaluation of a consistent tangent for the GTN model and for the extended Rousselier model (#5) are given in appendix D and in appendix E, respectively.
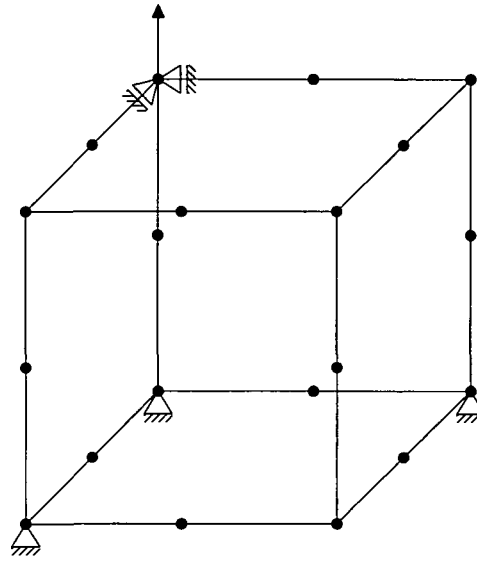
Figure 3.6: Geometry for single element test with periodicity boundary conditions
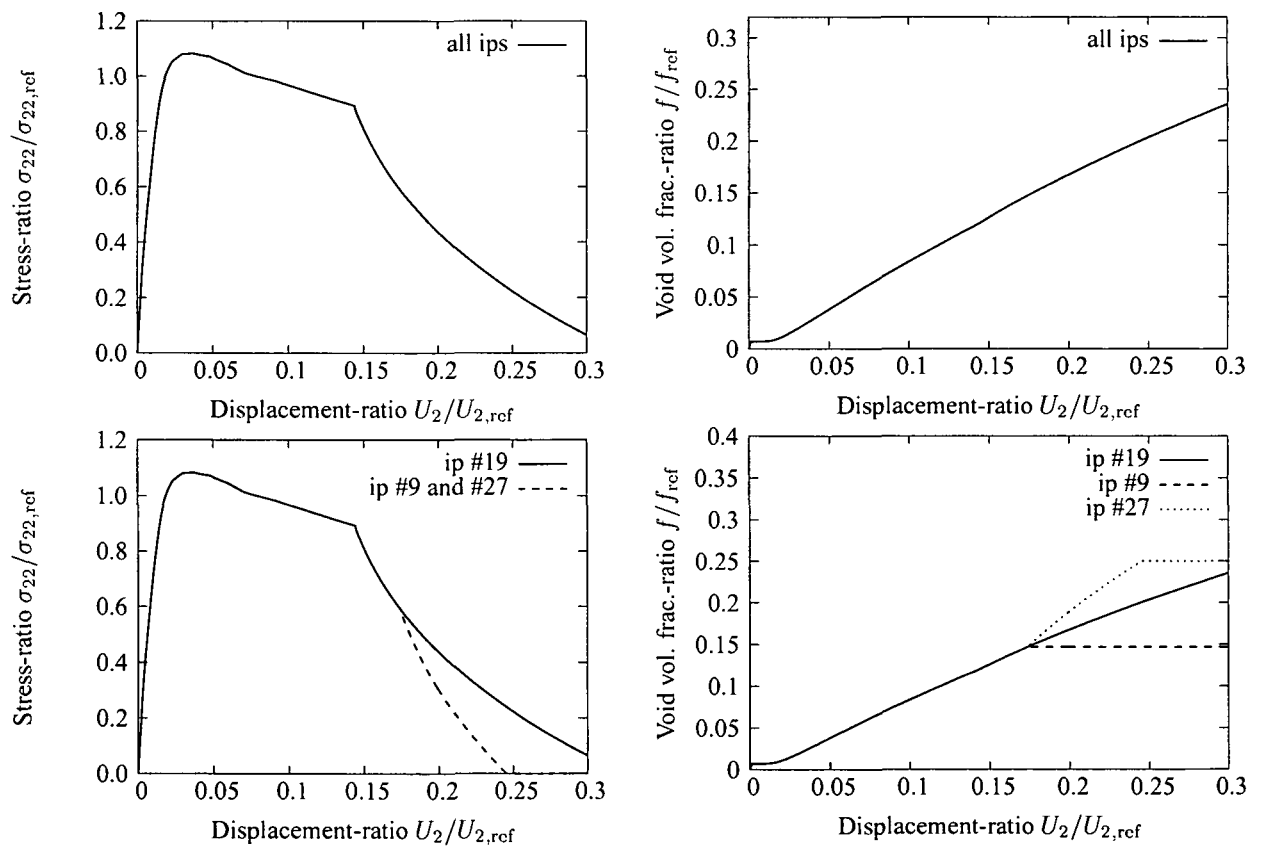

Figure 3.7: Single element test with consistent (top) and incorrect tangent (bottom)

3.4 Implementation of the Nonlocal Regularization Technique

The present work employs an integral-type nonlocal averaging approach which is based on smoothing the increment of an appropriate damage variable, Δq, according to an algorithm given by Leblond et al. [56]. The method is described by eqn. (2.27) and eqn. (2.28) and can be rewritten in combination with eqn. (2.29) as

$$\Delta q_{NL}(\mathbf{x}_i) = \frac{1}{W(\mathbf{x}_i)} \sum_{j=1}^{n} \Delta q_{L}(\hat{\mathbf{x}}_j) \left[\frac{1}{1 + \left(\frac{|\mathbf{x}_i - \hat{\mathbf{x}}_j|}{L} \right)^8} \right]^2 \hat{V}_j \qquad (3.100)$$

with

$$W(\mathbf{x}_i) = \sum_{j=1}^{n} \left[\frac{1}{1 + \left(\frac{|\mathbf{x}_i - \hat{\mathbf{x}}_j|}{L} \right)^8} \right]^2 \hat{V}_j, \qquad (3.101)$$

in order to use the algorithm in a numerical procedure.

Here q_{L} is the local damage variable and q_{NL} is its nonlocal counterpart, $|\mathbf{x}_i - \hat{\mathbf{x}}_j|$ stands for the distance between two integration points i and j, $\hat{V}_j$ is the volume associated with integration point j, and the sums run over all integration points j within a distance L from a given integration point i as sketched in fig. 3.8.

The user subroutine UEXTERNALDB available in ABAQUS/Standard allows the user to perform any operations at the

- beginning of an analysis (LOP = 0),

- beginning of a restart analysis (LOP = 4),

- beginning of an increment (LOP = 1),

- end of an increment (LOP = 2),

- end of an analysis (LOP = 3),

where LOP stands for a variable provided by ABAQUS/Standard that indicates the actual state when UEXTERNALDB is called.

The averaged increment of the damage variable in eqn. (3.100) is evaluated only at the end of each increment, where the local values, Δq_{L}, are available and equilibrium has been

achieved. While this constitutes a considerable restriction when compared to research codes, where averaging may take place for each iteration, compare e.g. Baaser and Tvergaard [60], tests showed good agreement between the two types of algorithms as can be seen in fig. 3.9, where shear band localization was induced by a small imperfection in the right bottom corner of a plane strain tensile test specimen loaded in the vertical direction. For efficient nonlocal smoothing via eqns. (3.100) and (3.101) it is obviously desirable to have suitable information on those neighbors of any given integration point available that lie within the half of the characteristic length, L. Such data, comprising e.g. integration point volumes and the distances between pairs of integration points, can be evaluated and stored at the start of the analysis and may be updated as required. The ABAQUS vector COORD (coordinates) and the variable IVOL (integration point volume) can be extracted via the c++ or python scripting interfaces that provide access to the data stored in the ODB files of ABAQUS. These scripts must be started at the beginning of the nonlocal analysis in any case to obtain the necessary relations between the integration points and can be employed during the simulation as well to get an actual setting. For that reason, lists of data for each integration point are stored in a FORTRAN common block and are thus kept in memory to ensure efficient access throughout the analysis. For each integration point i the list identifies all neighbors j that lie within the distance L and gives the factors

$$p_1 = \left[\frac{1}{1 + \left(\frac{|x_i - \hat{x}_j|}{L} \right)^8} \right]^2 \hat{V}_j \tag{3.102}$$

that are required for evaluating eqn. (3.100). Figure 3.10 shows a short section of such a list and considerations about the expected memory requirements depending on the mesh size h and the characteristic length $2L$ is given in subsection 4.2.1.

Following each load increment the nonlocal increment of the damage variable, $\Delta q_{\mathrm{NL}}^{t+\Delta t}$, can then be evaluated from the local values, $\Delta q_{\mathrm{L}}^{t}$. The smoothened value of the damage variable is obtained as

$$q_{\mathrm{NL}}^{t+\Delta t} = q_{\mathrm{NL}}^{t} + \Delta q_{\mathrm{NL}}^{t+\Delta t}, \tag{3.103}$$

and is available for the next increment, compare the sketch in fig. 3.11 and fig. 3.12. New values for q_{L} are evaluated during each equilibrium iteration, the corresponding $\Delta q_{\mathrm{L}}^{t}$ must be transferred from the UMAT into the UEXTERNALDB and the new values of $\Delta q_{\mathrm{NL}}^{t+\Delta t}$ must be passed back. This is again achieved via common variables (see subsection 3.6 for important notes on the usage of common variables within ABAQUS user subroutines).

In order to provide correct results, the smoothing algorithm must ignore all integration points that have reached failure. In analyses where both ductile and elastic materials

are present, as is the case in micromechanical studies of MMCs, the smoothing must be restricted to the ductile constituent. Furthermore, appropriate provisions must be made for the symmetry or periodicity boundary conditions that are typically employed in unit cell analyses, compare fig. 3.13. There the basic unit cell is drawn in bold lines, thin lines designate "copies" of the unit cell, a given integration point is marked by a "+", and a circle of radius L centered on it indicates the characteristic length within which integration points contribute to the nonlocal averaging. In the case of symmetry boundary conditions the "mirror images" of the integration points with respect to each symmetry plane must be included in the averaging procedure, and periodicity boundary conditions require that unit cells shifted by multiples of the vectors of periodicity must be considered. Note that the "integration regions" typically do not follow mirror symmetries in the case of symmetry boundary conditions.

It is worth pointing out that it is absolutely necessary to employ the increments of the damage variable for averaging according to eqn. (2.27) rather than the damage variable itself. In the latter case regions where elastic unloading occurs due to stress redistribution ($\Delta q = 0$, but $q \neq 0$) can influence the nonlocal averages in an unphysical way.

● integration point i

✕ n integration points (j's) considered for the evaluation of integration point i
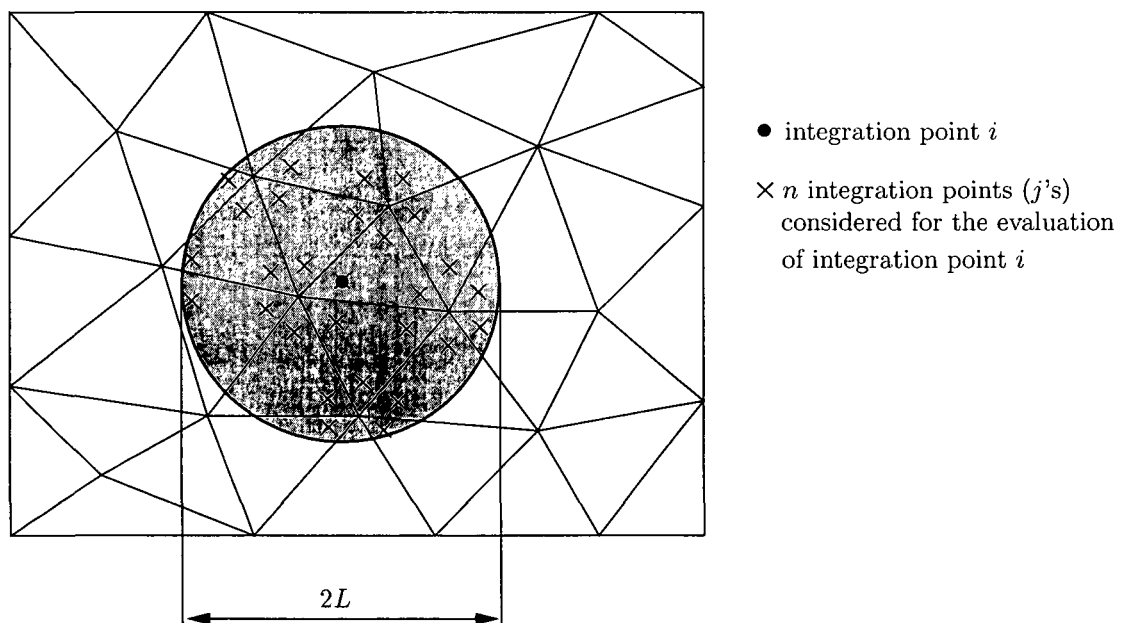
Figure 3.8: Finite element mesh with integration points considered in the nonlocal averaging algorithm for integration point i lying within the characteristic length $2L$
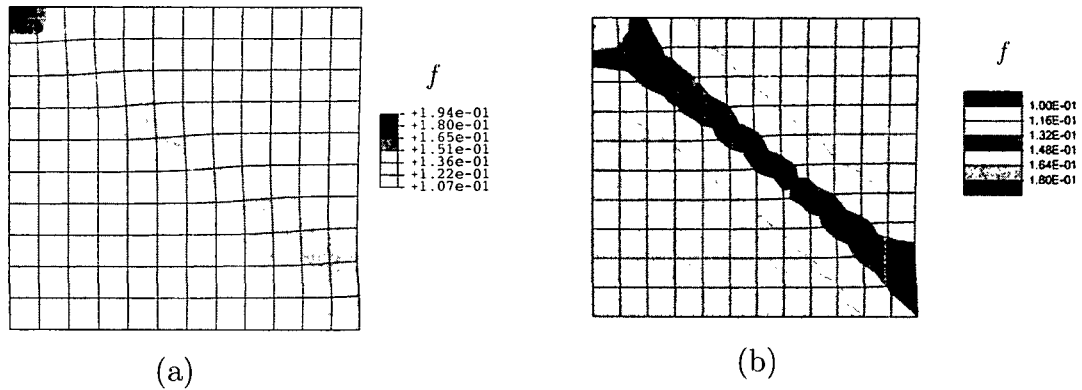
Figure 3.9: Shear band localization — comparison of (a) results from the present nonlocal
Rousselier procedure and (b) predictions published in [60]

Figure 3.10: A small section of a list storing the spatial relation between integration points
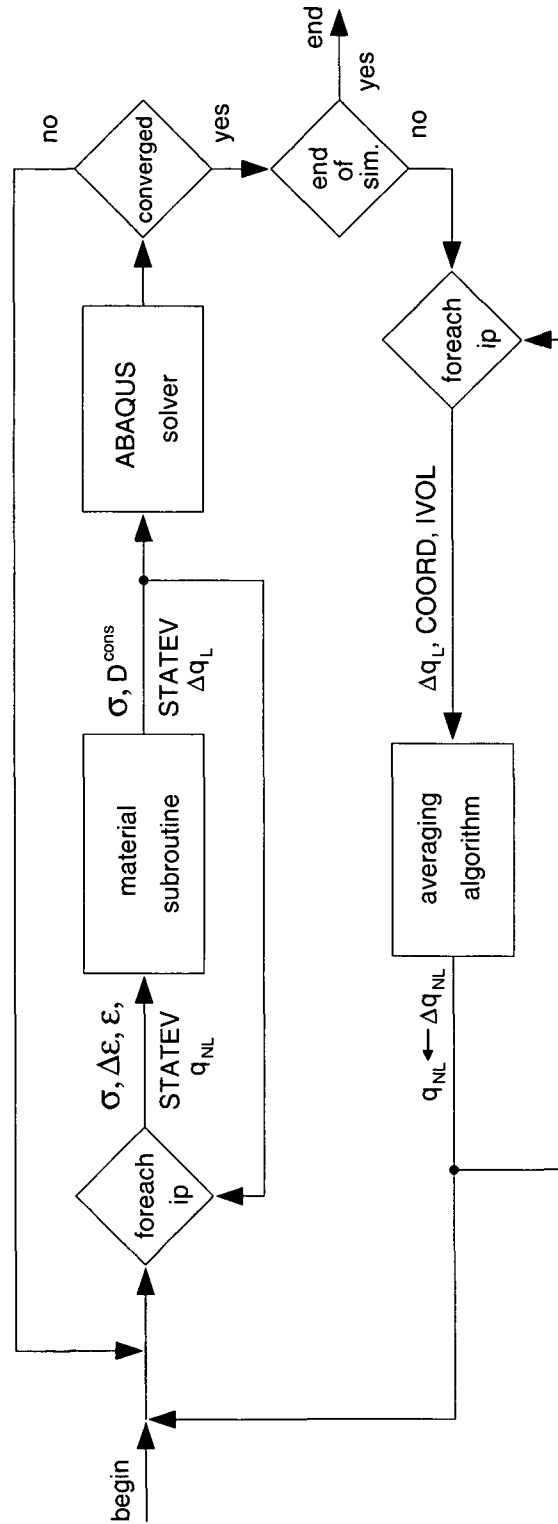used for handling the integral-type nonlocal averaging within ABAQUS/Standard

Figure 3.11: Implementation of the nonlocal averaging algorithm in the ABAQUS/Standard framework

$$q_{\mathrm{NL}}^{t} = q_{\mathrm{NL}}^{t-\Delta t} + \Delta q_{\mathrm{NL}}^{t} \qquad\qquad\qquad q_{\mathrm{NL}}^{t+\Delta t} = q_{\mathrm{NL}}^{t} + \Delta q_{\mathrm{NL}}^{t+\Delta t}$$

| incr. $n-1$ | t | increment n calculation of Δq_{L} | $t + \Delta t$ | incr. $n+1$ |

evaluation of $\Delta q_{\mathrm{NL}}^{t}$ (eqn. (3.100))   evaluation of $\Delta q_{\mathrm{NL}}^{t+\Delta t}$ (eqn. (3.100))
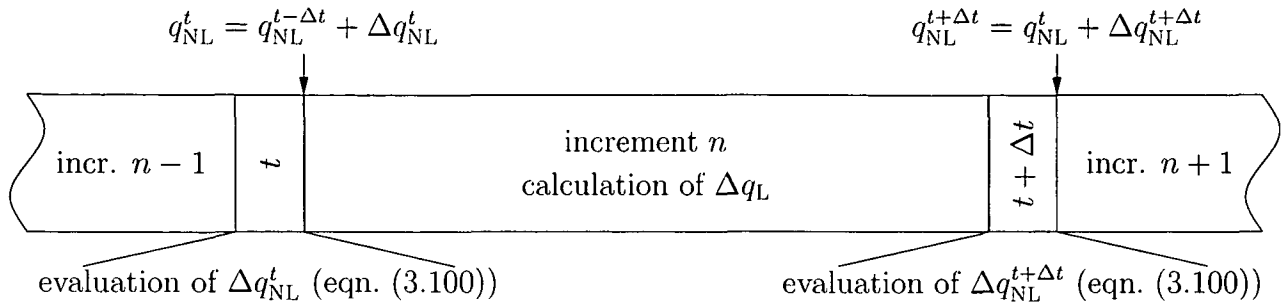
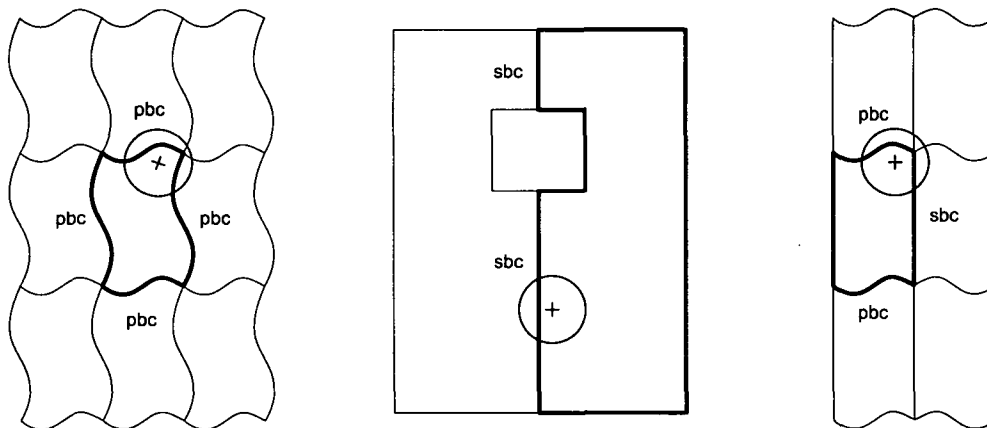Figure 3.12: Sequence of operations performed by the smoothing algorithm

Figure 3.13: Unit cell geometries with periodicity (pbc) and symmetry (sbc) boundary conditions. Regions contributing to the nonlocal averages of Δq_{NL} for given integration points "+" are marked as circles

3.5 Single Element Tests and Comparisons

Comparisons were carried out between unit cell models containing resolved voids in a simple cubic arrangement, compare fig. 3.14, and smeared-out models employing the three ductile damage algorithms described above (the Rousselier model was used in both its original form and in the extended version #5). A similar test was used by Prahl et al. [99] for calibration of the material parameters of the ductile damage models. Furthermore, the influence of selected material parameters of the three ductile damage models was explored for different kinds of load cases.

The material of the unit cell with the resolved void was assumed to be elastoplastic and

the flow stress was described by the Ludwik hardening law given in eqn. (2.26). The elastic
and elastoplastic material parameters are listed in tab. 2.1 on page 28.

The additional material parameters for the ductile damage models are listed in tab. 3.8.
The initial void volume fraction was chosen as $f_0 = 7 \times 10^{-3}$, which determined the size of
the single void in the unit cell in fig. 3.14.

Four different loading scenarios corresponding to different displacement controls were ap-
plied to both the unit cell and the single elements using the different damage models.
Periodicity boundary conditions were used in all cases.

The force–displacement responses predicted with the three damage models for the four
sets of loading conditions are displayed in fig. 3.15 and fig. 3.16. The numbers beside the
arrows in the inserted sketches of the unit cell indicate the multipliers of the displacement
amplitudes.

The load cases can be seen to comprise two nonsymmetric triaxial load cases (#1, #2), a
uniaxial tensile load case (#3), and tensile hydrostatic loading (#4). The DDIT model was
not used in the latter scenario, because this model cannot handle ductile damage under
purely hydrostatic loading, compare section 3.2.

The yield surface of the "original" Rousselier model shows a vertex for purely hydrostatic
stress states as mentioned in section 3.2, so that associated flow descriptions run into prob-
lems at high stress triaxialities (which occur commonly under the constrained plasticity
conditions typical of micromechanical analyses) and no result was obtained with this model
in loading scenario #4, whilst the extended Rousselier model described in section 3.2 can
handle this stress state without any problems. Furthermore, it is worth noting, that the
above extension of the Rousselier model does not markedly change the results in compar-
ison to the original Rousselier model, with the exception of loading scenario #3, where
softening occurs at quite different loads. While not fully satisfactory this behavior was as-
sessed as acceptable for micromechanical analyses where a wide range of stress triaxialities
is present at the microscale for any given macroscopic load state.

By correlating the overall responses obtained, on the one hand, from the three ductile dam-
age models and, on the other hand, from the unit cells containing a single void, suitable
values for the modeling constants in the above models can also be estimated, see tab. 3.8.
The best agreement to the behavior predicted by the unit cell model was obtained with the
GTN model[2], followed by the Rousselier model. The DDIT model can resolve the onset of
damage, but does not correctly describe the behavior of the unit cell containing a single
void after that point. The unit cell model does not show the inflexion points observed in

---

[2]This is not surprising, because the GTN model is based on a single-void unit cell.

the Rousselier and GTN models, which are due to void coalescence.

Such comparisons between unit cell and damage models, while shedding light on many features of the behavior of the latter, cannot, of course, take the place of full-blown parameter identification procedures for a given material as reported e.g. by Springmann and Kuna [100], [101].

In addition it must be kept in mind that the unit cell shows cubic symmetry and, accordingly, anisotropic overall behavior, whereas the damage models are designed to be isotropic. After varying the material properties in all models, the author concluded that it appears impossible to find sets of material parameters that allows to obtain identical or nearly identical results with the different ductile damage models for a set of different loading scenarios. Furthermore, it turns out that materials characterized by a ductile behavior in the softening regime (e.g. Al2618-T4, the matrix of Aluminum Silicon Carbide (Al/SiC_p) metal matrix composite) can be described quite well by the Rousselier model, whilst the DDIT model is best applied for materials where the damage behavior shows limited macroscopic ductility even though dimples are present at the fracture surface, indicating a ductile failure mechanism. The GTN model should be used for materials showing a very ductile stress strain behavior, even more so than materials suitable for the Rousselier model.

One can see that the implemented damage models are sufficient for simulating crack initiation and propagation in a wide range of different kinds of ductile materials.

In order to get a better insight into the behavior of such damage models once the material parameters are varied, a number of single element tests were performed with different sets of material parameters using the loading condition of scenario #1. These tests were based on the material parameters listed in tab. 3.8, but one parameter was varied at a time to see the corresponding effect. Three material parameters, q_1, q_2 and f_0 in the GTN model[3], q_4, $\tilde{D}$ and f_0 in the extended, modified Rousselier model (#5) and the only material parameter ε_0 of the DDIT model were changed independently and the results are depicted in fig. 3.17, fig. 3.18 and fig. 3.19. It is evident from the force-displacement diagrams that the variation of any one of the three material parameters in the GTN model leads to a nearly parallel shift of the force–displacement curves towards higher or lower forces and hence mainly influences the maximum load carrying capacity and the energy required for crack growth. Among the parameters considered, changes of q_2 influence the results most markedly (giving changes of up to 20% in maximum force for a 10% change in q_2). The results performed with the extended Rousselier (#5) model shows a completely different

---

[3]Variation of q_1 leads to a modification of q_3 following the relation $q_3 = q_1^2$ as mentioned in subsection 3.2.

behavior. On the one hand, the maximum force $RF_{2,\mathrm{max}}$ is influenced by changing the values of the material parameters, and, on the other hand, the point of final failure ($RF_2 = 0$) varies within a wide range. The initial void volume fraction, f_0, has only a small influence on the local behavior of the element as also observed with the GTN model. The initiation of ductile failure in an element driven by the DDIT model depends on ε_0 and can be delayed by using a higher number of the material parameter in accordance with eqn. (3.40).

GTN	q_1	q_2	q_3	f_c	f_f	f_0	
	1.5	0.9	2.25	0.12	0.25	7×10^{-3}	

orig. and ext. Rousselier	σ_1 [MPa]	q_4	$\tilde{D}$	f_c	f_F	f_0
	320	1.2	2	0.15	0.9	7×10^{-3}

DDIT	ε_0
	0.2

Table 3.8: Material properties obtained by comparing unit cell with pore and smeared-out models

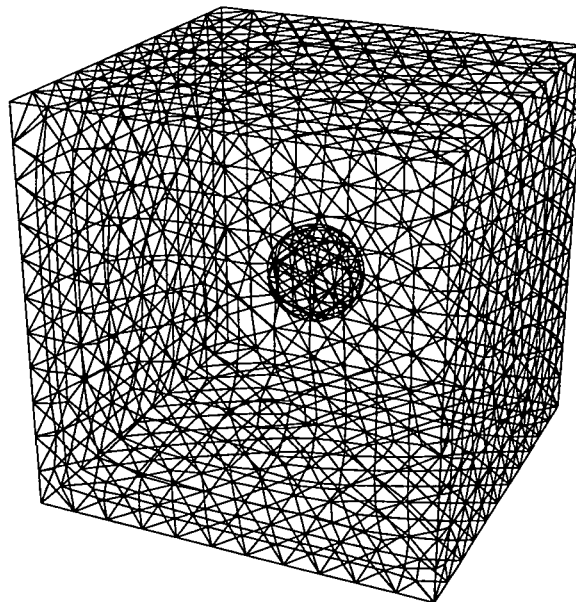Figure 3.14: Unit cell containing a single central void

Scenario #1: nonsymmetric triaxial tensile loading
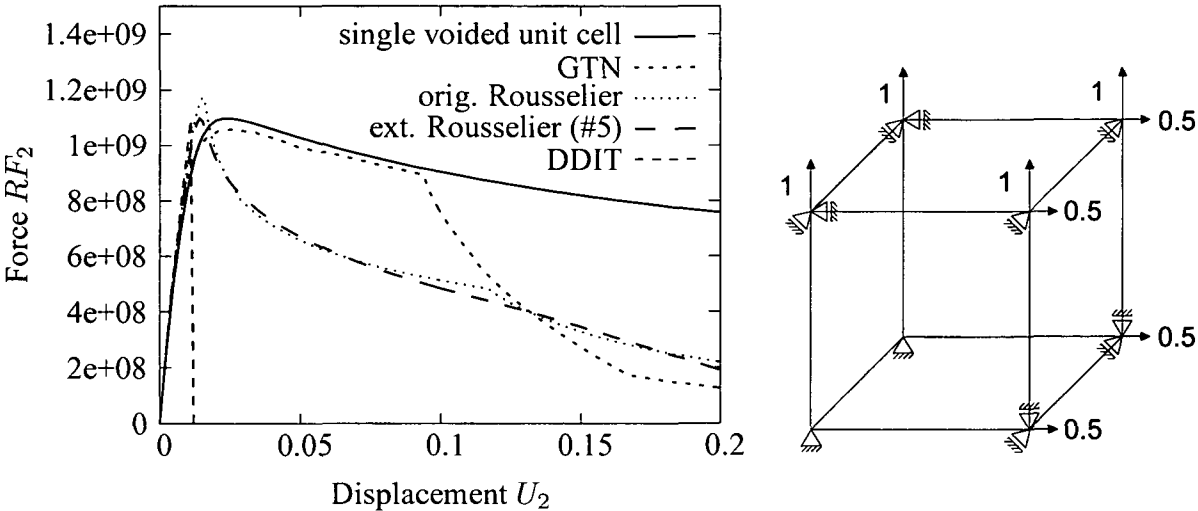
Scenario #2: nonsymmetric triaxial tensile loading

Figure 3.15: Force–displacement responses obtained with loading scenarios #1 and #2

Scenario #3: uniaxial tensile loading

Scenario #4: hydrostatic loading

Figure 3.16: Force–displacement responses obtained with loading scenarios #3 and #4

Figure 3.17: Force–displacement responses obtained by varying individual material parameters for the GTN model using loading scenario #1

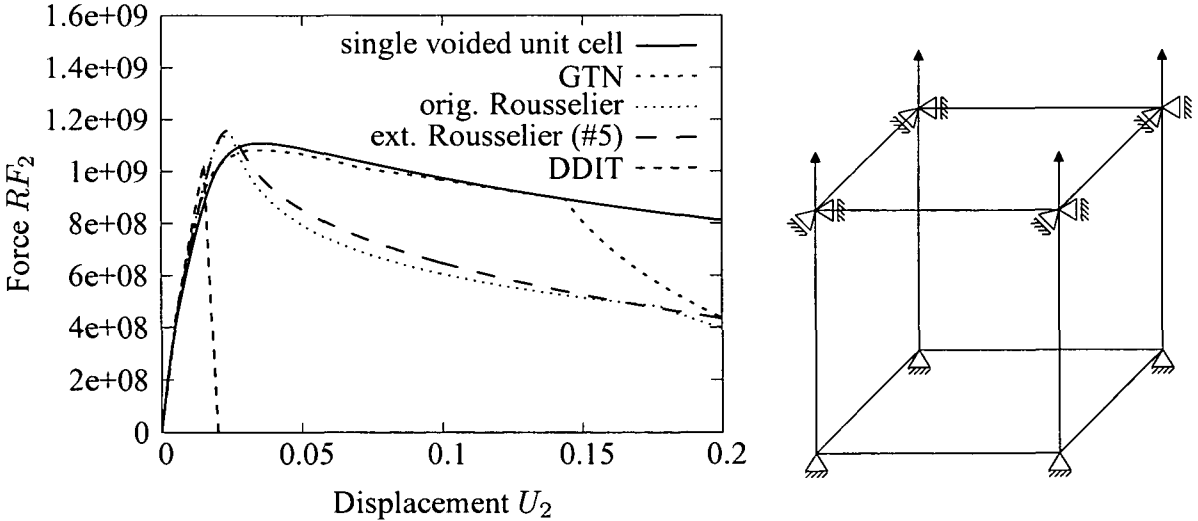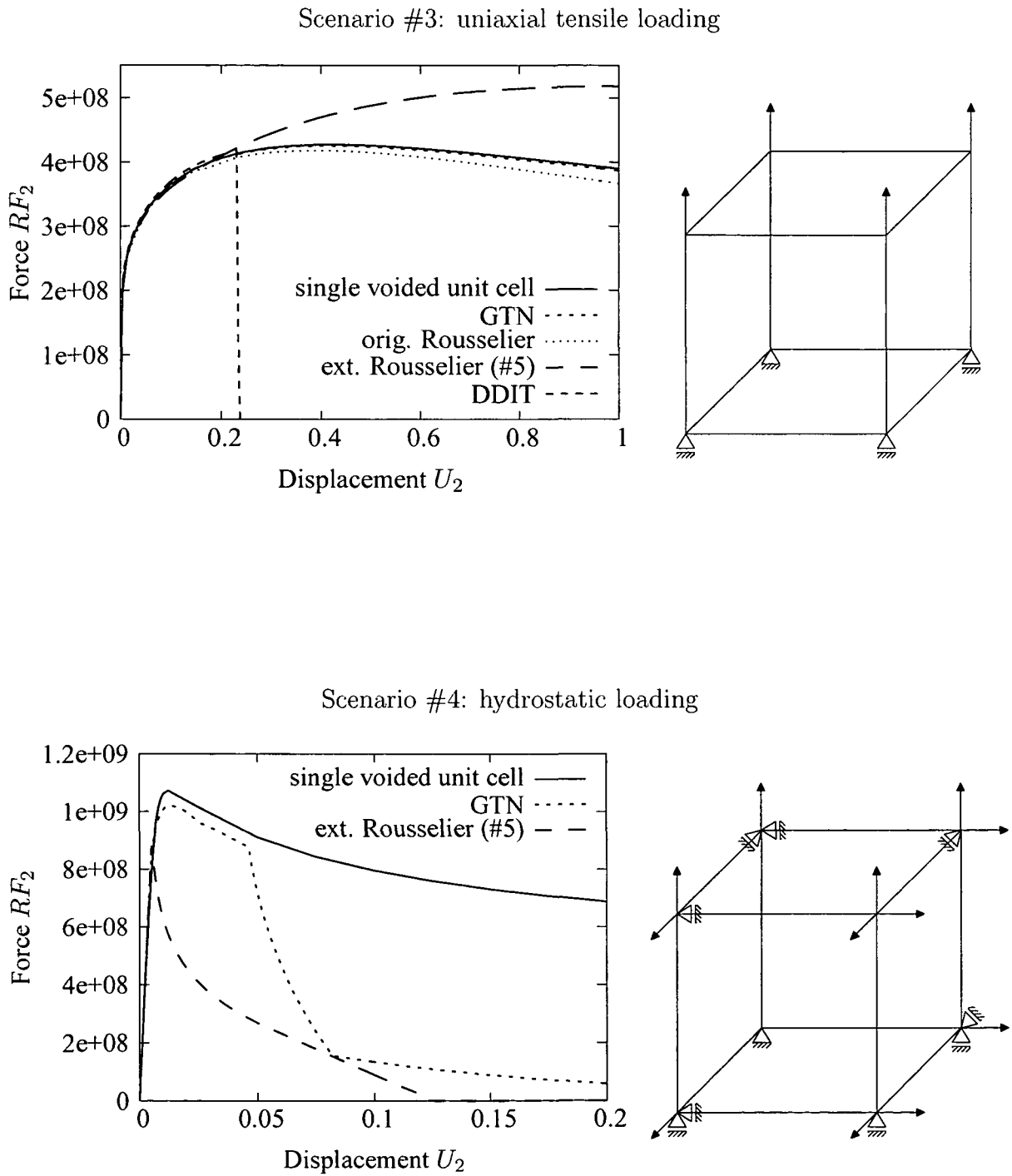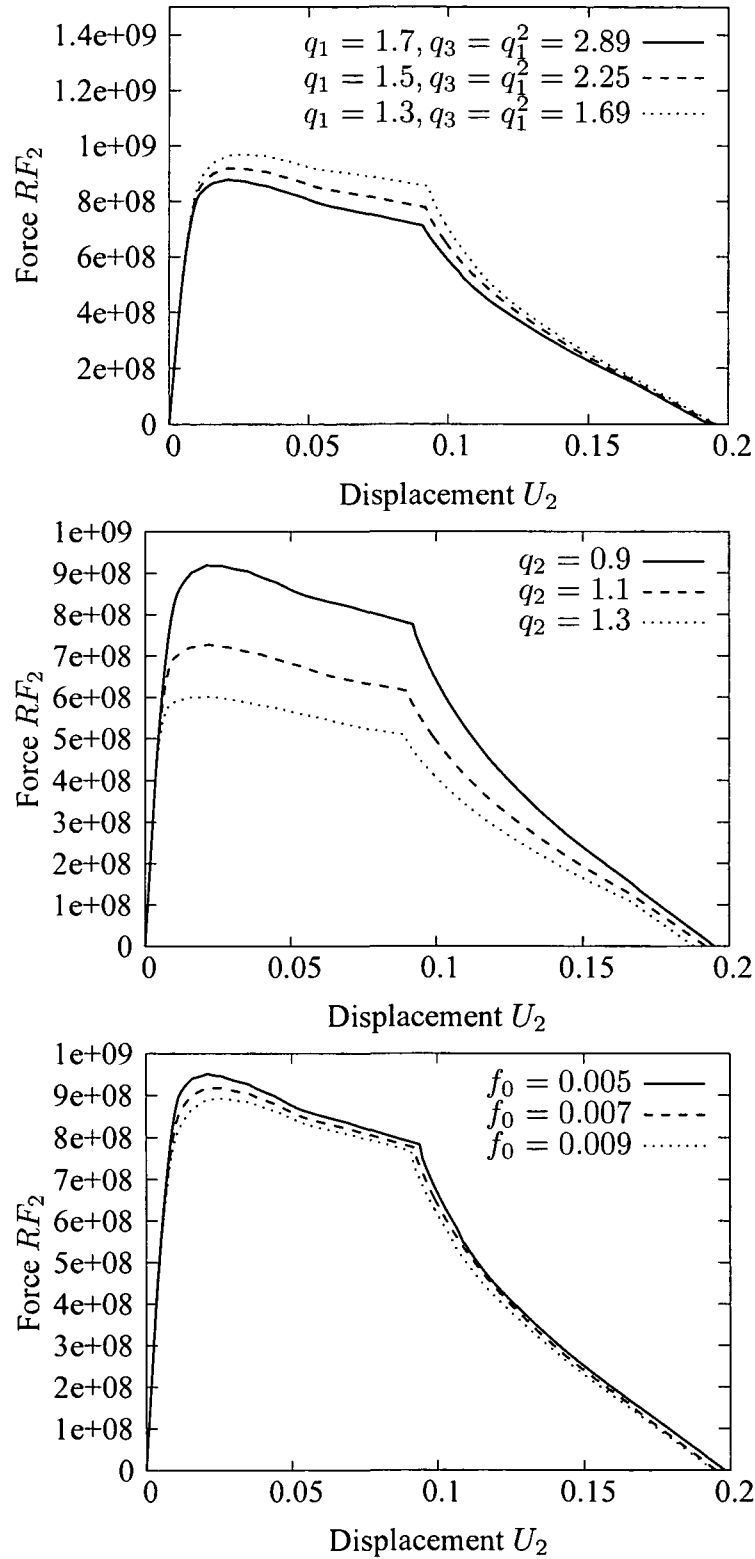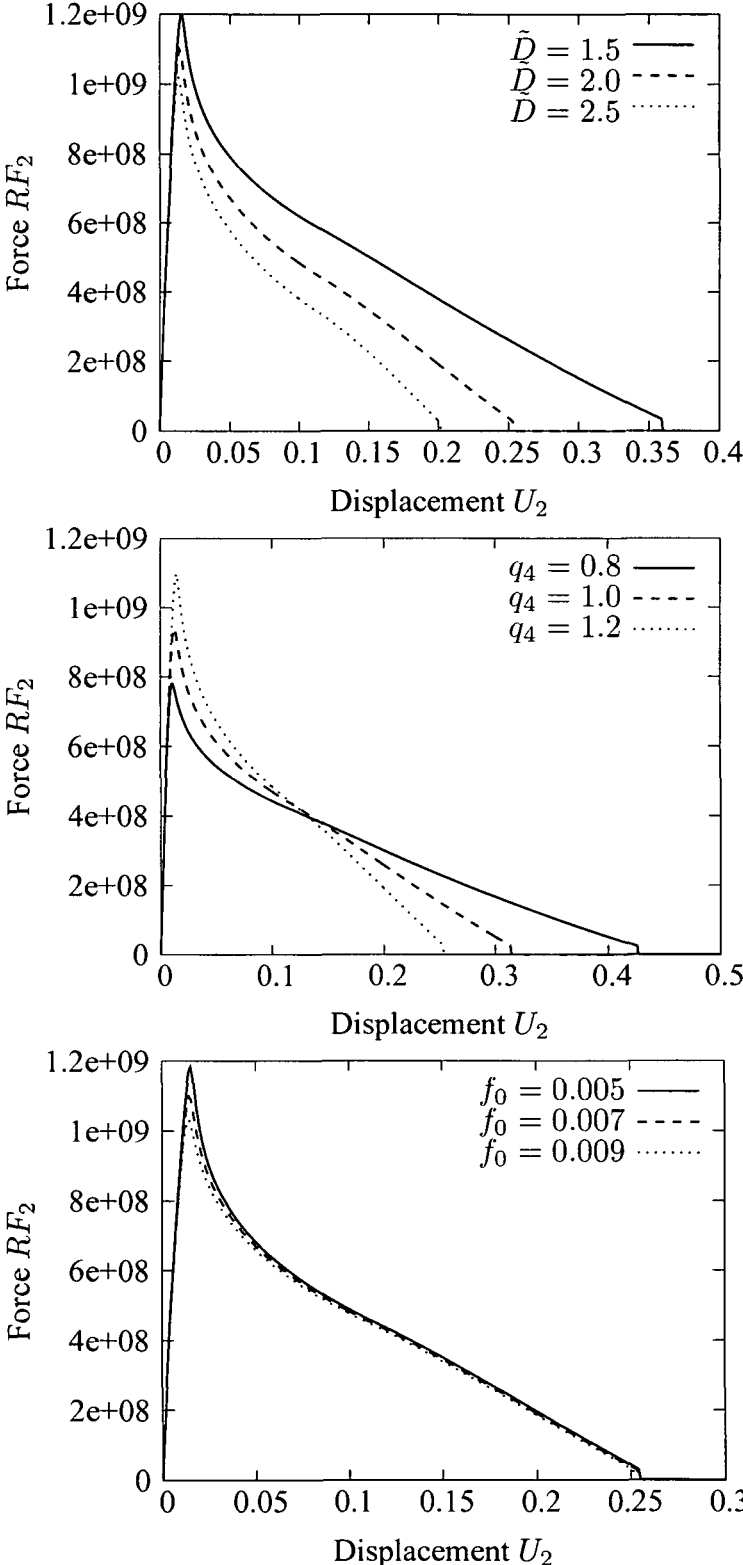Figure 3.18: Force–displacement responses obtained by varying individual material parameters for the extended Rousselier (#5) model using loading scenario #1
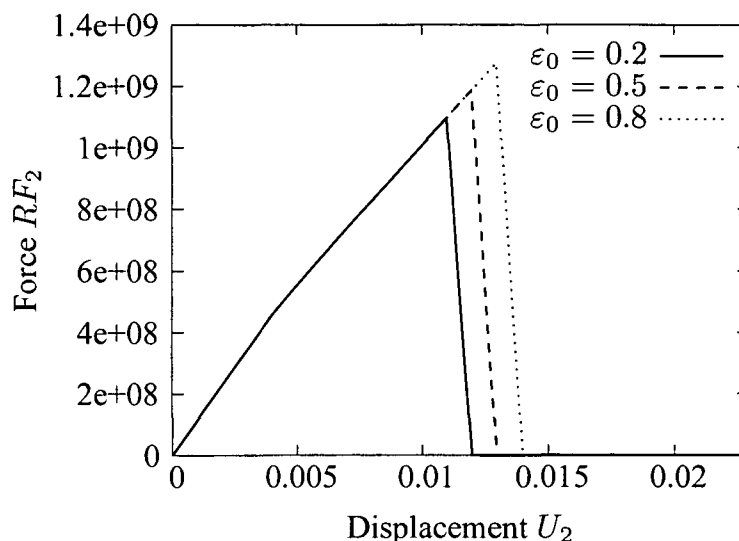
Figure 3.19: Force–displacement responses obtained by varying individual material parameters for the DDIT model using loading scenario #1

3.6 Technical Details

The author wants to point out the difference between using state variables, STATEV, and common variables, COMV, in ABAQUS/Standard user subroutines. The state variables are managed by ABAQUS in such a way that the previous ("old") values of the variable are available when convergence is not reached and a new iteration or new attempt[4] has to be performed. Common variables, in contrast, must be organized by the user and provision must be made to hold the old and the new values in memory. The difference can be explained in a simple example:

Assume that the state variable STATEV and the common variable COMV are equal to 1 at the beginning of an increment, then the equations

$$STATEV = STATEV + 1, \tag{3.104}$$

$$COMV = COMV + 1, \tag{3.105}$$

which are assumed to be implemented in the ABAQUS/Standard user subroutine UMAT will lead to the values of STATEV = 2 and COMV = 11 after the solver has performed 10 iterations for finding the state at the end of the increment.

---

[4]An attempt in ABAQUS/Standard can be explained as a new start of an increment if the previous one did not converge.

Furthermore, the different handling of state variables in a user defined subroutine UMAT
and in a user defined field subroutine USDFLD should be outlined. This difference can be
explained in an example where the equivalent plastic strain, ε_{eq}^{pl}, is calculated. The UMAT
subroutine is called at the beginning of the increment inc at time t and the old value of
ε_{eq}^{pl} stored in STATEV can be used to calculate the new value at the end of the increment at
time $t + \Delta t$:

$$STATEV_{t+\Delta t} = STATEV_t + \Delta \varepsilon_{eq,inc}^{pl} \qquad (3.106)$$

The USDFLD subroutine, in contrast, is called at the beginning of the increment as well, but
the increment of the equivalent plastic strain, $\Delta \varepsilon_{eq}^{pl}$, is calculated during the increment by
ABAQUS in an internal procedure and cannot be accessed at the beginning of the increment
by the user, who can only store $\Delta \varepsilon_{eq,inc-1}^{pl}$ into STATEV from the previous increment to give

$$STATEV_{t+\Delta t} = STATEV_t + \Delta \varepsilon_{eq,inc-1}^{pl}. \qquad (3.107)$$

This leads to a "delayed" behavior of the ductile damage indicator in eqn. (3.40) calcu-
lated with the USDFLD in comparison to the UMAT as shown in fig. 3.20. Nevertheless, the
differences between the two results were found to be limited in a number of tests provided
that the load increments are chosen sufficiently small.

It should be mentioned that the implementations of the above local ductile damage models
into an ABAQUS/Standard UMAT require the removal of damaged elements after a number
of increments, because otherwise the low stiffnesses of the "failed" elements can lead to
numerical difficulties which manifest themselves in ABAQUS failing to reach convergence
and breaking off the analysis. This procedure can be applied in a restart analysis by using
the MODEL CHANGE command of ABAQUS/Standard to remove the elements from the
finite element mesh that have reached the final failure criterion.

A more convenient way for removing such elements is provided in ABAQUS/Explicit where
each integration point can be deactivated during the simulation by a flag accessible in the
user defined material subroutine (VUMAT). However, ABAQUS/Explicit does not offer the
broad range of user subroutines available in ABAQUS/Standard and hence it was not
possible to implement the nonlocal averaging method presented in section 3.4 into the
ABAQUS/Explicit framework.

It is worth noting that special provisions are required for applying the nonlocal averaging
approach to a composite where two or more constituents are involved not all of which are

to be considered in the smoothing process[5]. Figure 3.21 depicts such a composite material in 2D, two locations where the averaging will occur being pictured by two circles. Circle 1 is located in material 1 only and all integration points in the circle are considered, whilst circle 2 spans both constituents and only integration points of material 1 are involved in eqn. (3.100). Nonlocal averaging in only one phase can be implemented in a fairly straight-forward way. It should be kept in mind, however, that the resulting smoothing domains may be very small in some situations, leading to a nearly local solution at such points.

Furthermore, when the above nonlocal algorithm is used, one has to decide if a completely damaged integration point in the finite element mesh should be considered in eqn. (3.100) or not. Although the increment of the damage variable, Δq_L, is equal to zero for an integration point that has reached final failure, this integration point would influence eqn. (3.100) by the factor $W(\mathbf{x}_i)$ defined in eqn. (3.101) that remains finite. In both cases a problem arises that is sketched in fig. 3.22, where two regions of the material that are connected by "deleted" elements (a crack) are still able to "communicate" via the nonlocal procedure, which is an unphysical behavior. At present such situations are not taken into account, because integration points in close neighborhood to failed elements (i.e. to a crack) have a high likelihood of unloading elastically, in which case, of course, the increment of the damage variable is zero.

Simulations including softening in quasi-static problems as treated in this work are best handled in ABAQUS/Standard with the STABILIZE option that adds artificial damping to the system of equations to deal with load redistribution effects upon the failure of elements. This procedure introduces viscous forces of the form

$$VF_i = cM_{ij}^*V_j, \tag{3.108}$$

where $\mathbf{M}^*$ is an artificial mass matrix calculated with unity density, $\mathbf{V}$ is the vector of nodal velocities

$$V_j = \frac{\Delta U_j}{\Delta t} \tag{3.109}$$

calculated from the displacement increment $\Delta \mathbf{U}$ and the time increment Δt that corresponds to the load increment in a quasi-static analysis and has no physical meaning in this context. The parameter c in eqn. (3.108) is the so-called damping factor, which is determined automatically at the beginning of the simulation unless specified otherwise by

---

[5]At present the nonlocal averaging is implemented for one constituent only (i.e. the ductile matrix, the reinforcements being assumed not to fail in a ductile mode). If more than one ductile phase is present, it appears physically reasonable to apply the smoothing to each phase separately.

the user. In order to obtain a useful prediction of the damping factor, ABAQUS assumes
that the problem to be stable at the beginning of the step, where the calculation of c will
occur. If this stabilizing utility is used, it is important to compare the viscous forces, **VF**,
and the calculated nodal forces, **RF**, to make sure that the viscous forces do not dominate
the solution. In a restart analysis, the damping factor of the previous run should be used
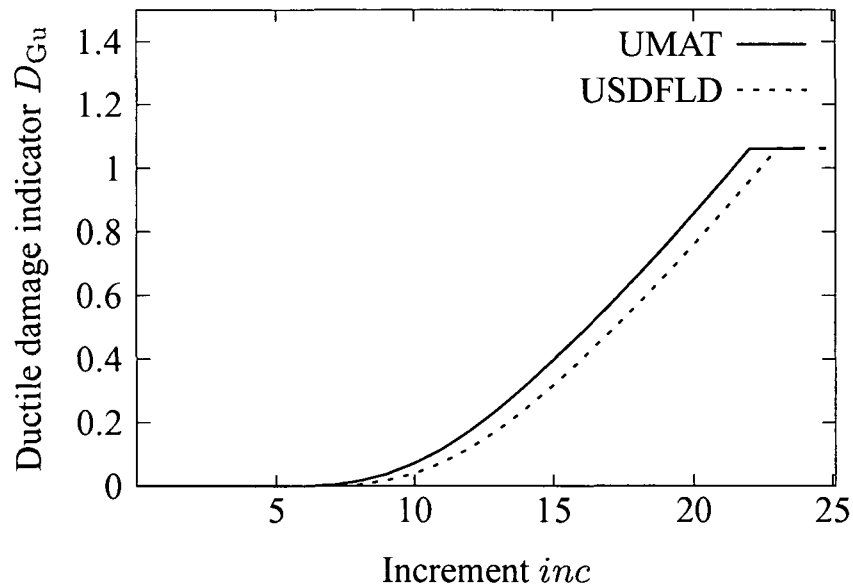and can be detected in the ABAQUS message file.

Figure 3.20: "Time shift" in the evaluation of a ductile damage indicator using the UMAT
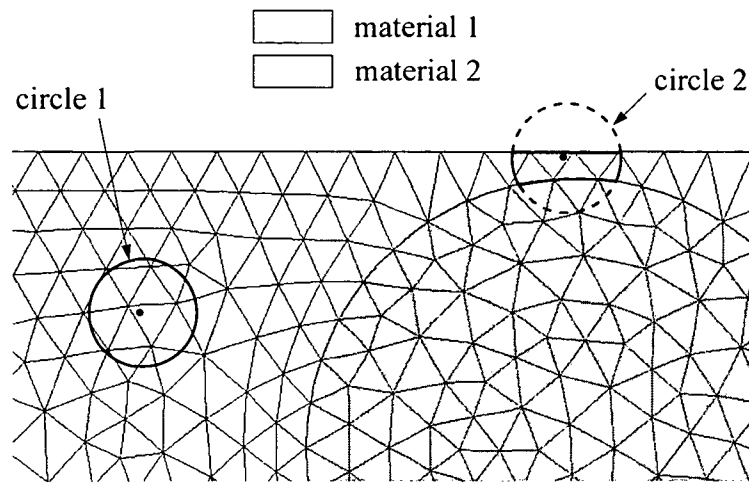and the USDFLD subroutine

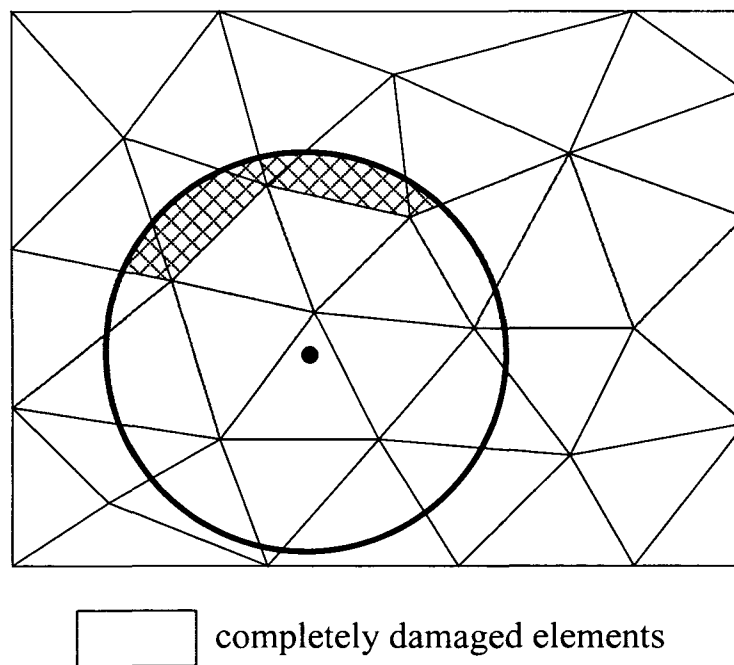Figure 3.21: Nonlocal averaging in a composite material

Figure 3.22: Unphysical averaging including the process zone and regions (hatched) that are separated from the active integration point by failed elements

Chapter 4

Simulation of Ductile Damage in Metal Matrix Composites

The nonlocal damage routines discussed in chapter 3 were applied to modeling the behavior of the matrix of composites containing elastic reinforcements to observe the influence of the reinforcement size and arrangement on matrix failure. In the following the material properties of the ductile matrix correspond to Al2618–T4 and those of the fibrous or particulate reinforcements to SiC. The material parameters necessary for the ductile damage models are given in tab. 3.8 on page 71 with the exception of the initial void volume fraction which was randomly seeded at the integration point level in the range $4 \times 10^{-3} \leq f_0 \leq 8 \times 10^{-3}$ to account for the inhomogeneity of real materials.

The Young's modulus of the fibers and particles was set to E=450 GPa and the Poisson ratio to ν=0.17; these values were kept for all simulations of this chapter.

The modified Ludwik hardening law presented in eqn. (2.26) on page 27 was used to describe the flow stress σ_f of the matrix as a function of plastic strain. The necessary material parameters are given in tab. 2.1 on page 28.

Simulations of two-inclusion and multi-inclusion unit cells are presented in the following, which were performed in 2D (the reinforcement being fibers) and in 3D, where the particulate reinforcements are modeled by spheres.

4.1 Fiber Reinforced Metal Matrix Composites (2D Models)

4.1.1 Two-fiber Unit Cells

Two periodic configurations of fibers embedded in a ductile matrix as illustrated in fig. 4.1 were studied to test the nonlocal damage models. The fiber volume fraction of both arrangements is $\xi = 0.14$, the characteristic length, $2L$, was set to 17.5% of the fiber diameter. Uniaxial tensile loading in the vertical direction was simulated and periodicity boundary conditions were used in both cases.

The overall load–displacement responses displayed in fig. 4.2 show very different predictions obtained with the three ductile damage models as expected according to the observations in the single element tests in section 3.5. The DDIT model gives rise to the least ductile behavior, whereas the GTN model leads to the highest maximum loads and, in the case of the staggered arrangement, a very ductile response. The Rousselier model provides predictions between the above extremes. All three models, however, lead to the same conclusions regarding the behavior of the staggered and the stacked fiber arrangements. The unit cell with the stacked fiber configuration consistently shows a higher tangential stiffness at the beginning of the loading history, whereas the unit cell reinforced by staggered fibers can carry a higher maximum load and has a higher failure strain.

Finally, fig. 4.3 displays the deformed unit cells obtained with the nonlocal Rousselier model for the two arrangements. It is worth noting that the process zone is formed by two rows of finite elements as a consequence of the nonlocal approach and the chosen characteristic length.

Slightly non-symmetric results are obtained with the stacked fiber model due to the inhomogeneous distribution of the initial void volume fraction f_0 at the beginning of the analysis.

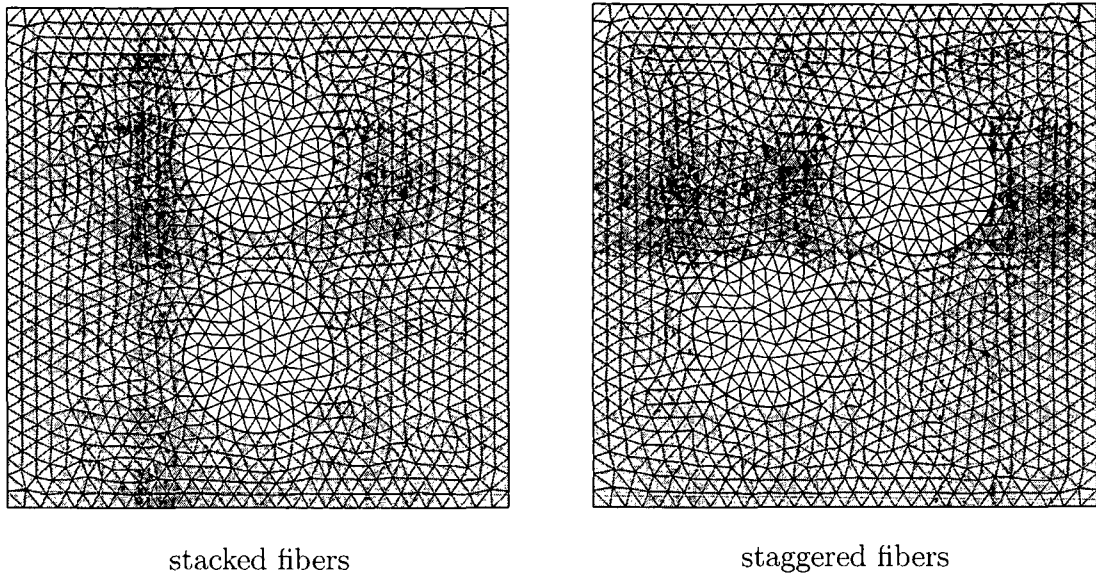stacked fibers   staggered fibers
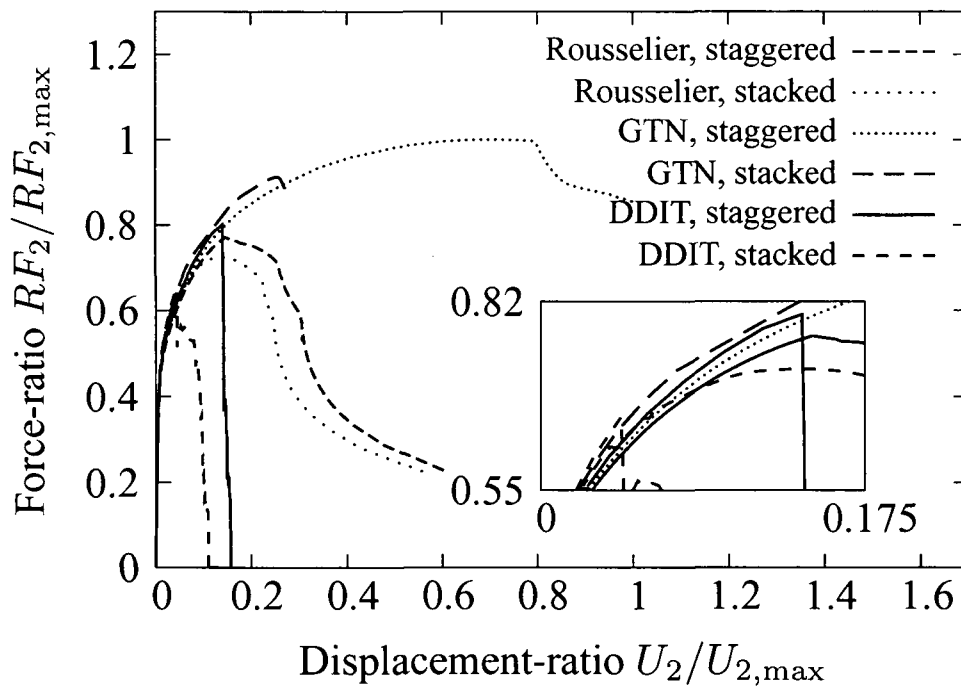
Figure 4.1: Undeformed meshes

Figure 4.2: Predicted force–displacement responses of two unit cells containing two fibers each (the insert shows details of the curves)

stacked fibers   staggered fibers
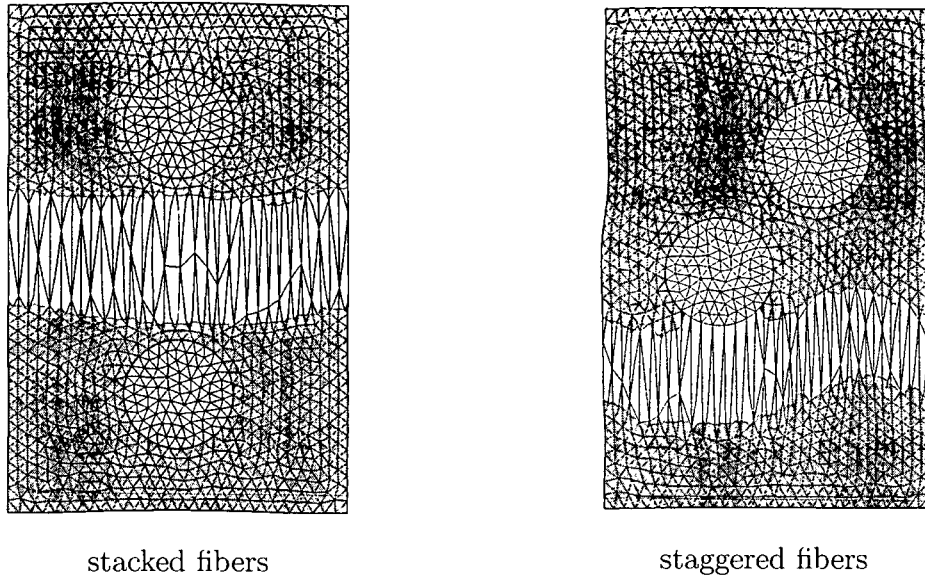
Figure 4.3: Deformed meshes

4.1.2   Multi-fiber Unit Cells

Further simulations were realized in order to show the applicability of the presented ductile
damage models to multi-fiber micromechanical models for metal matrix composites. An
arrangement following Nakamura and Suresh [102] is used, in which 60 aligned fibers with a
volume fraction of 25% are randomly distributed in a ductile matrix. Periodicity boundary
conditions and a generalized plane strain formulation were used. Uniaxial tensile loading
was applied in a direction transverse to the fibers. The user defined field (USDFLD) version
of the nonlocal DDIT model (compare section 3.6) was used to describe the damage beha-
vior of the matrix, whereas the fibers were as treated linear elastic as done in all simulations
in this chapter. The characteristic length, $2L$, was set to 8.1% of the fiber diameter, which
corresponds to approximately double the standard element size h.

The crack paths (completely damaged finite elements are removed from the mesh) in a
loading state close to final failure of the composite are depicted in fig. 4.4. A sequence of
images that show the crack propagation through the matrix of the MMC in different load-
ing states is given in fig. 4.5. In most of the cases crack initiation occurs in finite elements
located at or close to the interface between matrix and fibers. Regions where neighboring
fibers approach closely can be seen to be susceptible to ductile damage. Furthermore, the
first failed integration points are not aligned with the fiber's center points and the loading

direction but are observed to be slightly offset laterally.

The effect of periodicity boundary conditions can be seen in fig. 4.6 where nine unit cells are shown together and the correct transition of the crack from one unit cell to the other can be observed.

The periodic crack pattern that is typical of unit cell analyses involving damage is clearly evident. Because such behavior is rarely if ever found in actual composites, embedded cell models which can handle single cracks, are much better suited for studying the progress of damage, see e.g. Böhm [5]. Despite this idealization, however, the analysis serves as a clear proof of the applicability of nonlocal ductile damage models to fiber reinforced composites. The force–displacement response of the multi–fiber unit cell is shown in fig. 4.7.
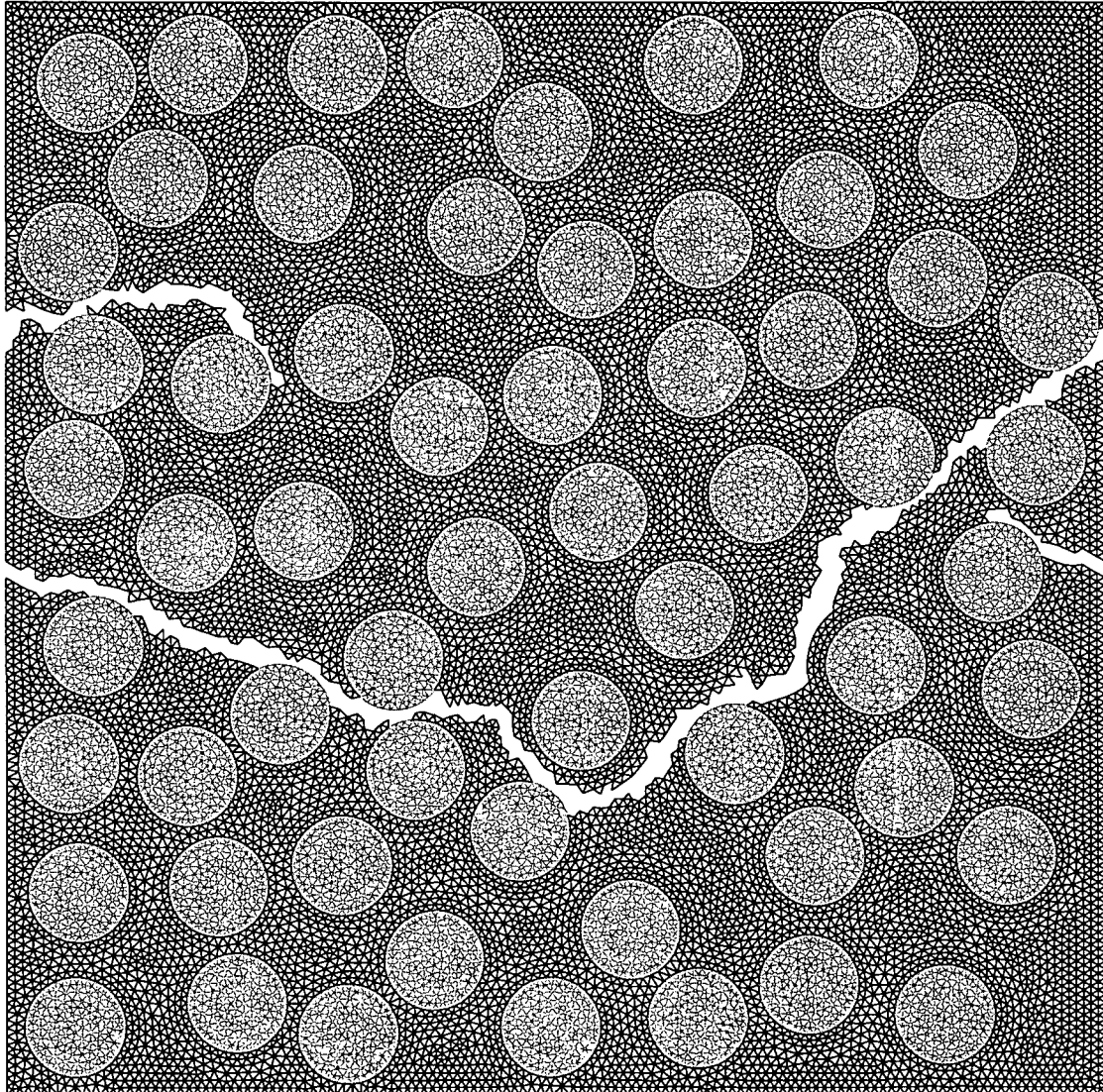
Figure 4.4: Crack propagation in a loading state close to final failure of a multi-fiber unit cell representing a unidirectional metal matrix composite subjected to uniaxial transverse loading in the vertical direction (finite elements in black represent the matrix, the fibers are rendered in gray)
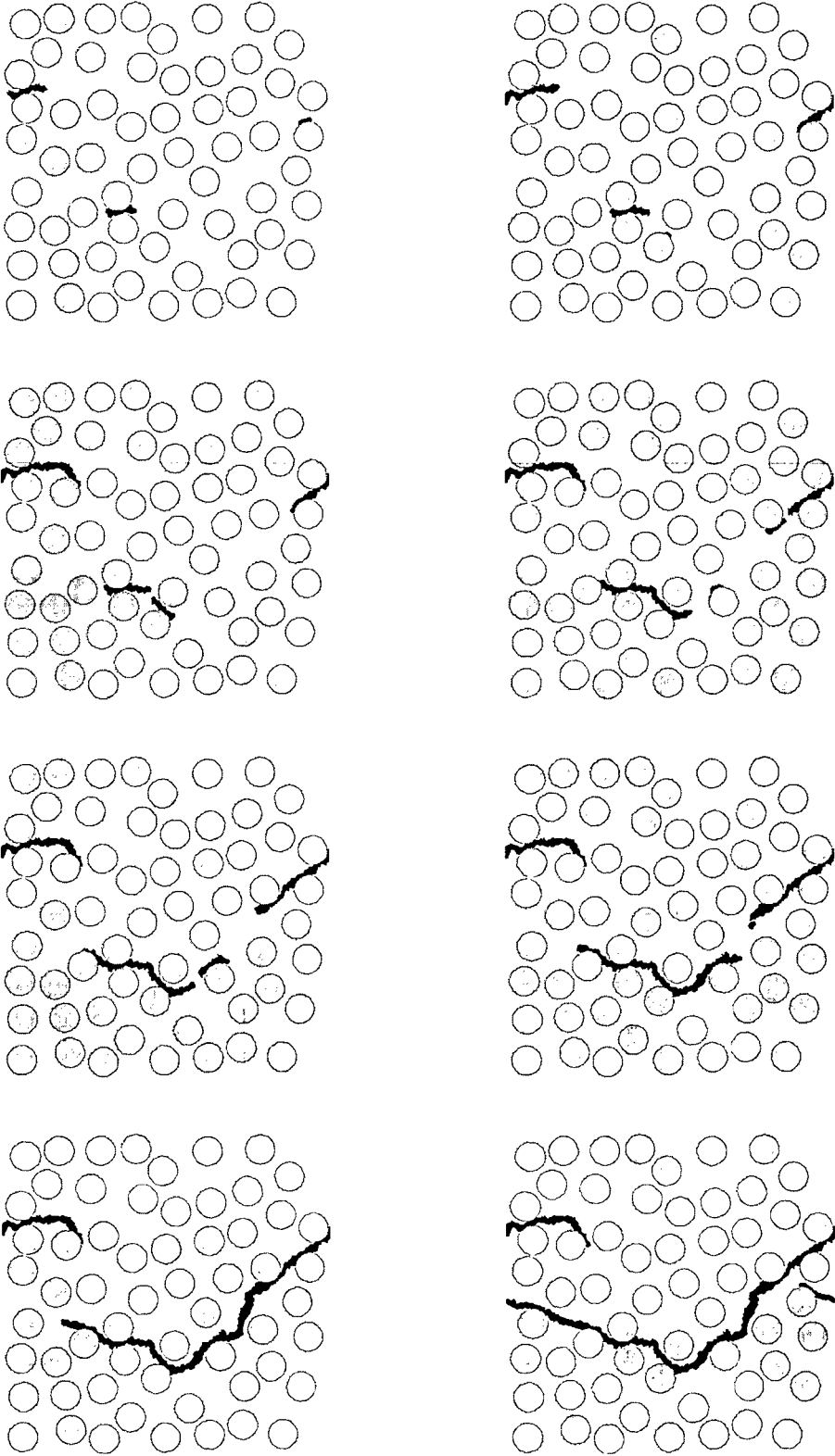
Figure 4.5: Crack propagation in a unidirectional fiber reinforced metal matrix composite subjected to transverse uniaxial loading at different loading states (the finite elements in black represent the damaged matrix material, the fibers are rendered in gray)
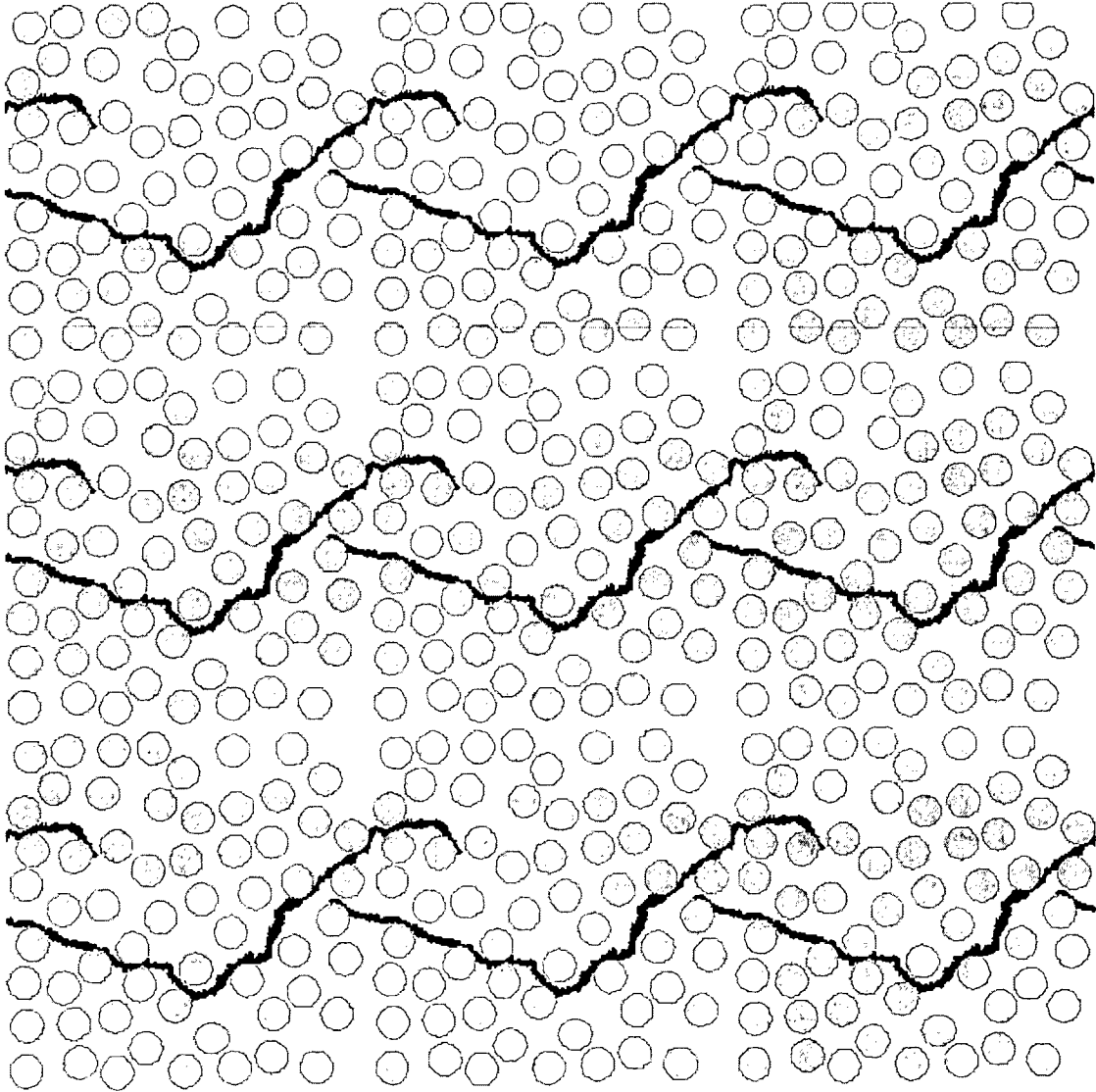
Figure 4.6: Nine unit cells showing the periodicity of the crack in a loading state close to
final failure of a unidirectional fiber reinforced metal matrix composite (the finite elements
in black represent the damaged matrix material, the fibers are rendered in gray)
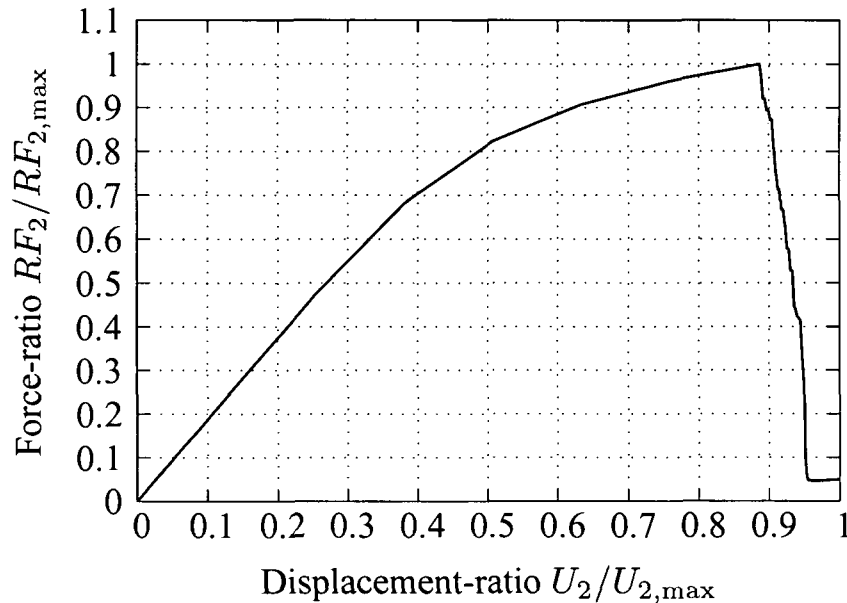
Figure 4.7: Force–displacement response of the fiber reinforced metal matrix composite under transverse unidirectional loading

4.2 Particle Reinforced Metal Matrix Composites (3D Models)

A number of applications of DDIT-type approaches and of the GTN ductile rupture model to micromechanical studies of composite materials have been reported in the literature, see e.g. LLorca et al. [103], Wulf et al. [26], Geni and Kikuchi [104], Mishnaevsky et al. [105], Segurado [106], all of which, however, employed local versions of the ductile damage models. Micromechanical studies of ductile matrix composites involving nonlocal ductile damage descriptions at the constituent level are a recent development, see Drabek and Böhm [107], Böhm et al. [108], Hu et al. [109], Drabek and Böhm [110], which is somewhat surprising because the high spatial resolutions of the stress and strain fields obtained on the micro-scale are well matched with the requirements of nonlocal smoothing.

Results based on three-dimensional unit cells are presented, which pertain to the behavior of composites reinforced by equiaxed particles. Periodicity boundary conditions were employed in all cases and all presented predictions were obtained with the nonlocal extended Rousselier model (#5).

4.2.1   Two-particle Unit Cells

Arrangement Effects

Two three-dimensional unit cells containing spherical particles in aligned and staggered periodic configurations that may be viewed as being analogous to the stacked and staggered arrangements used in subsection 4.1.1 are displayed in fig. 4.8. Uniaxial tensile loading in the vertical direction was applied in both cases.

Figure 4.9 shows the failed regions of the three-dimensional unit cells containing two spherical particles in the undeformed state. In fig. 4.10, which presents the corresponding load–displacement curves, the aligned sphere configuration can be seen to give a more compliant response in the elastic range, to reach a lower maximum stress and to be considerably more ductile than the staggered arrangement of the spheres.

A comparison with the force–displacement diagrams obtained for the two dimensional unit cells of the same volume fraction, fig. 4.2, shows major differences. Whereas in the 3D cell the aligned arrangements are predicted to be more ductile, for the 2D models the staggered arrangement shows a higher ductility for all damage models considered.

The qualitative differences in the responses predicted for these two sets of simple phase arrangements indicate that the use of two-dimensional microgeometries for modeling particle reinforced materials (which is known to be problematic in the elastic and, especially, the elastoplastic regimes, see Weissenbek et al. [111] and Böhm and Han [112]) should be avoided as far as possible in analyses involving ductile matrix damage in composites.

aligned particle arrangement   staggered particle arrangement
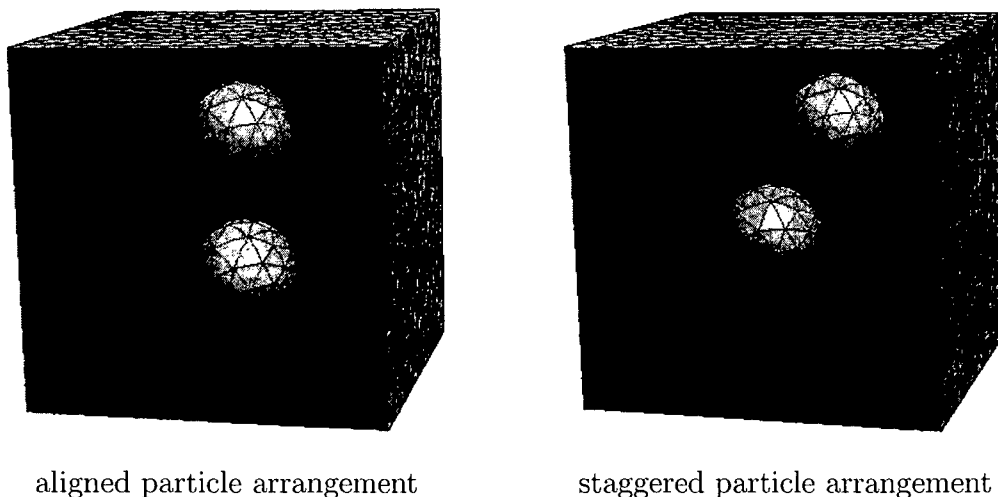
Figure 4.8: Undeformed meshes of three-dimensional two-particle unit cells

aligned particle arrangement   staggered particle arrangement
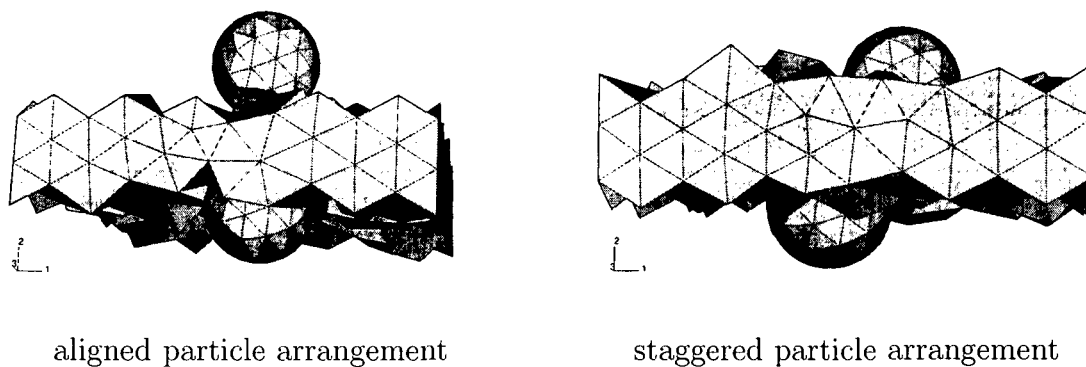
Figure 4.9: Completely damaged elements predicted with the nonlocal Rousselier model
by three-dimensional two-particle models (undeformed geometries)
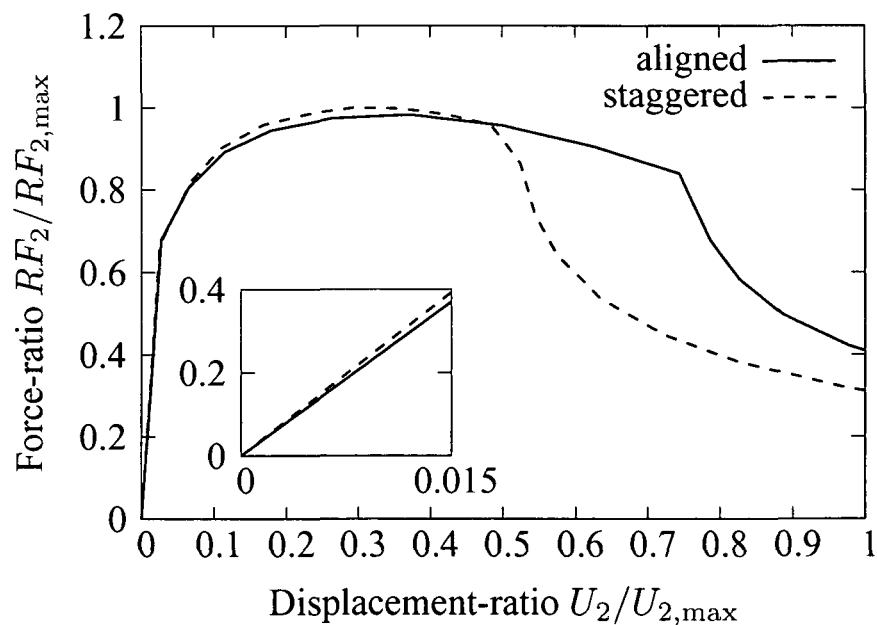

Figure 4.10: Force–displacement responses from the three-dimensional two–sphere simulations (the insert shows details of the curves in the elastic range)

Mesh Dependence

In order to show the effect of the nonlocal averaging algorithm on the mesh dependence of the results, two additional finite element meshes with different mesh size were generated for the aligned particle arrangement. The same loading scenario was applied to these meshes as described above and the characteristic length, $2L = 17.5\%$ of the particle diameter, is held constant in all three cases. The average element sizes, h, of the three models are 0.1, 0.075 and 0.062 times the unit cell length which results in meshes with ≈ 6.600, ≈ 10.400 and ≈ 22.900 elements, respectively.

All three meshes are depicted in fig. 4.11, where only the surface mesh of the continuum finite elements representing the matrix of the composite is shown in order to picture the arrangement of the particles. Figure 4.12 gives the force–displacement response of all three meshes with the same micro topology and turns out nearly the same results in regimes of positive and negative tangential stiffness. Especially the same value of the maximum loading capacity, $RF_{2,\mathrm{max}}$, is calculated in all three cases and the initiation of the rapid stress drop at high deformation differs only to a minor degree.

This test clearly indicates that the implemented nonlocal damage models can closely approach the stated requirement of markedly reducing or removing the mesh dependence in micromechanical studies of ductile matrix composites.

At this point it is appropriate to consider the additional memory requirements that are due to the use of a list of "neighbor data" (storing the spatial relation between the integration points) that is held in memory in the present implementation. For the meshes shown in fig. 4.11 additional RAM (random access memory) or swap space required for saving the neighbor data list is 26 MByte, 65 MByte and 340 MByte for the models with ≈ 6.600, ≈ 10.400 and ≈ 22.900 finite elements (four integration points per element), respectively. A further reduction of the mesh size, say to half that used in the coarsest mesh in the comparison, would give rise to ≈ 48.200 finite elements and a neighbor data list that needs approximately 2 GByte RAM (which exceeds requirements for the coarsest mesh by a factor of more than 70) when the characteristic length, $2L$, is kept at the same value.

Evidently, especially in 3D analyses the size of the neighbor data array grows quickly as the element sizes decreases relatively to the averaging radius L. This is not surprising because the number of integration points in the ductile phase is proportional to $\left(\frac{1}{h}\right)^3$ and the number of neighbors per integration point scales with $\left(\frac{L}{h}\right)^3$, so that the number of entries grows with $\frac{L^3}{h^6}$, i.e. proportionally to the square of the number of elements. In 2D analyses the number of entries also scales as the square of the elements, but the latter is proportional to $\left(\frac{1}{h}\right)^2$. Accordingly, with the present implementation the use of the elements that are

much smaller than the characteristic length, $2L$, quickly becomes inefficient. These scaling properties are purely geometrical and cannot circumvented by algorithmic improvements.

≈ 6.600 el. ≈ 10.400 el.

≈ 22.900 el.
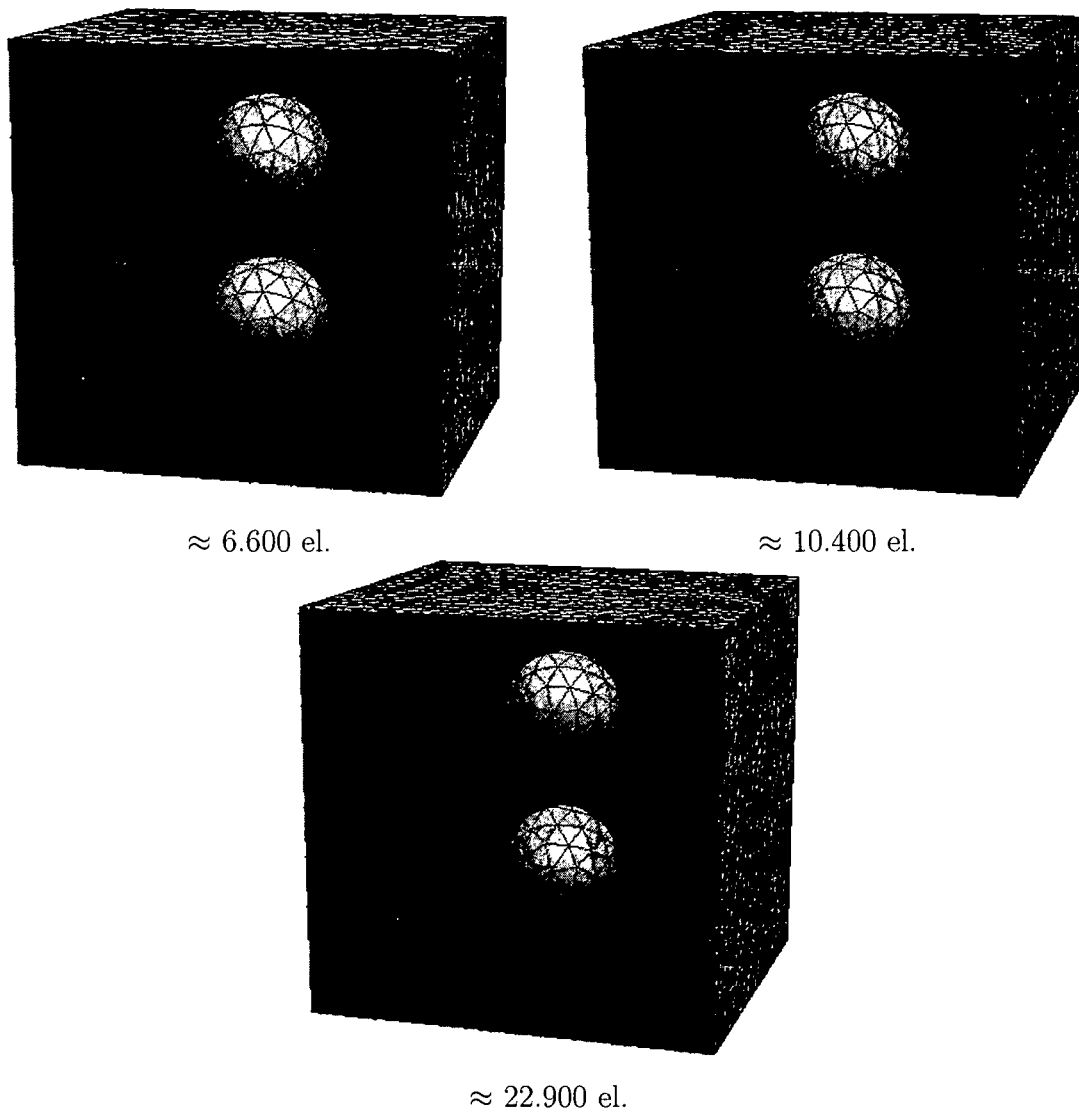
Figure 4.11: Undeformed meshes of two-particle unit cells (aligned particle configuration) with different mesh size h
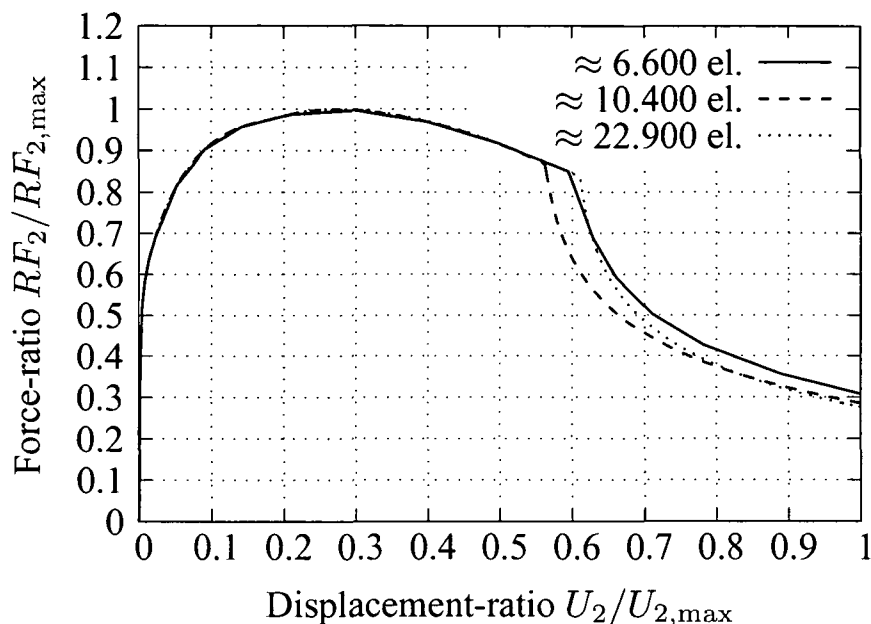
Figure 4.12: Force–displacement responses from two–sphere simulations performed with three different finite element meshes and constant characteristic length, $2L$

4.2.2 Multi-particle Unit Cells

At present one of the most powerful methods for simulating the thermomechanical behavior of particle reinforced composites are multi-particle unit cell models, see e.g. Gusev [113], Böhm and Han [112], Segurado [106], in which periodic homogenization is carried out on volume elements that contain a number of particles that are positioned according to the relevant arrangement statistics.

In this light, exploratory studies of ductile matrix damage in particle reinforced metal matrix composites were carried out by combining multi-particle unit cells with the nonlocal extended Rousselier ductile damage model (#5).

It should be noted that the responses obtained from these simulations are not directly comparable with experimental results on SiC/Al2618–T4 because particle fracture, which plays an important role in initiating damage in this composite system if the particles are rather aged, see LLorca and González [114], is not accounted for in the models.

The choice of proper reference volume elements (RVEs) that are statistically representative of actual composites in the presence of damage is an unsolved problem at present. It is clear, however, that periodic homogenization must always give rise to periodically

repeating patterns of damage and, accordingly, is not suitable for handling the emergence of macrocracks. The interpretation of the results obtained from periodic models involving damage, accordingly, may be difficult because effects of damage and approximations in terms of the phase arrangement can be closely intertwined.

Such behavior is evident in the responses of a set of three microgeometries, each containing 5, 10 and 20 spherical particles of equal size, respectively, at a total reinforcement volume fraction of 20%. The undeformed meshes of the corresponding unit cells are shown in fig. 4.13 and the predicted force–displacement responses under uniaxial tensile loading are presented in fig. 4.14. For overall displacements up to $U_2 = 0.4U_{2,\text{max}}$ the cell with 5 particles gives the softest and that with 20 particles gives the stiffest response, which is most probably an artefact of the low number of particles used in the cells. In the softening regime the trend reverses, which may be a size effect.

Unit cells that are too small for being proper RVEs tend to give rise to an anisotropic overall behavior and the responses of different "sub-RVE" cells that contain equal numbers of particles typically differ significantly. Such effects can be seen by comparing the overall responses of a second set of three periodic microgeometries. Figure 4.15 shows the three unit cells, each of which contains 5 spherical particles of equal size, the total particle volume fraction being 20%. The corresponding predicted macroscopic force–displacement responses are displayed in fig. 4.16 and can be seen to differ considerably in terms of their hardening behavior, of the maximum load carried, and of the softening behavior due to ductile matrix damage. Improved predictions can be obtained by ensemble averaging over results obtained from a number of different but equivalent microgeometries.

A third group of phase arrangements containing 10 spherical particles each are depicted in fig. 4.17. The three unit cells shown use identical positions of the particle centers and the particle radii are adjusted to obtain total particle volume fractions of 5.3%, 11.1%, and 20%, respectively. The corresponding predicted force–displacement curves for uniaxial tensile loading are presented in fig. 4.18. They show that among the reinforcement volume fractions studied the highest one gives rise to the highest elastic stiffness, the strongest strain hardening in the elastoplastic range and the highest maximum stress, the latter being reached at the lowest strain. The opposite tendencies are predicted for the lowest volume fraction in the series. These results are in qualitative agreement with experimental trends, viz. that increases in the particle volume fraction of MMCs lead to improved stiffness and strength but to reduced ductility. Additional simulation runs with other microgeometries are, however, needed to bolster the statistical significance of these results.

Finally, it is worth noting that all of the above simulations involving three-dimensional arrangements of spherical particles consistently predicted that, in the absence of other mi-

croscopic damage modes, ductile matrix damage occurs in the immediate neighborhood of the particles in regions that are situated in the direction of the global load with respect to the particles, see the contour plot of the void volume fraction in fig. 4.19, where the black regions indicate the maximum value, and fig. 4.20, which shows the completely damaged finite elements rendered in dark gray located at the poles of the particles. The author wants to point out that the periodicity of the unit cells considered in the implemented nonlocal averaging algorithm as discussed in section 3.4 can be observed in fig. 4.20 quite well by looking at the damaged elements at the boundaries.

The resulting regions of local ductile damage showed little tendency to coalesce at reasonable macroscopic loads, giving rise to a very ductile homogenized behavior. A considerably less ductile overall response can be expected to arise when damage due to particle fracture is taken into account.
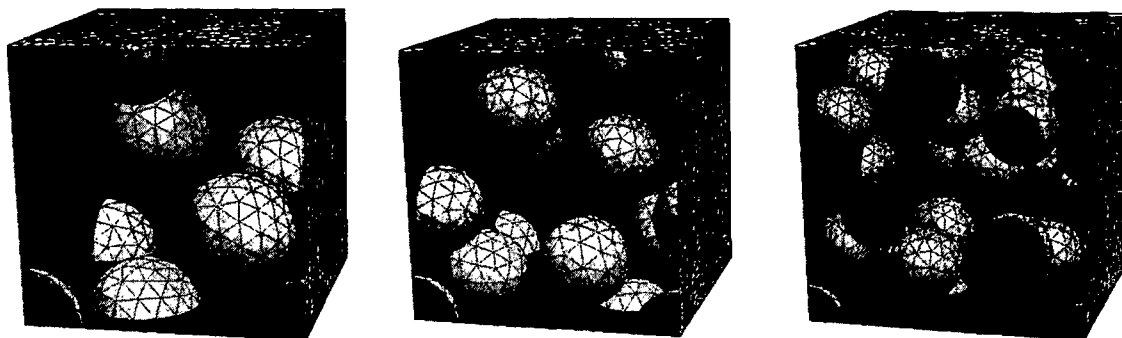
Figure 4.13: Undeformed meshes of unit cells containing 5 (left), 10 (center) and 20 (right) particles, respectively, at a particle volume fraction of 20%
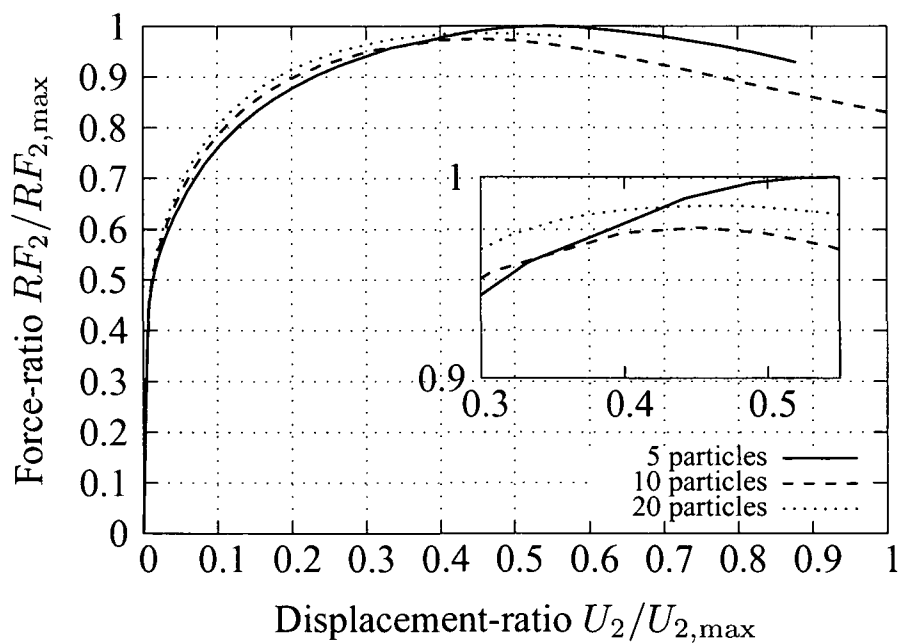
Figure 4.14: Force–displacement relations predicted for the three unit cells shown in fig. 4.13 under macroscopic uniaxial tensile loading
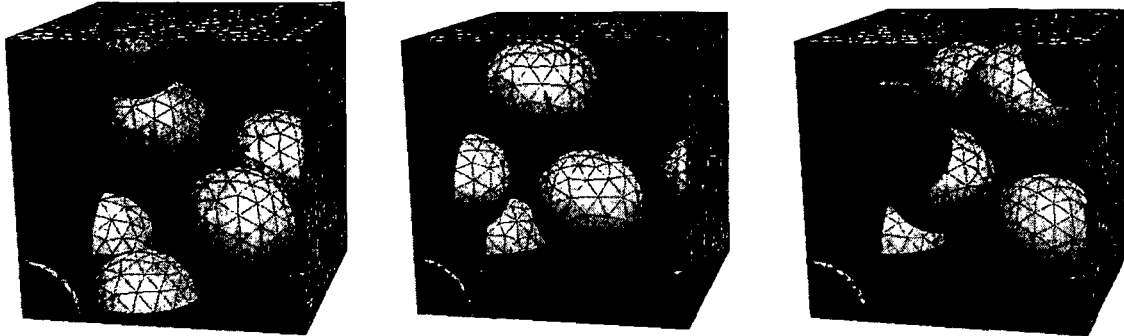
Figure 4.15: Undeformed meshes of three unit cells containing 5 particles each at a volume
fraction of 20% (the left unit cell was used in the previous simulation as well, see the left
model in fig. 4.13)
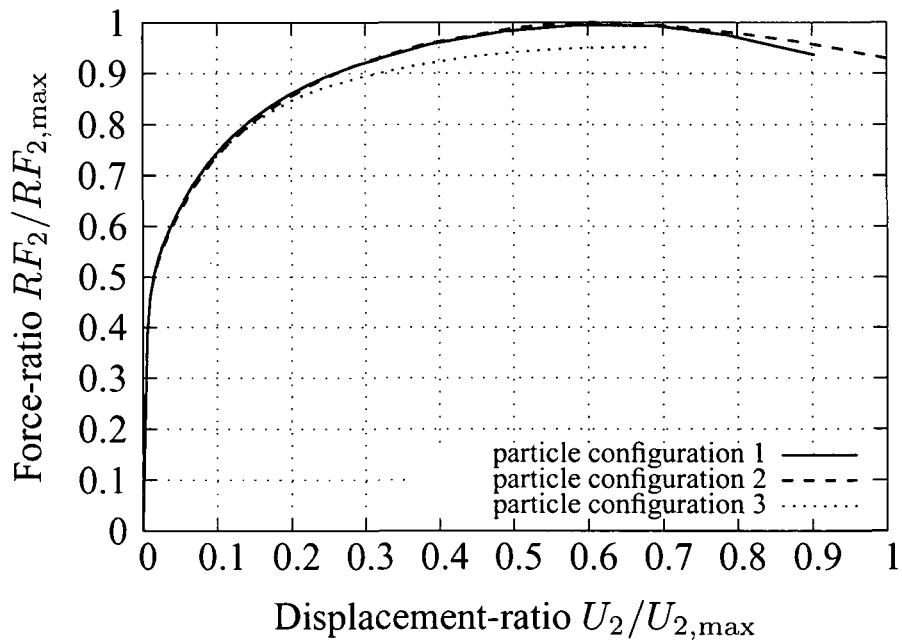
Figure 4.16: Force–displacement relations predicted for the three unit cells shown in
fig. 4.15 under macroscopic uniaxial tensile loading
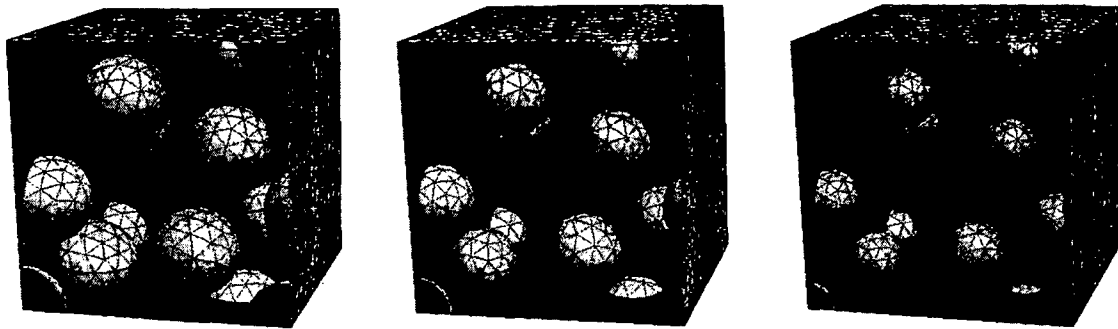
Figure 4.17: Undeformed meshes of three unit cells containing 10 particles each; particle positions are identical in the three cells and particle radii are chosen to obtain particle volume fractions of 20% (left), 11.1% (center), and 5.3% (right)
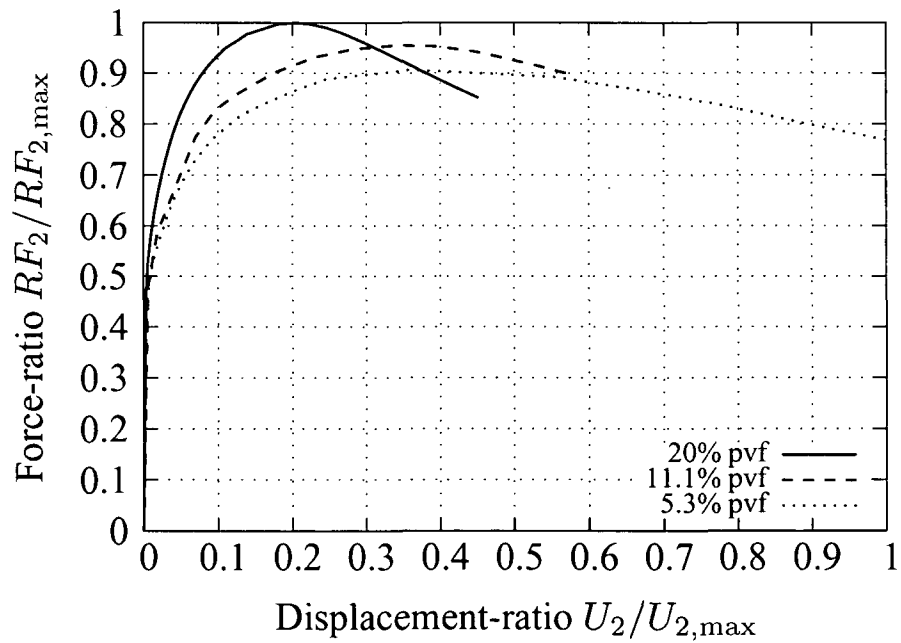
Figure 4.18: Force–displacement relations predicted for the three unit cells shown in fig. 4.17 under macroscopic uniaxial tensile loading
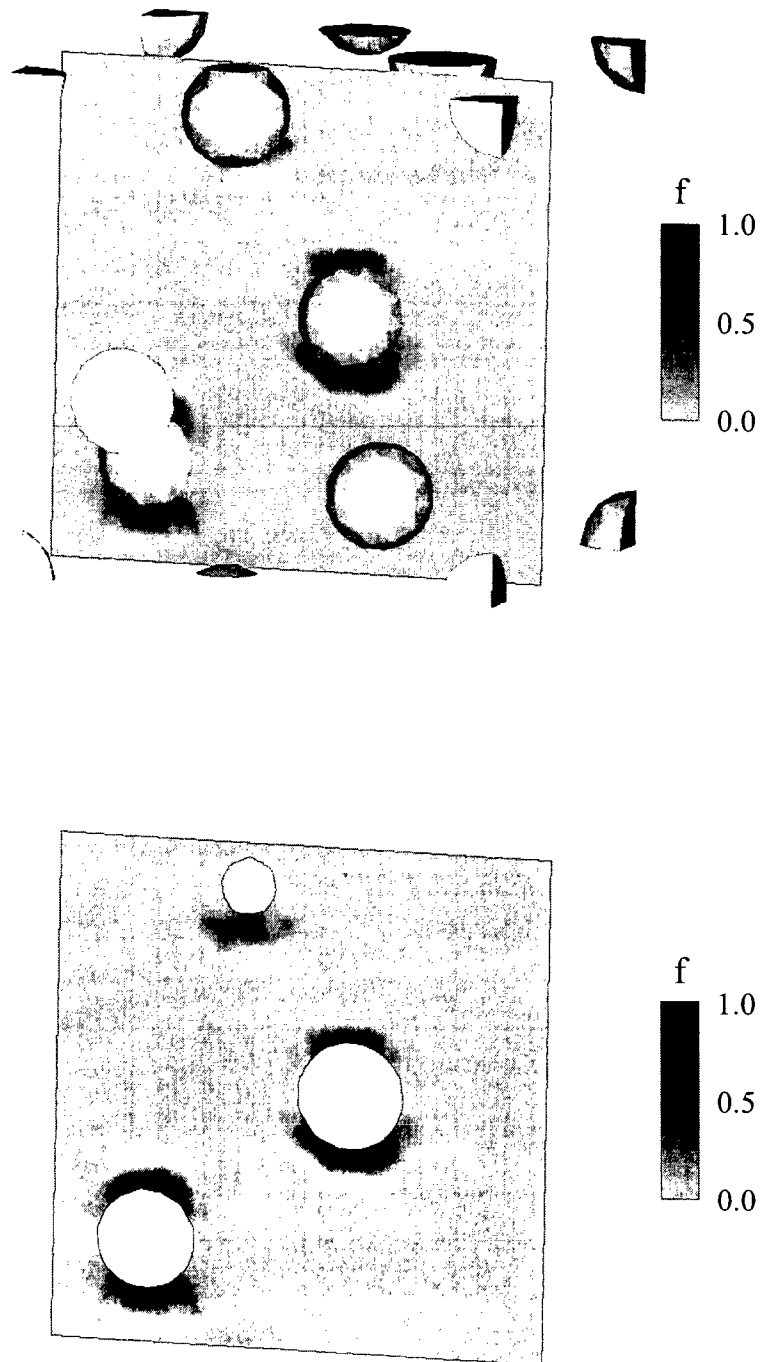
Figure 4.19: Contour plot of the void volume fraction, f, in a cross–section of the unit cell in the center of fig. 4.17 plotted with (top) and without (bottom) particles
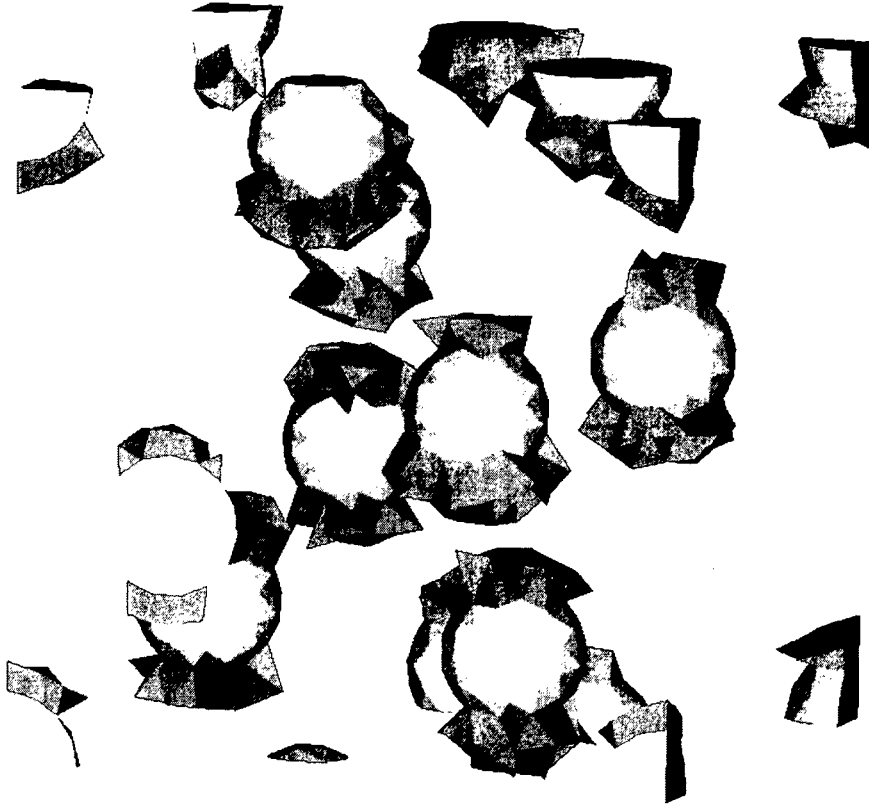
Figure 4.20: Completely damaged finite elements (rendered in dark gray) located at those poles of the particles that are aligned with the macroscopic load applied in the vertical direction (the different gray scales are caused by shading only)

Chapter 5

Summary

The present work concentrates on the modeling of ductile damage and failure of the matrix of composite materials and provides a building block for use in comprehensive models of the failure behavior of ductile matrix composites.

Following an introduction on metal matrix composites and the failure mechanisms acting in them at the microscale, a number of different damage models that are capable of describing crack initiation and crack propagation in ductile materials are presented in a literature survey. The work then concentrates on models of the continuum damage type, three of which were implemented into ABAQUS/Standard via user defined subroutines. The inherent mesh sensitivity of such models in the softening regime is accounted for by a regularization technique based on nonlocal averaging.

The full sets of equations for three ductile damage models, the Gurson-Tvergaard-Needleman and Rousselier ductile rupture models and an element elimination scheme triggered by a ductile damage indicator, are given and the pertinent algorithms are presented in detail. The return mapping algorithms, which must be capable of handling pressure-dependent yielding behavior in two of the models used, and the evaluation of the material Jacobian are discussed in depth. It is found that the use of Jacobians that are not consistent not only gives rise to slow convergence, but can actually lead to incorrect results in the softening regime.

The Rousselier damage model is modified by the author to handle purely hydrostatic stress states which is not possible in its basic form due the vertex of the yield surface.

Furthermore, a detailed description of the strategy for implementing the integral-type nonlocal algorithm into the ABAQUS user subroutines is given.

A number of single element tests are performed to compare the different models in order

to identify appropriate fields of application for them.

In the final part of the thesis the algorithms are applied to studying matrix damage in continuously and particle reinforced metal matrix composites. Qualitative differences in the predictions from 2D and 3D models are found, which shows that 2D descriptions are not a proper tool for studying ductile damage in particle reinforced composites. The implemented algorithm, on the one hand, introduces an absolute length scale into micromechanical models and, on the other hand, is shown to be capable of reproducing the influence of the particle volume fraction on the macroscopic stiffness, strength and ductility typically found in MMCs.

Future work is planned to consider combinations of the different failure modes of metal matrix composites, viz. ductile failure of the matrix, brittle fracture of the reinforcements, and interfacial decohesion. The ultimate aim of such models is to understand the failure behavior of MMCs at a depth that is sufficient for supporting the design of microstructures towards specified goals in terms of the overall behavior.

Appendix A

Some Auxiliary Expressions Required for Linking Integral and Gradient Type Nonlocal Models

The following relations are required for obtaining the gradient relationship, eqn. (2.33), from the Taylor expansion of the damage variable, eqn. (2.32):

$$\int_{-\infty}^{\infty}\int_{-\infty}^{\infty}\int_{-\infty}^{\infty} y_1 \frac{1}{(2\pi)^{3/2}L^3} \exp\left[-\frac{z^2(\mathbf{x},\mathbf{y})}{2L^2}\right] dy_1\,dy_2\,dy_3 = 0 \tag{A.1}$$

$$\int_{-\infty}^{\infty}\int_{-\infty}^{\infty}\int_{-\infty}^{\infty} \frac{1}{2!}y_1^2 \frac{1}{(2\pi)^{3/2}L^3} \exp\left[-\frac{z^2(\mathbf{x},\mathbf{y})}{2L^2}\right] dy_1\,dy_2\,dy_3 = \frac{1}{2}L^2 \tag{A.2}$$

$$\int_{-\infty}^{\infty}\int_{-\infty}^{\infty}\int_{-\infty}^{\infty} \frac{1}{2!}y_1 y_2 \frac{1}{(2\pi)^{3/2}L^3} \exp\left[-\frac{z^2(\mathbf{x},\mathbf{y})}{2L^2}\right] dy_1\,dy_2\,dy_3 = 0 \tag{A.3}$$

$$\int_{-\infty}^{\infty}\int_{-\infty}^{\infty}\int_{-\infty}^{\infty} \frac{1}{3!}y_1^3 \frac{1}{(2\pi)^{3/2}L^3} \exp\left[-\frac{z^2(\mathbf{x},\mathbf{y})}{2L^2}\right] dy_1\,dy_2\,dy_3 = 0 \tag{A.4}$$

$$\int_{-\infty}^{\infty}\int_{-\infty}^{\infty}\int_{-\infty}^{\infty} \frac{1}{4!}y_1^4 \frac{1}{(2\pi)^{3/2}L^3} \exp\left[-\frac{z^2(\mathbf{x},\mathbf{y})}{2L^2}\right] dy_1\,dy_2\,dy_3 = \frac{1}{8}L^4 \tag{A.5}$$

Appendix B

Proof of the Relation $\mathbf{S} = 2G\boldsymbol{\varepsilon}_{\mathrm{D}}^{\mathrm{e}}$

The relation between the stress deviator $\mathbf{S}$ and the strain deviator $\boldsymbol{\varepsilon}_{\mathrm{D}}^{\mathrm{e}}$, eqn. (3.17), can be derived as follows:

$$\sigma_{ij} = \left[\left(K - \frac{2}{3}G\right)\delta_{ij}\delta_{kl} + 2G\delta_{ik}\delta_{jl}\right]\varepsilon_{kl}^{\mathrm{e}} \tag{B.1}$$

$$S_{ij} = \sigma_{ij} - \sigma_m\delta_{ij} = C_{ijkl}^{\mathrm{e}}\varepsilon_{\mathrm{D}_{kl}}^{\mathrm{e}} = C_{ijkl}^{\mathrm{e}}\left(\varepsilon_{kl}^{\mathrm{e}} - \frac{1}{3}\varepsilon_{\mathrm{V}}^{\mathrm{e}}\delta_{kl}\right) \tag{B.2}$$

$$= \left[\left(K - \frac{2}{3}G\right)\delta_{ij}\delta_{kl} + 2G\delta_{ik}\delta_{jl}\right]\left(\varepsilon_{kl}^{\mathrm{e}} - \frac{1}{3}\left(\varepsilon_{11}^{\mathrm{e}} + \varepsilon_{22}^{\mathrm{e}} + \varepsilon_{33}^{\mathrm{e}}\right)\delta_{kl}\right)$$

$$= 2G\left(\varepsilon_{ij}^{\mathrm{e}} - \frac{1}{3}\left(\varepsilon_{11}^{\mathrm{e}} + \varepsilon_{22}^{\mathrm{e}} + \varepsilon_{33}^{\mathrm{e}}\right)\delta_{ij}\right) = 2G\varepsilon_{\mathrm{D}_{ij}}^{\mathrm{e}}$$

For the 11-component of the stress deviator one accordingly obtains

$$S_{11} = C_{11kl}^{\mathrm{e}}\left(\varepsilon_{kl}^{\mathrm{e}} - \frac{1}{3}\varepsilon_{\mathrm{V}}^{\mathrm{e}}\delta_{kl}\right) \tag{B.3}$$

$$= \left[\left(K - \frac{2}{3}G\right)\delta_{kl} + 2G\delta_{1k}\delta_{1l}\right]\left(\varepsilon_{kl}^{\mathrm{e}} - \frac{1}{3}\left(\varepsilon_{11}^{\mathrm{e}} + \varepsilon_{22}^{\mathrm{e}} + \varepsilon_{33}^{\mathrm{e}}\right)\delta_{kl}\right)$$

$$= 2G\left(\varepsilon_{11}^{\mathrm{e}} - \frac{1}{3}\left(\varepsilon_{11}^{\mathrm{e}} + \varepsilon_{22}^{\mathrm{e}} + \varepsilon_{33}^{\mathrm{e}}\right)\right) + \left(K - \frac{2}{3}G\right)\left(\varepsilon_{11}^{\mathrm{e}} - \frac{1}{3}\left(\varepsilon_{11}^{\mathrm{e}} + \varepsilon_{22}^{\mathrm{e}} + \varepsilon_{33}^{\mathrm{e}}\right)\right)$$

$$+ \left(K - \frac{2}{3}G\right)\left(\varepsilon_{22}^{\mathrm{e}} - \frac{1}{3}\left(\varepsilon_{11}^{\mathrm{e}} + \varepsilon_{22}^{\mathrm{e}} + \varepsilon_{33}^{\mathrm{e}}\right)\right) + \left(K - \frac{2}{3}G\right)\left(\varepsilon_{33}^{\mathrm{e}} - \frac{1}{3}\left(\varepsilon_{11}^{\mathrm{e}} + \varepsilon_{22}^{\mathrm{e}} + \varepsilon_{33}^{\mathrm{e}}\right)\right)$$

$$= 2G\left(\varepsilon_{11}^{\mathrm{e}} - \frac{1}{3}\left(\varepsilon_{11}^{\mathrm{e}} + \varepsilon_{22}^{\mathrm{e}} + \varepsilon_{33}^{\mathrm{e}}\right)\right) = 2G\varepsilon_{\mathrm{D}_{11}}^{\mathrm{e}}$$

and the other components can be handled in analogy.

Appendix C

Derivation of the Tensor c_{ij} for $n = 2$

The tensor c_{ij} which is required for evaluating the consistent tangent tensor, see eqn. (3.66) to (3.75) can be derived for the case of 2 scalar state variables ($n = 2$) as follows. The relation

$$\partial H_i = \partial \Delta H_i, \tag{C.1}$$

the dependence of

$$\Delta H_i = \Delta H_i(\sigma_{\mathrm{m}}, \sigma_{\mathrm{eq}}, \Delta \varepsilon_p, \Delta \varepsilon_q, H_j) \qquad \text{for } i, j = 1, \ldots, n \tag{C.2}$$

and setting $n = 2$ lead to

$$
\begin{aligned}
\partial H_1 = \partial \Delta H_1 \quad = \quad & \frac{\partial \Delta H_1}{\partial \Delta \varepsilon_p} \partial \Delta \varepsilon_p + \frac{\partial \Delta H_1}{\partial \Delta \varepsilon_q} \partial \Delta \varepsilon_q \\
& + \left(\frac{\partial \Delta H_1}{\partial \sigma_{\mathrm{m}}} \frac{\partial \sigma_{\mathrm{m}}}{\partial \boldsymbol{\sigma}} + \frac{\partial \Delta H_1}{\partial \sigma_{\mathrm{eq}}} \frac{\partial \sigma_{\mathrm{eq}}}{\partial \boldsymbol{\sigma}} \right) : \partial \boldsymbol{\sigma} \\
& + \frac{\partial \Delta H_1}{\partial H_1} \partial H_1 + \frac{\partial \Delta H_1}{\partial H_2} \partial H_2,
\end{aligned}
\tag{C.3}
$$

$$
\begin{aligned}
\partial H_2 = \partial \Delta H_2 \quad = \quad & \frac{\partial \Delta H_2}{\partial \Delta \varepsilon_p} \partial \Delta \varepsilon_p + \frac{\partial \Delta H_2}{\partial \Delta \varepsilon_q} \partial \Delta \varepsilon_q \\
& + \left(\frac{\partial \Delta H_2}{\partial \sigma_{\mathrm{m}}} \frac{\partial \sigma_{\mathrm{m}}}{\partial \boldsymbol{\sigma}} + \frac{\partial \Delta H_2}{\partial \sigma_{\mathrm{eq}}} \frac{\partial \sigma_{\mathrm{eq}}}{\partial \boldsymbol{\sigma}} \right) : \partial \boldsymbol{\sigma} \\
& + \frac{\partial \Delta H_2}{\partial H_1} \partial H_1 + \frac{\partial \Delta H_2}{\partial H_2} \partial H_2.
\end{aligned}
\tag{C.4}
$$

Rearranging leads to

$$\partial H_1 \left(1 - \frac{\partial \Delta H_1}{\partial H_1}\right) = \frac{\partial \Delta H_1}{\partial \Delta \varepsilon_p} \partial \Delta \varepsilon_p + \frac{\partial \Delta H_1}{\partial \Delta \varepsilon_q} \partial \Delta \varepsilon_q \tag{C.5}$$

$$+ \left(\frac{\partial \Delta H_1}{\partial \sigma_m} \frac{\partial \sigma_m}{\partial \boldsymbol{\sigma}} + \frac{\partial \Delta H_1}{\partial \sigma_{eq}} \frac{\partial \sigma_{eq}}{\partial \boldsymbol{\sigma}}\right) : \partial \boldsymbol{\sigma} + \frac{\partial \Delta H_1}{\partial H_2} \partial H_2,$$

$$\partial H_2 \left(1 - \frac{\partial \Delta H_2}{\partial H_2}\right) = \frac{\partial \Delta H_2}{\partial \Delta \varepsilon_p} \partial \Delta \varepsilon_p + \frac{\partial \Delta H_2}{\partial \Delta \varepsilon_q} \partial \Delta \varepsilon_q \tag{C.6}$$

$$+ \left(\frac{\partial \Delta H_2}{\partial \sigma_m} \frac{\partial \sigma_m}{\partial \boldsymbol{\sigma}} + \frac{\partial \Delta H_2}{\partial \sigma_{eq}} \frac{\partial \sigma_{eq}}{\partial \boldsymbol{\sigma}}\right) : \partial \boldsymbol{\sigma} + \frac{\partial \Delta H_2}{\partial H_1} \partial H_1,$$

and moving the unknowns ∂H_1 and ∂H_2 to the left hand side gives

$$\left(1 - \frac{\partial \Delta H_1}{\partial H_1}\right) \partial H_1 - \frac{\partial \Delta H_1}{\partial H_2} \partial H_2 = \tag{C.7}$$

$$= \frac{\partial \Delta H_1}{\partial \Delta \varepsilon_p} \partial \Delta \varepsilon_p + \frac{\partial \Delta H_1}{\partial \Delta \varepsilon_q} \partial \Delta \varepsilon_q + \left(\frac{\partial \Delta H_1}{\partial \sigma_m} \frac{\partial \sigma_m}{\partial \boldsymbol{\sigma}} + \frac{\partial \Delta H_1}{\partial \sigma_{eq}} \frac{\partial \sigma_{eq}}{\partial \boldsymbol{\sigma}}\right) : \partial \boldsymbol{\sigma} = < Q_1 >,$$

$$-\frac{\partial \Delta H_2}{\partial H_1} \partial H_1 + \left(1 - \frac{\partial \Delta H_2}{\partial H_2}\right) \partial H_2 = \tag{C.8}$$

$$= \frac{\partial \Delta H_2}{\partial \Delta \varepsilon_p} \partial \Delta \varepsilon_p + \frac{\partial \Delta H_2}{\partial \Delta \varepsilon_q} \partial \Delta \varepsilon_q + \left(\frac{\partial \Delta H_2}{\partial \sigma_m} \frac{\partial \sigma_m}{\partial \boldsymbol{\sigma}} + \frac{\partial \Delta H_2}{\partial \sigma_{eq}} \frac{\partial \sigma_{eq}}{\partial \boldsymbol{\sigma}}\right) : \partial \boldsymbol{\sigma} = < Q_2 >,$$

or, in an abbreviated form

$$\left(1 - \frac{\partial \Delta H_1}{\partial H_1}\right) \partial H_1 - \frac{\partial \Delta H_1}{\partial H_2} \partial H_2 = < Q_1 >, \tag{C.9}$$

$$-\frac{\partial \Delta H_2}{\partial H_1} \partial H_1 + \left(1 - \frac{\partial \Delta H_2}{\partial H_2}\right) \partial H_2 = < Q_2 >. \tag{C.10}$$

The unknowns ∂H_1 and ∂H_2 can now be calculated as

$$\begin{pmatrix} \partial H_1 \\ \partial H_2 \end{pmatrix} = \mathbf{c} \begin{pmatrix} < Q_1 > \\ < Q_2 > \end{pmatrix}, \tag{C.11}$$

where $\mathbf{c}$ is the inverse of the tensor $\hat{\mathbf{c}}$ with the components

$$\hat{c}_{ij} = \delta_{ij} - \frac{\partial \Delta H_i}{\partial H_j}. \tag{C.12}$$

Appendix D

Expressions that are Used in Evaluating a Consistent Tangent for the GTN Model

An expression for the consistent tangent of the GTN model (compare tab. 3.3) can be derived as follows.

Derivatives of the GTN yield function and flow potential, $\Phi = g = \frac{\sigma_{eq}^2}{\sigma_f^2} + 2q_1 f \cosh\left(\frac{3q_2 \sigma_m}{2\sigma_f}\right) - 1 - q_3 f^2 = 0$, with respect to various variables take the form

$$\frac{\partial \Phi}{\partial \sigma_{eq}} = \frac{\partial g}{\partial \sigma_{eq}} = \frac{2 \sigma_{eq}}{\sigma_f{}^2}, \tag{D.1}$$

$$\frac{\partial \Phi}{\partial \sigma_m} = \frac{\partial g}{\partial \sigma_m} = \frac{3 f \ q_1 \ q_2 \ \sinh(\frac{3}{2} \frac{q_2}{\sigma_f} \frac{\sigma_m}{})}{\sigma_f}, \tag{D.2}$$

$$\frac{\partial \Phi}{\partial f} = -2 f \ q_3 + 2 \ q_1 \ \cosh(\frac{3 \ q_2 \ \sigma_m}{2 \ \sigma_f}), \tag{D.3}$$

$$\frac{\partial \Phi}{\partial \varepsilon_{eq}^{pl}} = \frac{\partial \Phi}{\partial \sigma_f} \frac{\partial \sigma_f}{\partial \varepsilon_{eq}^{pl}} = \frac{\partial \Phi}{\partial \sigma_f} \sigma_f' = \sigma_f' \left(\frac{-2 \ \sigma_{eq}{}^2}{\sigma_f{}^3} - \frac{3 f \ q_1 \ q_2 \ \sigma_m \ \sinh(\frac{3 \ q_2 \ \sigma_m}{2 \ \sigma_f})}{\sigma_f{}^2} \right), \tag{D.4}$$

$$\frac{\partial^2 g}{\partial \sigma_m^2} = \frac{9 f \ q_1 \ q_2{}^2 \ \cosh(\frac{3 \ q_2 \ \sigma_m}{2 \ \sigma_f})}{2 \ \sigma_f{}^2}, \tag{D.5}$$

$$\frac{\partial^2 g}{\partial \sigma_{\mathrm{eq}}^2} = \frac{2}{\sigma_{\mathrm{f}}^2}, \tag{D.6}$$

$$\frac{\partial^2 g}{\partial \sigma_{\mathrm{eq}} \partial \sigma_{\mathrm{m}}} = \frac{\partial^2 g}{\partial \sigma_{\mathrm{m}} \partial \sigma_{\mathrm{eq}}} = \frac{\partial^2 g}{\partial \sigma_{\mathrm{eq}} \partial f} = 0, \tag{D.7}$$

$$\frac{\partial^2 g}{\partial \sigma_{\mathrm{eq}} \partial \varepsilon_{\mathrm{eq}}^{\mathrm{pl}}} = \frac{\partial g}{\partial \sigma_{\mathrm{eq}}} \frac{\partial g}{\partial \sigma_{\mathrm{f}}} \frac{\partial \sigma_{\mathrm{f}}}{\partial \varepsilon_{\mathrm{eq}}^{\mathrm{pl}}} = \frac{\partial g}{\partial \sigma_{\mathrm{eq}}} \frac{\partial g}{\partial \sigma_{\mathrm{f}}} \sigma_{\mathrm{f}}' = \frac{-4 \; \sigma_{\mathrm{f}}' \; \sigma_{\mathrm{eq}}}{\sigma_{\mathrm{f}}^3}, \tag{D.8}$$

$$\frac{\partial^2 g}{\partial \sigma_{\mathrm{m}} \partial f} = \frac{3 \; q_1 \; q_2 \; \sinh\left(\frac{3}{2} \frac{q_2}{\sigma_{\mathrm{f}}} \sigma_{\mathrm{m}}\right)}{\sigma_{\mathrm{f}}}, \tag{D.9}$$

$$\frac{\partial^2 g}{\partial \sigma_{\mathrm{m}} \partial \varepsilon_{\mathrm{eq}}^{\mathrm{pl}}} = \frac{\partial g}{\partial \sigma_{\mathrm{m}}} \frac{\partial g}{\partial \sigma_{\mathrm{f}}} \frac{\partial \sigma_{\mathrm{f}}}{\partial \varepsilon_{\mathrm{eq}}^{\mathrm{pl}}} = \frac{\partial g}{\partial \sigma_{\mathrm{m}}} \frac{\partial g}{\partial \sigma_{\mathrm{f}}} \sigma_{\mathrm{f}}' = \tag{D.10}$$
$$\left(\frac{-9 \; f \; q_1 \; q_2^2 \; \sigma_{\mathrm{m}} \; \cosh\left(\frac{3}{2} \frac{q_2}{\sigma_{\mathrm{f}}} \sigma_{\mathrm{m}}\right)}{2 \; \sigma_{\mathrm{f}}^3} - \frac{3 \; f \; q_1 \; q_2 \; \sinh\left(\frac{3}{2} \frac{q_2}{\sigma_{\mathrm{f}}} \sigma_{\mathrm{m}}\right)}{\sigma_{\mathrm{f}}^2} \right) \sigma_{\mathrm{f}}'.$$

Derivatives of the increment of the void volume fraction, $\Delta f = \Delta H_1$, and of the equivalent plastic strain, $\Delta \varepsilon_{\mathrm{eq}}^{\mathrm{pl}} = \Delta H_2$, can be given as

$$\frac{\partial \Delta f}{\partial \Delta \varepsilon_{\mathrm{p}}} = 1 - f, \tag{D.11}$$

$$\frac{\partial \Delta f}{\partial \Delta \varepsilon_{\mathrm{q}}} = \frac{\partial \Delta f}{\partial \sigma_{\mathrm{m}}} = \frac{\partial \Delta f}{\partial \sigma_{\mathrm{eq}}} = \frac{\partial \Delta f}{\partial \varepsilon_{\mathrm{eq}}^{\mathrm{pl}}} = 0, \tag{D.12}$$

$$\frac{\partial \Delta f}{\partial f} = -\Delta \varepsilon_{\mathrm{p}}, \tag{D.13}$$

$$\frac{\partial \Delta \varepsilon_{\mathrm{eq}}^{\mathrm{pl}}}{\partial \Delta \varepsilon_{\mathrm{p}}} = \frac{\sigma_{\mathrm{m}}}{(1-f) \; \sigma_{\mathrm{f}}}, \tag{D.14}$$

$$\frac{\partial \Delta \varepsilon_{\mathrm{eq}}^{\mathrm{pl}}}{\partial \Delta \varepsilon_{\mathrm{q}}} = \frac{\sigma_{\mathrm{eq}}}{(1-f) \; \sigma_{\mathrm{f}}}, \tag{D.15}$$

$$\frac{\partial \Delta \varepsilon_{\mathrm{eq}}^{\mathrm{pl}}}{\partial \sigma_{\mathrm{m}}} = \frac{\Delta \varepsilon_{\mathrm{p}}}{(1-f) \; \sigma_{\mathrm{f}}}, \tag{D.16}$$

$$\frac{\partial \Delta \varepsilon_{\mathrm{eq}}^{\mathrm{pl}}}{\partial \sigma_{\mathrm{eq}}} = \frac{\Delta \varepsilon_{\mathrm{q}}}{(1 - f) \ \sigma_{\mathrm{f}}},$$

(D.17)

$$\frac{\partial \Delta \varepsilon_{\mathrm{eq}}^{\mathrm{pl}}}{\partial f} = \frac{\Delta \varepsilon_{\mathrm{q}} \ \sigma_{\mathrm{eq}} + \Delta \varepsilon_{\mathrm{p}} \ \sigma_{\mathrm{m}}}{(1 - f)^2 \ \sigma_{\mathrm{f}}},$$

(D.18)

$$\frac{\partial \Delta \varepsilon_{\mathrm{eq}}^{\mathrm{pl}}}{\partial \varepsilon_{\mathrm{eq}}^{\mathrm{pl}}} = \frac{\partial \Delta \varepsilon_{\mathrm{eq}}^{\mathrm{pl}}}{\partial \sigma_{\mathrm{f}}} \frac{\partial \sigma_{\mathrm{f}}}{\partial \varepsilon_{\mathrm{eq}}^{\mathrm{pl}}} = \frac{\partial \Delta \varepsilon_{\mathrm{eq}}^{\mathrm{pl}}}{\partial \sigma_{\mathrm{f}}} \sigma_{\mathrm{f}}' = - \left(\frac{\sigma_{\mathrm{f}}' \ (\ \Delta \varepsilon_{\mathrm{q}} \ \sigma_{\mathrm{eq}} + \Delta \varepsilon_{\mathrm{p}} \ \sigma_{\mathrm{m}})}{(1 - f) \ \sigma_{\mathrm{f}}^2} \right).$$

(D.19)

Appendix E

Expressions that are Used in Evaluating a Consistent Tangent for the extended Rousselier Model

An expression for the consistent tangent of the extended Rousselier model (see tab. 3.5) can be derived as follows.

Derivatives of the Rousselier yield function, $\Phi = \sigma_{eq} - \sigma_f + q_4 \sigma_f f \tilde{D} \exp\left(\frac{\sigma_m}{q_4 \sigma_f}\right) = 0$, and the flow potential, $g = \frac{\sigma_{eq}^2}{\sigma_{eq}^{*2}} + \frac{\sigma_m^2}{\sigma_m^{*2}} - 1$, with respect to various variables take the form

$$\frac{\partial \Phi}{\partial \sigma_{eq}} = 1, \tag{E.1}$$

$$\frac{\partial \Phi}{\partial \sigma_m} = \tilde{D} f \exp\left(\frac{\sigma_m}{q_4 \sigma_f}\right), \tag{E.2}$$

$$\frac{\partial \Phi}{\partial f} = \tilde{D} q_4 \sigma_f \exp\left(\frac{\sigma_m}{q_4 \sigma_f}\right), \tag{E.3}$$

$$\frac{\partial \Phi}{\partial \varepsilon_{eq}^{pl}} = \frac{\partial \Phi}{\partial \sigma_f} \frac{\partial \sigma_f}{\partial \varepsilon_{eq}^{pl}} = \frac{\partial \Phi}{\partial \sigma_f} \sigma_f' = \left(\tilde{D} f q_4 \exp\left(\frac{\sigma_m}{q_4 \sigma_f}\right) - \frac{\tilde{D} f \sigma_m \exp\left(\frac{\sigma_m}{q_4 \sigma_f}\right)}{\sigma_f}\right) \sigma_f', \tag{E.4}$$

$$\frac{\partial g}{\partial \sigma_{eq}} = \frac{2\sigma_{eq}}{\sigma_{eq}^{*2}}, \tag{E.5}$$

111

$$\frac{\partial g}{\partial \sigma_{\mathrm{m}}} = \frac{2\sigma_{\mathrm{m}}}{\sigma_{\mathrm{m}}^{*2}}, \tag{E.6}$$

$$\frac{\partial^2 g}{\partial \sigma_{\mathrm{eq}}^2} = \frac{2}{\sigma_{\mathrm{eq}}^{*2}}, \tag{E.7}$$

$$\frac{\partial^2 g}{\partial \sigma_{\mathrm{m}}^2} = \frac{2}{\sigma_{\mathrm{m}}^{*2}}, \tag{E.8}$$

$$\frac{\partial^2 g}{\partial \sigma_{\mathrm{eq}} \partial \sigma_{\mathrm{m}}} = \frac{\partial^2 g}{\partial \sigma_{\mathrm{m}} \partial \sigma_{\mathrm{eq}}} = 0, \tag{E.9}$$

$$\frac{\partial^2 g}{\partial \sigma_{\mathrm{eq}} \partial f} = \frac{4\tilde{D}q_4\sigma_{\mathrm{eq}}}{\left(1 - \tilde{D}fq_4\right)^3 \sigma_{\mathrm{f}}^2}, \tag{E.10}$$

$$\frac{\partial^2 g}{\partial \sigma_{\mathrm{eq}} \partial \varepsilon_{\mathrm{eq}}^{\mathrm{pl}}} = \frac{\partial g}{\partial \sigma_{\mathrm{eq}}} \frac{\partial g}{\partial \sigma_{\mathrm{f}}} \sigma_{\mathrm{f}}' = -\frac{4\sigma_{\mathrm{eq}}}{\left(1 - \tilde{D}fq_4\right)^2 \sigma_{\mathrm{f}}^3} \sigma_{\mathrm{f}}', \tag{E.11}$$

$$\frac{\partial^2 g}{\partial \sigma_{\mathrm{m}} \partial f} = \frac{4\sigma_{\mathrm{m}}}{fq_4^2\sigma_{\mathrm{f}}^2 \ln\left(\frac{1}{\tilde{D}fq_4}\right)^3}, \tag{E.12}$$

$$\frac{\partial^2 g}{\partial \sigma_{\mathrm{m}} \partial \varepsilon_{\mathrm{eq}}^{\mathrm{pl}}} = \frac{\partial g}{\partial \sigma_{\mathrm{m}}} \frac{\partial g}{\partial \sigma_{\mathrm{f}}} \sigma_{\mathrm{f}}' = -\frac{4\sigma_{\mathrm{m}}}{q_4^2\sigma_{\mathrm{f}}^3 \ln\left(\frac{1}{\tilde{D}fq_4}\right)^2} \sigma_{\mathrm{f}}'. \tag{E.13}$$

Derivatives of the increment of the void volume fraction, $\Delta f = \Delta H_1$, and of the equivalent plastic strain, $\Delta \varepsilon_{\mathrm{eq}}^{\mathrm{pl}} = \Delta H_2$, can be given as

$$\frac{\partial \Delta f}{\partial \Delta \varepsilon_{\mathrm{p}}} = B(1 - f), \tag{E.14}$$

$$\frac{\partial \Delta f}{\partial \Delta \varepsilon_{\mathrm{q}}} = \frac{\partial \Delta f}{\partial \sigma_{\mathrm{m}}} = \frac{\partial \Delta f}{\partial \sigma_{\mathrm{eq}}} = \frac{\partial \Delta f}{\partial \varepsilon_{\mathrm{eq}}^{\mathrm{pl}}} = 0, \tag{E.15}$$

$$\frac{\partial \Delta f}{\partial f} = -B\Delta \varepsilon_{\mathrm{p}}, \tag{E.16}$$

$$\frac{\partial \Delta \varepsilon_{\mathrm{eq}}^{\mathrm{pl}}}{\partial \Delta \varepsilon_{\mathrm{p}}} = \frac{\partial \Delta \varepsilon_{\mathrm{eq}}^{\mathrm{pl}}}{\partial \sigma_{\mathrm{m}}} = \frac{\partial \Delta \varepsilon_{\mathrm{eq}}^{\mathrm{pl}}}{\partial \sigma_{\mathrm{eq}}} = \frac{\partial \Delta \varepsilon_{\mathrm{eq}}^{\mathrm{pl}}}{\partial f} = \frac{\partial \Delta \varepsilon_{\mathrm{eq}}^{\mathrm{pl}}}{\partial \varepsilon_{\mathrm{eq}}^{\mathrm{pl}}} = 0, \tag{E.17}$$

$$\frac{\partial \Delta \varepsilon_{\mathrm{eq}}^{\mathrm{pl}}}{\partial \Delta \varepsilon_{\mathrm{q}}} = 1. \tag{E.18}$$

Bibliography

[1] *Prospekt zu MICROCLEAN, pulvermetallurgisch hergestellte Hochleistungsstähle*, Böhler Edelstahl GmbH & Co KG, Kapfenberg, Austria, September 2001.

[2] R. Pandorf, *Beitrag zur FE-Simulation des Kriechens partikelverstärkter Metallmatrix-Verbundwerkstoffe*, Ph.D. thesis, Ruhr-Universität Bochum, Germany, 2000.

[3] T. Mura (editor), *Micromechanics of Defects in Solids*, Kluwer Academic Publishers, Dordrecht, The Netherlands, 1987.

[4] S. Torquato (editor), *Random Heterogeneous Materials*, Springer–Verlag, New York, 2002.

[5] H.J. Böhm (editor), *Mechanics of Microstructured Materials*, Springer–Verlag, Vienna, Austria, 2004.

[6] *ABAQUS/Standard V.6.2.*, Hibbitt, Karlsson and Sorensen, Inc., Pawtucket, RI, 2001.

[7] A. Needleman, A Continuum Model for Void Nucleation by Inclusion Debonding, *J. Appl. Mech.*, 54, 525–531, 1987.

[8] A. Needleman, An Analysis of Decohesion Along an Imperfect Interface, *Int. J. Fract.*, 42, 21–40, 1990.

[9] I. Scheider, Kohäsivzonenmodell für die Modellierung von Rißfortschritt in Bauteilen mit elastisch-plastischem Materialverhalten, Teil 1: Grundlagen und Implementierung, Technical Report 19, GKSS Forschungszentrum, Geesthacht, Germany, 2000.

[10] M. Elices, G.V. Guinea, J. Gómez and J. Planas, The Cohesive Zone Model: Advantages, Limitations and Challenges, *Engng. Fract. Mech.*, 69, 137–163, 2002.

[11] I. Scheider and W. Brocks, Simulation of Cup-cone Fracture Using the Cohesive Model, *Engng. Fract. Mech.*, 70, 1943–1961, 2003.

[12] G.I. Barenblatt, The Mathematical Theory of Equilibrium Cracks in Brittle Fracture, in *Advances in Applied Mechanics 7*, pp. 55–129, New York, 1962, Academic Press.

[13] T. Siegmund and W. Brocks, Prediction of the Work of Separation and Implications to Modeling, *Int. J. Fract.*, 34, 97–116, 1999.

[14] T. Siegmund and A. Needleman, A Numerical Study of Dynamic Crack Growth in Elastic-viscoplastic Solids, *Int. J. Sol. Struct.*, 34, 769–787, 1997.

[15] C.R. Chen, I. Scheider, T. Siegmund, A. Tatschl, O. Kolednik and F.D. Fischer, Fracture Initiation and Crack Growth — Cohesive Zone Modeling and Stereoscopic Measurements, in *Proceedings of the ICF10*, edited by K. Ravi-Chandar et al., pp. 1–6, ICF 100409PR, 2001.

[16] M.A. Finot, Y.L. Shen, A. Needleman and S. Suresh, Micromechanical Modeling of Reinforcement Fracture in Particle-Reinforced Metal-Matrix Composites, *Metall. Trans.*, 25A, 2403–2420, 1994.

[17] V. Tvergaard, Model Studies of Fibre Breakage and Debonding in a Metal Reinforced by Short Fibres, *J. Mech. Phys. Solids*, 41, 1309–1326, 1993.

[18] P.O. Bouchard, F. Bay and Y. Chastel, Numerical Modelling of Crack Propagation: Automatic Remeshing and Comparison of Different Criteria, *Comput. Methods Appl. Mech. Eng.*, 192, 3887–3908, 2003.

[19] F. Armero and K. Garikipati, An Analysis of Strong Discontinuities in Multiplicative Finite Strain Plasticity and their Relation with the Numerical Simulation of Strain Localization in Solids, *Int. J. Sol. Struct.*, 33, 2863–2885, 1996.

[20] E.N. Dvorkin, A.M. Cuitiño and G. Gioia, Finite Elements with Displacement Embedded Localization Lines Insensitive to Mesh Size and Distortions, *Int. J. Num. Meth. Eng.*, 30, 541–564, 1990.

[21] T. Belytschko, N. Moës, S. Usui and C. Parimi, Arbitrary Discontinuities in Finite Elements, *Int. J. Num. Meth. Eng.*, 50, 993–1013, 2001.

[22] G.N. Wells and L.J. Sluys, Discontinuous Analysis of Softening Solids Under Impact Loading, *Int. J. Numer. Anal. Meth. Geomech.*, 25, 691–709, 2001.

[23] J. Dolbow, N. Moës and T. Belytschko, An Extended Finite Element Method for Modeling Crack Growth with Frictional Contact, *Comput. Methods Appl. Mech. Eng.*, 190, 6825–6846, 2001.

[24] M. Jirásek and T. Zimmermann, Embedded Crack Model: II. Combination with Smeared Cracks, *Int. J. Num. Meth. Eng.*, 50, 1291–1305, 2001.

[25] G.N. Wells and L.J. Sluys, A New Method for Modelling Cohesive Cracks Using Finite Elements, *Int. J. Num. Meth. Eng.*, 50, 2667–2682, 2001.

[26] J. Wulf, S. Schmauder and H. Fischmeister, Simulation of Experimental Force–Displacement Curves by a Finite-Element Elimination Technique, *Comp. Mat. Sci.*, 3, 300–306, 1994.

[27] M.G. Cockroft and D.J. Latham, Ductility and the Workability of Metals, *J. Inst. Met.*, 96, 33–39, 1968.

[28] F.A. McClintock, A Criterion for Ductile Fracture by the Growth of Holes, *J. Appl. Mech.*, 35, 363–371, 1968.

[29] M. Ayada, T. Higashino and K. Mori, Central Bursting in Extrusion of Inhomogeneous Materials, in *Advanced Technology of Plasticity*, edited by K. Lange, pp. 553–558, Berlin, 1987, Springer–Verlag.

[30] M. Oyane, Criteria of Ductile Fracture Strain, *Bulletin of JSME*, 15, 1507–1513, 1972.

[31] P. Brozzo, B. DeLuca and R. Rendina, A New Method for the Prediction of the Formability Limits of Metal Sheets, in *Proc. 7th Biennial Conf. Int. Deep Drawing Research Group*, edited by Chr. Veerman, Amsterdam, The Netherlands, 1972.

[32] S.R. Gunawardena, S. Jansson and F.A. Leckie, Transverse Ductility of Metal Matrix Composites, in *Failure Mechanisms in High Temperature Composite Materials*, edited by K. Haritos, G. Newaz and S. Mall, pp. 23–30, New York, NY, 1991, ASME.

[33] J.R. Rice and D.M. Tracey, On the Ductile Enlargement of Voids in Triaxial Stress Fields, *J. Mech. Phys. Solids*, 17, 201–217, 1969.

[34] J.W. Hancock and A.C. Mackenzie, On the Mechanisms of Ductile Failure in High-Strength Steels Subjected to Multi-Axial Stress-States, *J. Mech. Phys. Solids*, 24, 147–169, 1976.

[35] F.D. Fischer, O. Kolednik, G.X. Shan and F.G. Rammerstorfer, A Note on Calibration of Ductile Failure Damage Indicators, *Int. J. Fract.*, 73, 345–357, 1995.

[36] G. Bernauer and W. Brocks, Micromechanical Modelling of Ductile Damage and Tearing — Results of an European Numerical Round Robin, Technical Report 15, GKSS Forschungszentrum, Geesthacht, Germany, 2000.

[37] A.L. Gurson, Continuum Theory of Ductile Rupture by Void Nucleation and Growth: Part I — Yield Criteria and Flow Rules for Porous Ductile Media, *J. Engng. Mater. Technol.*, 99, 2–15, 1977.

[38] V. Tvergaard, Influence of Voids on Shear Band Instabilities under Plane Strain Conditions, *Int. J. Fract.*, 17, 389–407, 1981.

[39] V. Tvergaard and A. Needleman, Nonlocal Effects in Ductile Fracture by Cavitation Between Larger Voids, in *Computational Plasticity: Fundamentals and Applications*, edited by D.R.J. Owen, E. Oñate and E. Hinton, pp. 963–973, Swansea, UK, 1995, Pineridge Press.

[40] M. Gologanu, J.B. Leblond, G. Perrin and J. Devaux, Recent Extensions of Gurson's Model for Porous Ductile Materials, in *Continuum Micromechanics*, edited by P. Suquet, pp. 61–130, Vienna, Austria, 1997, Springer–Verlag.

[41] T. Pardoen and J.W Hutchinson, An Extended Model for Void Growth and Coalescence, *J. Mech. Phys. Solids*, 48, 2467–2512, 2000.

[42] G. Rousselier, Ductile Fracture Models and their Potential in Local Approach of Fracture, *Nucl. Engng. Design*, 105, 97–111, 1987.

[43] G. Rousselier, The Rousselier Model for Porous Metal Plasticity and Ductile Fracture, in *Handbook of Materials Behavior Models*, edited by J. Lemaître, pp. 436–445, San Diego, CA, 2001, Academic Press.

[44] J. Lemaître (editor), *A Course on Damage Mechanics*, Springer–Verlag, Berlin, 1996.

[45] J. Lemaître, How to Use Damage Mechanics, *Nucl. Engng. Design*, 80, 233–245, 1983.

[46] J.C. Zarco-Gonzalez, N.A. Fellows and J.F. Durodola, A Step-size Independent Method for Finite Element Modeling of Damage in Composites, *Comp. Sci. and Tech.*, 64, 1679–1689, 2004.

[47] H. Baaser and D. Gross, On the Limitations of CDM Approaches to Ductile Fracture Problems, in *Proceedings of the Fifth World Congress on Computational Mechanics*, edited by H.A. Mang, F.G. Rammerstorfer and J. Eberhardsteiner, paper #81462, Vienna, Austria, 2002, Vienna University of Technology.

[48] R. de Borst and E. van der Giessen (editors), *Material Instabilities in Solids*, Wiley, Chichester, 1998.

[49] C. Bellègo, J.F. Dube, G. Pijaudier-Cabot and B. Gèrard, Calibration of Nonlocal Damage Model from Size Effect Tests, *Eur. J. Mech. A/Solids*, 22, 33–46, 2003.

[50] V. Tvergaard and A. Needleman, Nonlocal Effects on Localization in a Void-sheet, *Int. J. Sol. Struct.*, 34, 2221–2238, 1997.

[51] V. Tvergaard and J.W. Hutchinson, Two Mechanisms of Ductile Fracture: Void by Void Growth versus Multiple Void Interaction, *Int. J. Sol. Struct.*, 39, 3581–3597, 2002.

[52] L. Ferrara and M. di Prisco, A Non-local Approach with Evolutionary Internal Length for the Analysis of Mode I Fracture Processes in Concrete, in *Proc. of the 15th ASCE Engineering Mechanics Conference*, New York, 2002, Columbia University.

[53] G. Pijaudier-Cabot, K. Haidar and J. Dubè, Non-local Damage Model with Evolving Internal Length, *Int. J. Numer. Anal. Meth. Geomech.*, 28, 633–652, 2004.

[54] G. Pijaudier-Cabot and Z.P. Bažant, Nonlocal Damage Theory, *J. Engng. Mech.*, 113, 1512–1533, 1987.

[55] Z.P. Bažant, Why Continuum Damage is Nonlocal: Micromechanics Arguments, *J. Eng. Mech. ASCE*, 117, 1070–1087, 1991.

[56] J.B. Leblond, G. Perrin and J. Devaux, Bifurcation Effects in Ductile Metals with Nonlocal Damage, *J. Appl. Mech.*, 61, 236–242, 1994.

[57] Z.P. Bažant and G. Pijaudier-Cabot, Nonlocal Continuum Damage, Localisation, Instability and Convergence, *J. Appl. Mech.*, 55, 287–293, 1988.

[58] V. Tvergaard and A. Needleman, Effects of Nonlocal Damage in Porous Plastic Solids, *Int. J. Sol. Struct.*, 32, 1063–1077, 1995.

[59] J. Chambert, N. Pernin, V. Lemiale and P. Picart, Micromechanical Nonlocal Damage Modeling, in *Computational Fluid and Solid Mechanics 2003*, edited by K.J. Bathe, pp. 172–175, Amsterdam, The Netherlands, 2003, Elsevier.

[60] H. Baaser and V. Tvergaard, A New Algorithmic Approach Treating Nonlocal Effects at Finite Rate Independent Deformation Using the Rousselier Damage Model, *Comput. Methods Appl. Mech. Eng.*, 192, 107–124, 2003.

[61] J. Jackiewicz and M. Kuna, Non-local Regularization for FE Simulation of Damage in Ductile Materials, *Comp. Mat. Sci.*, 28, 684–695, 2003.

[62] C. Comi and U. Perego, Criteria for Mesh Refinement in Nonlocal Damage Finite Element Analyses, *Eur. J. Mech. A/Solids*, 23, 615–632, 2004.

[63] A. Rodrìguez-Ferran, I. Morata and A. Huerta, Efficient and Reliable Nonlocal Damage Models, *Comput. Methods Appl. Mech. Eng.*, 193, 3431–3455, 2004.

[64] Z.P. Bažant, T. Belytschko and T.P. Chang, Continuum Theory for Strain-softening, *J. Engng. Mech.*, 110, 1666–1692, 1984.

[65] R.H.J Peerlings, R. de Borst, W.A.M Brekelmans and J.H.P de Vree, Gradient-enhanced Damage for Quasi-brittle Materials, *Int. J. Num. Meth. Eng.*, 39, 3391–3403, 1996.

[66] *Mathematica 5*, Wolfram Research, Inc., Champaign IL, 2003.

[67] R. de Borst and H.B. Mühlhaus, Gradient-dependent Plasticity: Formulation and Algorithmic Aspects, *Int. J. Num. Meth. Eng.*, 35, 521–539, 1992.

[68] E. Kuhl and E. Ramm, Simulation of Strain Localization with Gradient Enhanced Damage Models, *Comp. Mat. Sci.*, 16, 176–185, 1999.

[69] R.H.J. Peerlings, M.G.D. Geers, R. de Borst and W.A.M Brekelmans, A Critical Comparison of Nonlocal and Gradient-enhanced Softening Continua, *Int. J. Sol. Struct.*, 38, 7723–7746, 2001.

[70] D. Addessi, S. Marfia and E. Sacco, A Plastic Nonlocal Damage Model, *Comput. Methods Appl. Mech. Eng.*, 191, 1291–1310, 2001.

[71] R.A.B. Engelen, M.G.D. Geers and R.H.J. Peerlings, On Non-Local Damage Coupled to a J_2-Plasticity Framework, in *Proceedings of the Fifth World Congress on Computational Mechanics (WCCM V)*, edited by H.A. Mang, F.G. Rammerstorfer and J. Eberhardsteiner, paper # 80578, Vienna, Austria, 2002, Vienna University of Technology.

[72] H. Yuan and J. Chen, Comparison of Computational Predictions of Material Failure Using Nonlocal Damage Models, *Int. J. Sol. Struct.*, 41, 1021–1037, 2004.

[73] G.Z. Voyiadjis and R.J. Dorgan, Briding of Length Scales through Gradient Theory, *Comput. Methods Appl. Mech. Eng.*, 193, 1671–1692, 2004.

[74] F. Reusch, B. Svendsen and D. Klingbeil, Local and Non-local Gurson-based Ductile Damage and Failure Modelling at Large Deformation, *Eur. J. Mech. A/Solids*, 22, 779–792, 2003.

[75] R. de Borst, Some Recent Developments in Computational Modelling of Concrete Fracture, *Int. J. Fract.*, 86, 5–36, 1997.

[76] R.H.J. Peerlings, R. de Borst, W.A.M Brekelmans and M.G.D. Geers, Localisation Issues in Local and Nonlocal Continuum Approaches to Fracture, *Eur. J. Mech. A/Solids*, 21, 175–189, 2001.

[77] Z.P. Bažant and M. Jirásek, Nonlocal Integral Formulations of Plasticity and Damage: Survey of Progress, *J. Engng. Mech.*, pp. 1119–1149, 2002.

[78] M. Jirásek and S. Rolshoven, Comparison of Integral-type Nonlocal Plasticity Models for Strain-softening Materials, *Int. J. Engng. Sci.*, 41, 1553–1602, 2003.

[79] A. Needleman, Material Rate-dependence and Mesh-sensitivity in Localization Problems, *Comput. Methods Appl. Mech. Eng.*, 67, 69–85, 1988.

[80] O. Harireche and B. Loret, 3-D Dynamic Strain-localization: Shear-band Pattern Transition in Solids, *Eur. J. Mech. A/Solids*, 11, 733–752, 1992.

[81] B. Loret, J.H. Prevost and A. Deb, Finite Element Simulation of Dynamic Strain-localization: a Multi-scale Problem, *Comput. Methods Appl. Mech. Eng.*, 120, 315–338, 1995.

[82] G. Duvaut and J.L. Lions (editors), *Inequalities in Mechanics and Physics*, Springer-Verlag, Berlin, 1976.

[83] L.J. Sluys and W.M. Wang, Macroscopic Modelling of Stationary and Propagative Instabilities, in *Material Instabilities in Solids*, edited by R. de Borst and E. van der Giessen, pp. 489–505, Chichester, 1998, Wiley.

[84] W.M. Wang and L.J. Sluys, Formulation of an Implicit Algorithm for Finite Deformation Viscoplasticity, *Int. J. Sol. Struct.*, 37, 7329–7348, 2000.

[85] E. Cosserat and F. Cosserat (editors), *Théorie des corps déformables*, A. Hermann et fils., Paris, France, 1909.

[86] R. de Borst, Simulation of Strain Localization: A Reappraisal of Cosserat Continuum, *Eng. Comp.*, 8, 317–332, 1991.

[87] M. Alsaleh, *Numerical Modeling of Strain Localization in Granular Materials Using Cosserat Theory Enhanced with Microfabric Properties*, Ph.D. thesis, Louisiana State University, Baton Rouge, LA, USA, 2004.

[88] P. Grammenoudis, *Mikropolare Plastizität*, Ph.D. thesis, Technische Universität Darmstadt, Germany, 2003.

[89] F. Reusch, D. Klingbeil and S. Schmauder, Simulation duktilen Rißfortschritts in einem Al/SiC-Verbundwerkstoff mit dem Materialmodell von Gurson, in *Proceedings of the Micro Mat '95*, edited by T. Winkler B. Michel, pp. 641–646, Berlin, 1996, Deutscher Verband für Materialforschung und -prüfung.

[90] R. Hambli, Comparison between Lemaître and Gurson Damage Models in Crack Growth Simulation During Blanking Process, *Int. J. Mech. Sci.*, 43, 2769–2790, 2000.

[91] A. Imad, On the Ductile Fracture Based on the Continuum Damage in Steel Case, *Méc. Ind.*, 3, 45–50, 2001.

[92] P. Nègre, D. Steglich, W. Brocks and M. Kocak, Numerical Simulation of Crack Extension in Aluminium Welds, *Comp. Mat. Sci.*, 28, 723–731, 2003.

[93] N. Aravas, On the Numerical Integration of a Class of Pressure-Dependent Plasticity Models, *Int. J. Num. Meth. Eng.*, 24, 1395–1416, 1987.

[94] Z.L. Zhang, On the Accuracies of Numerical Integration Algorithms for Gurson-based Pressure-dependent Elastoplastic Constitutive Models, *Comput. Methods Appl. Mech. Eng.*, 121, 15–28, 1995.

[95] U. Mühlich and W. Brocks, On the Numerical Integration of a Class of Pressure-dependent Plasticity Models Including Kinematic Hardening, *Computational Mechanics*, 31, 479–488, 2003.

[96] M. Ortiz and E.P. Popov, Accuracy and Stability of Integration Algorithms for Elastoplastic Constitutive Relations, *Int. J. Num. Meth. Eng.*, 21, 1561–1576, 1985.

[97] Z.L. Zhang, Explicit Consistent Tangent Moduli With a Return Mapping Algorithm for Pressure-Dependent Elastoplasticity Models, *Comput. Methods Appl. Mech. Eng.*, 121, 29–44, 1995.

[98] S.M. Aboutayeb, *Comportement à l'endommagement des matériaux métalliques hétérogènes: Simulation et expérience*, Ph.D. thesis, Université des Sciences et Technologies de Lille, Lille, France, 2000.

[99] U. Prahl, S. Bourgeois, T. Pandorf, M. Aboutayeb, O. Debordes and D. Weichert, Damage Parameter Identification by a Periodic Homogenization Approach, *Comp. Mat. Sci.*, 25, 159–165, 2002.

[100] M. Springmann and M. Kuna, Identification of Material Parameters of the Rousselier Model by Non-Linear Optimization, *Comp. Mat. Sci.*, 26, 202–209, 2003.

[101] M. Springmann and M. Kuna, Identifikation schädigungsmechanischer Materialparameter mit Hilfe nichtlinearer Optimierungsverfahren am Beispiel des Rousselier Modells, in *Sonderforschungsbereich 393, Numerische Simulation auf massiv parallelen Rechnern*. Techn. Universität Chemnitz, 2002.

[102] T. Nakamura and S. Suresh, Effects of Thermal Residual Stresses and Fiber Packing on Deformation of Metal-Matrix-Composites, *Acta Metall.*, 41(6), 1665–1681, 1993.

[103] J. LLorca, A. Needleman and S. Suresh, An Analysis of the Effects of Matrix Void Growth on Deformation and Ductility in Metal–Ceramic Composites, *Acta Metall.*, 39, 2317–2335, 1991.

[104] M. Geni and M. Kikuchi, Damage Analysis of Aluminum Matrix Composite Considering Non-Uniform Distribution of SiC Particles, *Acta Mater.*, 46, 3125–3133, 1998.

[105] L.L. Mishnaevsky, M. Dong, S. Hönle and S. Schmauder, Computational Mesomechanics of Particle-reinforced Composites, *Comp. Mat. Sci.*, 16, 133–143, 1999.

[106] J. Segurado, *Micromecánica computacional de materiales compuestos reforzados con partículas*, Ph.D. thesis, Universidad Politécnica de Madrid, Madrid, Spain, 2004.

[107] H.J. Böhm and T. Drabek, Implementation of Nonlocal Damage Models in Commercial FE-Codes, paper 262, in *Computational Mechanics – Proceedings of the Sixth World Congress on Computational Mechanics*, edited by Z.H.Yao et al., Beijing, China, 2004, Tsinghua University Press and Springer–Verlag.

[108] H.J. Böhm, D. Duschlbauer, T. Drabek and C. Chimani, Finite Element Based Micromechanical Model of Ductile Intergranular Cracks in Columnar Two-Phase System, paper 258, in *Computational Mechanics – Proceedings of the Sixth World Congress on Computational Mechanics*, edited by Z.H.Yao et al., Beijing, China, 2004, Tsinghua University Press and Springer–Verlag.

[109] C. Hu, S. Moorthy and S. Ghosh, A Voronoi Cell Finite Element for Ductile Damage in MMCs, in *Proceedings of NUMIFORM 2004*, edited by S. Ghosh et al., pp. 1893–1898, Melville, NY, 2004, American Institute of Physics.

[110] T. Drabek and H.J. Böhm, Damage Models for Studying Ductile Matrix Failure in Composites, *Comp. Mat. Sci.*, 32, 329–336, 2005.

[111] E. Weissenbek, H.E. Pettermann and S. Suresh, Elasto-plastic Deformation of Compositionally Graded Metal-Ceramic Composites, *Acta Mater.*, 45, 3401–3417, 1997.

[112] H.J. Böhm and W. Han, Comparisons between Three-Dimensional and Two-Dimensional Multi-Particle Unit Cell Models for Particle Reinforced Metal Matrix Composites, *Modell. Simul. Mater. Sci. Eng.*, 9, 47–65, 2001.

[113] A.A. Gusev, Representative Volume Element Size for Elastic Composites: A Numerical Study, *J. Mech. Phys. Solids*, 45, 1449–1459, 1997.

[114] J. LLorca and C. González, Microstructural Factors Controlling the Strength and Ductility of Particle Reinforced Metal-matrix Composites, *J. Mech. Phys. Solids*, 46, 1–28, 1998.

Curriculum Vitae

Personal Data

Name	:	Dipl.-Ing. Thomas Drabek
Date of birth	:	December 30, 1974
Place of birth	:	Vienna, Austria
Citizenship	:	Austrian

Education

09/01 – 01/05	Doctoral Student at the Christian Doppler Laboratory for Functionally Oriented Materials Design at the Institute of Light Weight Design and Structural Biomechanics, Vienna University of Technology, Austria
04/95 – 06/01	Studies of "Industrial Engineering" at the Vienna University of Technology, Austria, leading to the degree of Diplom-Ingenieur
09/89 – 06/94	Technical High School (HTL) in "Industrial Engineering", Technologisches Gewerbemuseum (TGM), Vienna, Austria
09/85 – 06/89	4 years Secondary School in Vienna, Austria
09/81 – 06/85	4 years Primary School in Vienna, Austria

Employment

09/01 – 01/05	Research assistant at the Christian Doppler Laboratory for Functionally Oriented Materials Design at the Institute of Light Weight Design and Structural Biomechanics, Vienna University of Technology, Austria